UNIVERSITY OF CALIFORNIA
RIVERSIDE

Modifying Environmental Chambers for Varying Applications: From Evaluating Secondary Organic Aerosol Formation to Health Effects Investigation with Animal Exposure

A Dissertation submitted in partial satisfaction
of the requirements for the degree of

Doctor of Philosophy

in

Chemical and Environmental Engineering

by

Qi Li

March 2022

Dissertation Committee:
Dr. David R. Cocker III, Chairperson
Dr. Don Collins
Dr. David D. Lo

The Dissertation of Qi Li is approved:

_____

_____

_____

Committee Chairperson

University of California, Riverside

Acknowledgments

Chapter 2 and Chapter 4 of this thesis, are reprints of the materials as they appear in

- Li, Q., Jiang, J., Afreh, I. K., Barsanti, K. C., and Cocker III, D. R.: Secondary organic aerosol formation from camphene oxidation: measurements and modeling, 22, 3131–3147, https://doi.org/10.5194/ACP-22-3131-2022, 2022.
- Biddle, T. A., Li, Q., Maltz, M. R., Tandel, P. N., Chakraborty, R., Yisrael, K., Drover, R., Cocker, D. R., and Lo, D. D.: Salton Sea aerosol exposure in mice induces a pulmonary response distinct from allergic inflammation, Sci. Total Environ., 792, 148450, https://doi.org/10.1016/J.SCITOTENV.2021.148450, 2021.

The co- authors Dr. David Cocker, Dr. Kelley Barsanti and Dr. David Lo listed in these publications directed and supervised the research which form the basis for this dissertation.

ABSTRACT OF THE DISSERTATION

Modifying Environmental Chambers for Varying Applications: from Evaluating Secondary Organic Aerosol Formation to Health Effects Investigation with Animal Exposure

by

Qi Li

Doctor of Philosophy, Graduate Program in Chemical and Environmental Engineering
University of California, Riverside, March 2022
Dr. David R. Cocker III, Chairperson

Camphene is a significant monoterpene measured in both biogenic and biomass burning emission but is not well-studied in environmental chambers. This thesis includes a series of experiments conducted in the UCR environmental chamber to explore the SOA formation from OH-initiated oxidation of camphene. Experimental observations were compared to simulations from two detailed chemical box models. Experiments performed with added nitrogen oxides resulted in higher SOA yields (up to 64 %) than ones without added NOx (up to 28 %). Modeling results suggest a possible undervaluation of RO_2 chemistry in previous SOA studies. The higher SOA yields observed at higher initial NO_x levels were attributed to the higher production of peroxy radicals (RO_2) and the generation of highly oxygenated organic molecules (HOMs) formed through unimolecular RO_2 reactions. An additional experimental study on Volatile Consumer Products (VCPs) is included herein. VCPs are major contributors to the total volatile organic compounds (VOCs) emissions. Some low vapor pressure VOCs (LVP-VOCs) have shown high potentials of SOA formation. The low vapor pressure of the LVP-VOCs makes SOA

studies challenging using traditional environmental chambers. This thesis compares two widely known environmental chamber systems- UCR chamber and Caltech chamber to identify best practices for the study of SOA formation. A series of experiments benzyl alcohol oxidation studies were conducted in both chambers as a case study to identify best practices for chamber studies and development of a consistent experimental protocol and an improved UCR chamber system. Upgrades were performed on the UCR chamber facility leading to a new fixed-volume chamber with orders of magnitude lower backgrounds and >70% decrease in total particle number decay rates. Additionally, a separate environmental chamber system at the UCR school of medicine was modified to improve animal exposure studies. To meet the requirement of varying research objectives, animal whole-body exposure chamber systems were upgraded for different types of particulate matter and experimental conditions. A series of PM exposure experiments were conducted to investigate the health effects of Salton Sea Spray on mice, in which the gene expression analysis data suggested PMs from different sources may have a possible synergistic effect on mice lungs.

Contents

List of Figures

List of Tables

Chapter 1 : Introduction

Air pollution has been the fifth ranking human health risk factor globally, following child and maternal malnutrition, dietary risks, high systolic blood pressure, tobacco (GBD, 2018). According to World Health Organization, about 4.2 million deaths every year come out as a result of exposure to ambient air pollution, while about 3.8 million deaths every year are due to household exposure to smoke from dirty cookstoves and fuels (WHO, 2019). PM, one of the 6 criteria air pollutants defined by EPA, significantly impacts human health and environments including climate change and visibility impairment. In 2017, 5.25% of all deaths in were attributable to ambient particulate matter pollution, making it the eighth leading risk for deaths, with a total of 2.94 million (2.50–3.36) deaths globally (GBD, 2018). Secondary organic aerosol, formed through oxidation of volatile organic compound (VOC), is estimated to account for a dominant fraction of the fine particle mass in the troposphere (Hallquist et al., 2009; Cappa et al., 2016; Jathar et al., 2017; Ma et al., 2017).

For decades, environmental chambers, also known as smog chambers, have been applied in a variety of research fields including study on atmospheric reaction, secondary organic aerosol formation, combustion engine emission evaluation, health effects investigation of pollutants (Nakao et al., 2011; Jahn et al., 2021; Carter et al., 1995; Cocker et al., 2001; Peng et al., 2018), etc. Environmental chambers have been heavily relied for developing and evaluating chemical mechanisms for secondary pollutants formation. For example, models for ozone formation prediction has been developed based on data from

environmental chamber (Dodge, 2000). Environmental chambers were modified and upgraded to meet the requirements of different research objectives. In this thesis, the modification, application and standardization of environmental chambers are presented with studies on SOA formation characterization from oxidation of camphene, chamber system comparison between the UCR chambers (old collapsible chamber and new fixed-volume chamber) and Caltech chamber, and whole-body animal exposure study.

Many studies have reported camphene as a top contributor by mass in measured biogenic and pyrogenic monoterpene emissions (Benelli et al., 2018; Hatch et al., 2019; Komenda, 2002; Mazza & Cottrell, 1999; Moukhtar et al., 2006). However, the SOA formation potential of camphene was under-studied. The old UCR collapsible chamber was used to carry out a series of ·OH initiated oxidation experiments of camphene under varying NO_x levels to evaluate the chemistry role in determining SOA formation to close the gap. Chapter 2 is a reprint of the published work (Li et al., 2022). A comprehensive synthesis study of combining chamber observation and box modeling Statewide Air Pollution Research Center (SAPRC) simulations is presented with high consistency between chamber observations and simulated RO_2 chemistry. Unexpected higher SOA mass yields were measured with added NO_x (0.33–0.64) than without added NO_x (0.08–0.26) at atmospherically relevant ·OH concentrations, different from other monoterpenes (e.g., α-pinene, d-limonene) and n-alkanes (carbon≤ 10) (Nøjgaard et al., 2006; Ng et al., 2007b). Based on SAPRC simulation results, the RO_2 + NO pathway favored in experiments with added NO_x formed HOMs with much lower volatilities than products formed in other pathways, which explains the higher SOA yield in experiments with added NO_x. The study

emphasizes the importance of RO_2 chemistry in driving the reaction rates and SOA formation.

In addition to BVOCs, volatile consumer products related VOCs is another important SOA precursor source but under studied. Chen and Luo estimated that, in 2012, the third ranking anthropogenic VOC emission source in California's South Coast Air Basin is consumer products, following light -duty passenger cars and off-road equipment. With strict emission regulations and technology development of tailpipe emission control, automotive emissions of VOCs have decreased obviously in California. As a result, consumer products, including pesticides, coatings, printing inks, adhesives, cleaning agents, and personal care products, are believed to contribute an even larger fraction of the total VOC emission. Recent study predicted that the use of volatile chemical products constitutes half of fossil fuel VOC emissions in industrialized cities (7.6Tg/16.0Tg= 47.5%) (McDonald, et al. 2018). In the LA basin especially, volatile consumer products (VCPs) have become the biggest source for VOC emission and SOA potential (McDonald, et al. 2018). Low vapor pressure-volatile organic compounds (LVP-VOC), being one of the major component in the VCP category, is defined by California Air Resources Board (CARB) as a chemical "compound" or "mixture" that contains at least one carbon atom, having a vapor pressure less than 0.1 mm Hg at 20°C, or having more than 12 carbon atoms, or having a boiling point greater than 216°C (CARB, 2015). LVP-VOCs are widely found in industry solvent, coatings, cosmetic, perfume, and pharmaceutical products (Bernard et al., 2013; Vo and Morris, 2014) but can own exemption from CARB's consumer products regulation (CARB, 2019) in some products due to their low vapor pressure (considered as non-volatile) (Võ

and Morris, 2014). However, recent studies show that some of the LVP-VOCs can contribute to SOA formation and O_3 concentration as much as typical traditional VOCs (Võ and Morris, 2014; Weihua and Lijie, 2018). It is therefore important to identify and classify VOCs from VCPs. Oxidation experiments are required to characterize their potential SOA formation at atmospheric related environments.

However, chamber facilities differ in various aspects (such as shape, size, materials, light intensity, etc.) including operation procedures and data processing methodology. As a result, uncertainties across different chamber systems exist and limit the consistency of conclusions and mechanisms developed from the environmental chamber data. LVP-VOCs are challenging the operation of traditional environmental chambers due to its extremely low vapor pressure and forcing the exposure of data inconsistency due to less rigorous assumptions. The conducted chamber comparison between UCR old collapsible chamber, UCR new fixed volume chamber, and Caltech chamber was initiated by a big discrenpency being observed. The photooxidation experiments conducted in Caltech chamber with benzyl alcohol showed a SOA mass yield that is higher than the one observed in the UCR chamber by almost 300%. Although the experiments were not conducted under exactly same conditions, the differences between experiments conditions are insufficient to explaining such big SOA yield difference with known mechanisms and limited characterization information of both chambers. To further explain the difference and improve representativeness of chamber data, presented in chapter 3, a detailed comparison was done in functional characteristics, experimental protocol, and data analysis. Especially, corrections of effects such as vapor wall loss and particle wall loss are discussed in this

thesis with our most up-to-date understanding. The 300% gap was closed with finding from chamber comparison. A summary table is provided with recommend modification and optimization of chamber facilities. In addition, 8 compounds that are VCPs related were performed in oxidation experiments in the new UCR fixed-volume chamber using the refined experimental protocol. SOA formation data is presented in section 3.3.3.

The chapter 4 is a reprint of a published work (Biddle et al., 2021). Chapter 4 covers the application of environmental chamber in health effects investigation of PMs. A dual chamber system was upgraded from the previous single chamber system used in study by Peng et al. (2018). PMs have been found to be related with multiple respiratory diseases for a long time. However, the mechanism of health effects of particulate matters is still unclear. Studies on mechanisms of ultrafine particle-induced health effects proposed reactive oxygen species (ROS) and oxidative stress to be reasons for PM-mediated health effects (Ayres et al., 2008; Donaldson et al., 2005; Leikauf et al., 2020). Soluble PM may release transition metals or organics, both of which can undergo cyclical chemical reactions in the lung to form free radicals and therefore increase the oxidative stress. I served as a main contributor to this study from water sampling to experimental design and conduction. For regular experiments, I was in charge of generating a stable PM suspension for mice while keeping consistent total PM mass concentration across different exposure experiments. A control chamber was built with upgrades on relative humidity control and NH_3 monitoring. I also performed a preliminary chemical composition analysis using aerosol mass spectrometer to investigate correlations between mice responses and PM composition, in which consistent results were observed between PM composition and mice

responses, indicating that organic component may contain the "active" species that could effectively induce inflammation and trigger immune responses. Further studies are required to advance our understanding of the mechanism of how PMs interact with the organism. Studies using the environmental chamber based whole-body exposure chamber is an efficient way to introduce targeted species (including microorganism and gas molecules in addition to particles) to animals in a less movement-restricted way.

In addition to the publication/work presented in the thesis, a list of other projects that I have been heavily involved is list below.

Publications presented:

- Li, Q., Jiang, J., Afreh, I. K., Barsanti, K. C., and Cocker, D. R.: Secondary Organic Aerosol Formation from Camphene Oxidation: Measurements and Modeling, Atmos. Chem. Phys. 2022 (accepted, in proofreading)
- Biddle, T. A., Li, Q., Maltz, M. R., Tandel, P. N., Chakraborty, R., Yisrael, K., Drover, R., Cocker, D. R., and Lo, D. D.: Salton Sea aerosol exposure in mice induces a pulmonary response distinct from allergic inflammation, Sci. Total Environ., 792, 148450, https://doi.org/10.1016/J.SCITOTENV.2021.148450, 2021.

Others:

The contents in Chapter 2 will be converted into two papers:

- Optimizing Environmental Chambers for characterizing Secondary Organic Aerosol formation based on a Comprehensive Chamber Comparison.
- Secondary Organic Aerosol Formation from Oxidation of Selected Compounds in Volatile Consumer Product

I participated in the SOA characterization of decamethylcyclopentasiloxane led by Caltech group:

- Charan, S. M., Huang, Y., Buenconsejo, R. S., Li, Q., Cocker, D. R., and Seinfeld, J. H.: Secondary organic aerosol formation from the oxidation of decamethylcyclopentasiloxane at atmospherically relevant OH concentrations, Atmos. Chem. Phys., 22, 917–928, https://doi.org/10.5194/ACP-22-917-2022, 2022.

I participated heavily in the particle wall loss characterization project, which is leading to a co-author paper:

- Le, C., Li, Q. and Cocker, D. R.: Characterization of Environmental Chamber Wall Loss, in preperation, expect to publish in 2022

I conducted the experiments on the SOA formation characterization of geraniol, which is a typical electric vaping related compound. This is leading to a co-author paper:

- The Implication of Vaping Emission from Geraniol on Indoor Air Quality (in preparation).

I processed and summarized the chamber experiments results for improving the air quality modeling of VCPs in cooperation with Colorado State University. This is leading to a co-author paper:

- Improving the Representation of Secondary Organic Aerosol from VCP Sources i n Air Quality Models.

I participated in the publication which reviews the ecosystem degradation, air quality and observed diseases near Salton Sea area. I provided a review on the air quality and potential PM sources in the Salton Sea area, including dry bed dust, desert dust, water spray, agricultural PM, and seasonal pollen.

- Biddle, T., Chakraborty, R., Li, Q., Maltz, M., Gerrard, J., and Lo, D. D.: The drying Salton Sea and asthma : A, Calif. Agric., 2022.

I participated heavily in the ship boiler emission task by taking charge of the sampling and corresponding analysis for aldehydes, VOCs, and PMs with HPLC, Thermal Desorption GC and scanning mobility particle sizer.

I conducted two 28-day long term mice exposure study with Alternaria PMs using the upgraded dual whole-body exposure anaimal chambers. I also bulit the sampling draft for water sample collection at the Salton Sea, dual small expsoure chambers for long term expsosure study, and the mini chamber setup for particle lung deposition study.

I won the Best Student Award in the CARTEEH conference by giving the talk: Investigating Health Effects of Various Particulate Matter on Mice by using Animal Exposure Chambers, CARTEEH, May 2021

Reference

"Air Pollution." World Health Organization, World Health Organization, 19 June 2019, www.who.int/airpollution/en/.

Ayres, J. G., Borm, P., Cassee, F. R., Castranova, V., Donaldson, K., Ghio, A., Harrison, R. M., Hider, R., Kelly, F., Kooter, I. M., Marano, F., Maynard, R. L., Mudway, I., Nel, A., Sioutas, C., Smith, S., Baeza-Squiban, A., Cho, A., Duggan, S., & Froines, J. (2008). Evaluating the toxicity of airborne particulate matter and nanoparticles by measuring oxidative stress potential - A workshop report and consensus statement. Inhalation Toxicology, 20(1), 75–99. https://doi.org/10.1080/08958370701665517

Benelli, G., Govindarajan, M., Rajeswary, M., Vaseeharan, B., Alyahya, S. A., Alharbi, N. S., Kadaikunnan, S., Khaled, J. M., and Maggi, F.: Insecticidal activity of camphene, zerumbone and α-humulene from Cheilocostus speciosus rhizome essential oil against the Old-World bollworm, Helicoverpa armigera, Ecotoxicol. Environ. Saf., 148, 781–786, https://doi.org/10.1016/j.ecoenv.2017.11.044, 2018.

Bernard, François, et al. "Atmospheric Chemistry of Benzyl Alcohol: Kinetics and Mechanism of Reaction with OH Radicals." Environmental Science & Technology, vol. 47, no. 7, 2013, pp. 3182–3189., doi:10.1021/es304600z.

Biddle, T. A., Li, Q., Maltz, M. R., Tandel, P. N., Chakraborty, R., Yisrael, K., Drover, R., Cocker, D. R., and Lo, D. D.: Salton Sea aerosol exposure in mice induces a pulmonary response distinct from allergic inflammation, Sci. Total Environ., 792, 148450, https://doi.org/10.1016/J.SCITOTENV.2021.148450, 2021.

California Air Resources Board (CARB), 2015. Regulation for Reducing Emissions from Consumer Products. Title 17, California Code of Regulations, Division 3, (Chapter1), Sub (chapter 8).5, Article 2 pp. 94507–94517. Available online at: https://www.arb.ca.gov/consprod/regs/regs.htm.

California Air Resources Board. "Current Regulations." California Air Resources Board, 2019, ww3.arb.ca.gov/consprod/regs/regs.htm.

Cappa, C. D., and Wilson, K. R. (2012): Multi-generation gas-phase oxidation, equilibrium partitioning, and the formation and evolution of secondary organic aerosol, Atmos. Chem. Phys., 12, 9505-9528, 10.5194/acp-12-9505-2012

Cappa, C. D., Jathar, S. H., Kleeman, M. J., Docherty, K. S., Jimenez, J. L., Seinfeld, J. H., and Wexler, A. S.: Simulating secondary organic aerosol in a regional air quality model using the statistical oxidation model – Part 2: Assessing the influence of vapor wall losses, Atmos. Chem. Phys., 16, 3041-3059, https://doi.org/10.5194/acp-16-3041-2016, 2016.

Carter, W. P. L., Pierce, J. A., Luo, D., and Malkina, I. L.: Environmental chamber study of maximum incremental reactivities of volatile organic compounds, Atmos. Environ., 29, 2499–2511, https://doi.org/10.1016/1352-2310(95)00149-S, 1995.

Carter, W. P. L. (2002): "Development of a Next Generation Environmental Chamber Facility for Chemical Mechanism and VOC Reactivity Research," Draft Research Plan and First Progress Report to the United States Environmental Protection Agency Cooperative Agreement CR 827331-01-0, January 3. Available at http://www.cert.ucr.edu/~carter/epacham.

Carter, W. P. L. (2004): "Evaluation of a Gas-Phase Atmospheric Reaction Mechanism for Low NOx Conditions," Final Report to California Air Resources Board Contract No. 01-305, May 5. Available at http://www.cert.ucr.edu/~carter/absts.htm#lnoxrpt.

Carter, W. P. L., D. R. Cocker III, D. R. Fitz, I. L. Malkina, K. Bumiller, C. G. Sauer, J. T. Pisano, C. Bufalino, and C. Song (2005a): "A New Environmental Chamber for Evaluation of Gas-Phase Chemical Mechanisms and Secondary Aerosol Formation", Atmos. Environ. 39 7768-7788.

Carter, W. P. L., I. L. Malkina, D. R. Cocker III, and C. Song (2005b): "Environmental Chamber Studies of VOC Species in Architectural Coatings and Mobile Source Emissions," Final Report to the South Coast Air Quality Management District Contract No. 03468, July 5. Available at http://www.cert.ucr.edu/~carter/absts.htm#scaqcham..

Chen, Jianjun, and Dongmin Luo. "Ozone Formation Potentials of Organic Compounds from Different Emission Sources in the South Coast Air Basin of California." Atmospheric Environment, vol. 55, 2012, pp. 448–455., doi:10.1016/j.atmosenv.2012.02.082.

Cocker, D. R., Flagan, R. C., and Seinfeld, J. H.: State-of-the-art chamber facility for studying atmospheric aerosol chemistry, Environ. Sci. Technol., 35, 2594–2601, https://doi.org/10.1021/es0019169, 2001.

Dodge, M. C. (2000): "Chemical Oxidant Mechanisms for Air Quality Modeling, Critical Review Paper for 1998 Ozone Assessment," Atmos. Environ, 34, 2103-2130.

Donaldson, K., Tran, L., Jimenez, L. A., Duffin, R., Newby, D. E., Mills, N., MacNee, W., & Stone, V. (2005). Combustion-derived nanoparticles: A review of their toxicology following inhalation exposure. In Particle and Fibre Toxicology (Vol. 2, Issue 1, pp. 1–14). BioMed Central. https://doi.org/10.1186/1743-8977-2-10

GBD 2017 Risk Factors Collaborators. "Global, Regional, and National Comparative Risk Assessment of 84 Behavioural, Environmental and Occupational, and Metabolic Risks or Clusters of Risks for 195 Countries and Territories, 1990–2017: a Systematic Analysis for the Global Burden of Disease Study 2017." The Lancet, vol. 392, no. 10159, 2018, pp. 1923–1994., doi:10.1016/s0140-6736(18)32225-6.

Hallquist, M., Wenger, J. C., Baltensperger, U., Rudich, Y., Simpson, D., Claeys, M., Dommen, J., Donahue, N. M., George, C., Goldstein, A. H., Hamilton, J. F., Herrmann, H., Hoffmann, T., Iinuma, Y., Jang, M., Jenkin, M. E., Jimenez, J. L., Kiendler-Scharr, A., Maenhaut, W., McFiggans, G., Mentel, Th. F., Monod, A., Prévôt, A. S. H., Seinfeld, J. H., Surratt, J. D., Szmigielski, R., and Wildt, J.: The formation, properties and impact of secondary organic aerosol: current and emerging issues, Atmos. Chem. Phys., 9, 5155-5236, https://doi.org/10.5194/acp-9-5155-2009, 2009.

Hatch, L. E., Jen, C. N., Kreisberg, N. M., Selimovic, V., Yokelson, R. J., Stamatis, C., York, R. A., Foster, D., Stephens, S. L., Goldstein, A. H., and Barsanti, K. C.: Highly Speciated Measurements of Terpenoids Emitted from Laboratory and Mixed-Conifer Forest Prescribed Fires, Environ. Sci. Technol., https://doi.org/10.1021/acs.est.9b02612, 2019.

Jahn, L. G., Wang, D. S., Dhulipala, S. V., and Ruiz, L. H.: Gas-Phase Chlorine Radical Oxidation of Alkanes: Effects of Structural Branching, NOx, and Relative Humidity Observed during Environmental Chamber Experiments, J. Phys. Chem. A, 125, 7303–7317, https://doi.org/10.1021/ACS.JPCA.1C03516/SUPPL_FILE/JP1C03516_SI_001.PDF, 2021.

Jathar, S. H., Woody, M., Pye, H. O. T., Baker, K. R., and Robinson, A. L.: Chemical transport model simulations of organic aerosol in southern California: model evaluation and gasoline and diesel source contributions, Atmos. Chem. Phys., 17, 4305-4318, https://doi.org/10.5194/acp-17-4305-2017, 2017.

Komenda, M.: Monoterpene emissions from Scots pine (Pinus sylvestris): Field studies of emission rate variabilities, J. Geophys. Res., 107, 4161, https://doi.org/10.1029/2001JD000691, 2002.

Leikauf, G. D., Kim, S. H., & Jang, A. S. (2020). Mechanisms of ultrafine particle-induced respiratory health effects. In Experimental and Molecular Medicine (Vol. 52, Issue 3, pp. 329–337). Springer Nature. https://doi.org/10.1038/s12276-020-0394-0

Li, Q., Jiang, J., Afreh, I. K., Barsanti, K. C., and Cocker, D. R.: Secondary Organic Aerosol Formation from Camphene Oxidation : Measurements and Modeling, Atmos. Chem. Phys. 2022 (accepted, in proofreading)

Ma, P. K., Zhao, Y., Robinson, A. L., Worton, D. R., Goldstein, A. H., Ortega, A. M., Jimenez, J. L., Zotter, P., Prévôt, A. S. H., Szidat, S., and Hayes, P. L.: Evaluating the impact of new observational constraints on P-S/IVOC emissions, multi-generation oxidation, and chamber wall losses on SOA modeling for Los Angeles, CA, Atmos. Chem. Phys., 17, 9237-9259, https://doi.org/10.5194/acp-17-9237-2017, 2017.

Mazza, G. and Cottrell, T.: Volatile components of roots, stems, leaves, and flowers of Echinacea species, J. Agric. Food Chem., https://doi.org/10.1021/jf981117y, 1999.

Moukhtar, S., Couret, C., Rouil, L., and Simon, V.: Biogenic Volatile Organic Compounds (BVOCs) emissions from Abies alba in a French forest, Sci. Total Environ., 354, 232–245, https://doi.org/10.1016/j.scitotenv.2005.01.044, 2006.

Mcdonald, Brian C., et al. "Volatile Chemical Products Emerging as Largest Petrochemical Source of Urban Organic Emissions." Science, vol. 359, no. 6377, 2018, pp. 760–764., doi:10.1126/science.aaq0524.

Nakao, S., Shrivastava, M., Nguyen, A., Jung, H., and Cocker, D.: Interpretation of Secondary Organic Aerosol Formation from Diesel Exhaust Photooxidation in an Environmental Chamber, 45, 964–972, https://doi.org/10.1080/02786826.2011.573510, 2011.

Ng, N. L., Chhabra, P. S., Chan, A. W. H., Surratt, J. D., Kroll, J. H., Kwan, A. J., McCabe, D. C., Wennberg, P. O., Sorooshian, A., Murphy, S. M., Dalleska, N. F., Flagan, R. C., and Seinfeld, J. H.: Effect of NOx level on secondary organic aerosol (SOA) formation from the photooxidation of terpenes, Atmos. Chem. Phys., https://doi.org/10.5194/acp-7-5159-2007, 2007.

Peng, X., Madany, A. M., Jang, J. C., Valdez, J. M., Rivas, Z., Burr, A. C., Grinberg, Y. Y., Nordgren, T. M., Nair, M. G., Cocker, D., Carson, M. J., and Lo, D. D.: Continuous Inhalation Exposure to Fungal Allergen Particulates Induces Lung Inflammation While Reducing Innate Immune Molecule Expression in the Brainstem, ASN Neuro, 10, 175909141878230, https://doi.org/10.1177/1759091418782304, 2018.

Võ, Uyên-Uyên T., and Michael P. Morris. "Nonvolatile, Semivolatile, or Volatile: Redefining Volatile for Volatile Organic Compounds." Journal of the Air & Waste Management Association, vol. 64, no. 6, 2014, pp. 661–669., doi:10.1080/10962247.2013.873746.

Weihua Li, et al. "Potential of select intermediate-volatility organic compounds and consumer products for secondary organic aerosol and ozone formation under relevant urban conditions" Atmospheric Environment, Volume 178, 2018, Pages 109-117, ISSN 1352-2310, https://doi.org/10.1016/j.atmosenv.2017.12.019.

Zhang, X., Cappa, C. D., Jathar, S. H., McVay, R. C., Ensberg, J. J., Kleeman, M. J., Seinfeld, J. H. (2014). Influence of Vapor Wall Loss in Laboratory Chambers on Yields of Secondary Organic Aerosol. P. Natl. Acad. Sci. USA. 111:5802–5807.

Zhang, X., Schwantes, R. H., McVay, R. C., Lignell, H., Coggon, M. M., Flagan, R. C., Seinfeld, J. H. (2015). Vapor Wall Deposition in Teflon Chambers. Atmos. Chem. Phys. 15:4197-4214.

Chapter 2 : SOA Formation from Oxidation of Camphene: a synthesis study with experimental measurements and modeling

2.1 Introduction

On a global scale, biogenic monoterpene emissions are estimated to contribute 14% of the total reactive volatile organic compound (VOC) flux (Tg C) (Guenther, 1995). Camphene is an ubiquitous monoterpene emitted from biogenic sources (Geron et al., 2000; Hayward et al., 2001; Ludley et al., 2009; Maleknia et al., 2007; White et al., 2008) and pyrogenic sources (Akagi et al., 2013; Gilman et al., 2015; Hatch et al., 2015). Many studies have reported camphene as a top contributor by mass in measured biogenic and pyrogenic monoterpene emissions (Benelli et al., 2018; Hatch et al., 2019; Komenda, 2002; Mazza & Cottrell, 1999; Moukhtar et al., 2006). For example, in measurements of laboratory and prescribed fires reported by Hatch et al. (2019), camphene was among the top two monoterpenes emitted from subalpine and Douglas fir fires based on emission factors (mass of compound emitted/mass of fuel burned).

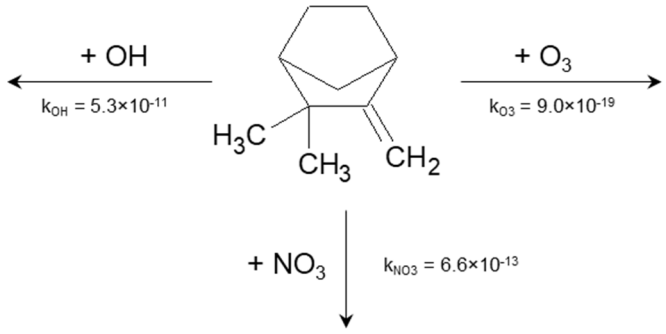

Figure 2-1 Camphene chemical structure and reaction rate constants (unit: cm^3 molecule^{-1} s^{-1}) with major atmospheric oxidants.

When emitted to the atmosphere, monoterpenes form oxygenated compounds through reactions with oxidants such as hydroxyl radicals (OH), ozone (O_3) and nitrate radicals (NO_3); compounds with sufficiently low volatility can then condense to form secondary organic aerosol (SOA). Figure 2-1 shows the chemical structure of camphene and its reaction rate constants with major atmospheric oxidants. The SOA formation potential of individual monoterpenes can vary greatly based on their molecular structure, atmospheric lifetimes, and the volatility of their oxidation products (Atkinson and Arey, 2003; Griffin et al., 1999; Ng et al., 2007a; Zhang et al., 1992). Previous experimental studies of other monoterpenes (such as α-pinene, β-pinene, d-limonene, etc.) have reported SOA mass yields from ~10% to 50% through OH oxidation and from ~ 0 to 65% through NO_3 oxidation; among the studied monoterpenes, d-limonene often has the highest reported yields (Mutzel et al., 2016; Griffin et al., 1999; Ng et al., 2007b; Fry et al., 2014). Few studies have been published regarding camphene SOA formation.

Past experimental studies of camphene largely have been focused on gas-phase reactivity with OH, NO_3, and/or O_3 and gas-phase product identification (e.g., Atkinson et al., 1990; Gaona-Colmán et al., 2017; Hakola et al., 1994). Baruah et al. (2018) performed

a kinetic and mechanism study of the camphene oxidation initiated by OH radicals using density functional theory (DFT), in which the rate constant and atmospheric lifetime were reported. It was also suggested that addition at the terminal double bond carbon atom could account for 98.4% of the initial OH-addition. A product study by Gaona-Colmán et al. (2017) showed obvious NO_x dependence in OH + camphene experiments, in which the molar yield of acetone was enhanced by a factor of 3, 33% relative to 10%, in the presence of NO_x (2–2.3 ppmv of NO).

Hatfield and Huff-Hartz studied SOA formation from ozonolysis of VOC mixtures, in which the added camphene was considered a non-reactive VOC and assumed to have little to no effect on SOA mass yields (Hatfield & Hartz, 2011). Mehra et al. (2020) recently published a compositional analysis study of camphene SOA. Although SOA mass yields were not provided, they demonstrated the potential contribution of highly oxygenated organic molecules (HOMs) and oligomers to camphene SOA formed in an oxidation flow reactor (OFR). Afreh et al. (2020) presented the first mechanistic modeling study of camphene SOA formation. While relatively high SOA mass yields were reported (with final SOA mass and yields twice that of α-pinene), no chamber-based SOA data were available for measurement–model comparison at that time.

SOA formation has been shown to be highly dependent on gas-phase NO_x concentrations; and more precisely, the relative ratios of NO:HO_2, hydroperoxyl radicals:RO_2, peroxy radicals (Henze et al., 2008; Ng et al., 2007b; Presto et al., 2005; Ziemann and Atkinson, 2012; Kroll and Seinfeld, 2008; Song et al., 2005). During chamber experiments, VOCs are subject to oxidation by OH, O_3 and/or NO_3. For some precursors,

NO_x levels influence the amount of SOA produced in the initial oxidation steps by controlling the relative proportions of oxidants, the fractional reactivity with those oxidants, and thus the volatility distribution of the products formed (Hurley et al., 2001; Nøjgaard et al., 2006; Kroll and Seinfeld, 2008). For other precursors, NO_x levels influence the amount of SOA produced via fate of RO_2. The reactions between RO_2 and HO_2 form hydroperoxides, which can have sufficiently low volatility to condense into the particle phase. In the presence of NO_x, RO_2 will react with NO, forming organic nitrate and carbonyl compounds that have higher volatilities than the products formed through the HO_2 pathway (Kroll and Seinfeld, 2008; Ziemann and Atkinson, 2012). Previous studies of relatively small compounds (carbon number $\leq$10), including monoterpenes such as α-pinene, have reported that SOA mass yields generally increase as initial NO_x decreases, with a proposed mechanism of competitive chemistry between $RO_2 + HO_2$ and $RO_2 + NO$ pathways, of which the latter would form more volatile products (Kroll et al., 2006; Ng et al., 2007; Song et al., 2005). The NO_x dependence of camphene oxidation and SOA formation has been relatively understudied.

The atmospheric gas-phase autoxidation of RO_2 has been identified as another key pathway of SOA formation (Crounse et al., 2013; Jokinen 2014; Ehn et al., 2017; Bianchi et al., 2019). The RO_2 radical undergoes intramolecular H-atom abstraction reactions to form a hydroperoxide functionality and an alkyl radical (RO), to which a new RO_2 will be formed by adding O_2. The autoxidation process can repeat several times until terminated by other pathways and will form low-volatility compounds known as highly oxygenated organic molecules (HOMs) (Bianchi et al., 2019). Recent theoretical and experimental

studies have been conducted to understand HOM formation from monoterpenes such as α-pinene and β-pinene (Zhang et al., 2017; Quéléver et al., 2019; Xavier et al., 2019; Pullinen et al., 2020; Ye et al., 2020), but the potential importance and mechanisms of HOM formation from camphene have not been well investigated.

Here, we present the first systematic study of SOA formation from camphene using laboratory-based chamber experiments and chemically detailed box models. The experiments were conducted at varying NO_x levels and the chamber data were used to provide SOA parameterizations based on the two-product (Odum et al., 1996) and volatility basis set (VBS) modeling approaches (Donahue et al., 2006; Donahue et al., 2009). Two chemically detailed box models, Statewide Air Pollution Research Center (SAPRC) and Generator for Explicit Chemistry and Kinetics of Organics in the Atmosphere (GECKO-A), were used to provide mechanistic insights into the chamber observations and to elucidate the connections between the fate of RO_2, HOM forming mechanisms, and camphene SOA formation.

2.2 Methods

2.2.1 Chamber Facility and Instrumentation

The camphene photooxidation experiments were conducted in the University of California, Riverside (UCR) dual indoor environmental chamber. Chamber characterization and features have been previously described in detail (Carter et al., 2005). Briefly, the UCR environmental chamber consists of two 90 m^3 collapsible Teflon reactors (2MIL (0.0508

mm) FEP film) kept at a positive pressure differential (3.73–4.98 Pa) to the enclosure where the reactors are located to minimize contamination during experiments. The enclosure is relative humidity controlled (<0.1%), temperature controlled (300 ± 1 K), and continuously flushed with dry purified air (dew point < -40 °C). Prior to and between experiments, reactors were collapsed to a volume < 20 m^3 for cleaning. The cycle of filling-purging the reactors was repeated until particle number concentrations were < 5 cm^{-3} and NO_x mixing ratios were < 1 ppb. The reactors were then flushed with dry purified air and filled up to 90 m^3 overnight. The filling-purging of the reactors is controlled by an "elevator" program in LabView.

NO and NO_2 mixing ratios were monitored by a Thermo Environmental Instruments Model 42C chemiluminescence NO_x analyzer. O_3 mixing ratios were monitored by a Dasibi Environmental Corp. Model 1003-AH O_3 analyzer. An Agilent 6890 gas chromatograph with flame ionization detector (GC-FID) was used to measure the camphene levels during the experiments.

Multiple instruments were used for particle-phase monitoring. Each reactor was equipped with a scanning mobility particle sizer (SMPS), including a TSI 3081 differential mobility analyzer (DMA), to measure the particle mass concentration. Particle effective density was directly measured by an Aerosol Particle Mass Analyzer (APM, Kanomax) with a SMPS built in house (Malloy et al., 2009). Chemical composition of SOA was measured using HR-ToF-AMS (DeCarlo et al., 2006) and analyzed to obtain O:C and H:C ratios by applying the method of Canagaratna et al. (2015). Data processing was performed using the ToF-AMS Analysis Toolkit 1.57 and PIKA 1.16 on Igor Pro 6.36. A prior

characterization of this UCR chamber system (Li et al., 2016) reported an experimental uncertainty in SOA yields of < 6.65%.

Particle wall loss corrections were performed following the method described in Cocker et al. (2001). Vapor wall loss of organics has been reported in multiple chambers (e.g., Zhang et al., 2015, 2014; Schwantes et al., 2019); and has been modeled as a function of the mass and volatility of the condensing compounds, condensation sink, and characteristics of the chamber (e.g., La et al., 2016; Zhang et al., 2014; Ye et al., 2016). The extent to which these observations and modeling simulations are relevant in the UCR chamber is unclear, given the significant difference in chamber sizes. The UCR chamber is 4.5 times larger (90 m^3) than the largest referenced chamber in these studies (20 m^3) and most are ~10 m^3. In the UCR chamber, the role of vapor wall loss has been investigated in SOA experiments using various precursor compounds (including α-pinene and *m*-xylene) under seed and no seed conditions (Clark et al., 2016; L. Li et al., 2015). There has been no evidence of non-negligible vapor wall loss in those experiments, including no measurable differences in SOA formation in experiments with and without seed. In this work, stability tests on camphene demonstrated negligible vapor wall loss of the parent compound. Thus without evidence to suggest otherwise, negligible vapor wall loss was assumed for these experiments. This assumption is further discussed where it may affect the major conclusions regarding the role of gas-phase chemistry on SOA formation.

2.2.2 Experimental Conditions

A series of 13 camphene photooxidation experiments were carried out under varying levels of camphene and NO_x (Table 2-1). Due to the relatively high melting point of camphene (51 °C), camphene (Sigma-Aldrich, purity > 96 %, FG) was injected into a glass manifold (heated to 50 °C by heating tape) using a preheated (~50-55 °C) microliter syringe. As camphene evaporated it was carried to the reactors by dry purified compressed air flowing through a glass manifold at 8 LPM for 15 mins. Injection lines from the glass manifold to the reactors were also heated to reduce losses of camphene. H_2O_2 (Sigma Aldrich, 50 wt.% in H_2O) was injected by adding 200 µl onto glass wool in glass tubing and then placing the tubing in a 56 °C oven with 10 LPM of dry purified compressed air flowing through the tubing for 15 mins and into the reactors. An inert tracer, perfluorohexane (Sigma-Aldrich, 99 %) or perfluorobutane (Sigma-Aldrich, 99 %), was injected to the reactors through the heated glass manifold by a carrier gas of 50 °C pure N_2. NO (Matheson, UHP) at known volume and pressure was transferred and injected through the same glass manifold as the inert tracer. When gaseous injection of camphene, H_2O_2, inert tracer, and NO (when used) was completed, the reactors were internally mixed using built-in blowers to ensure uniform distribution of chemicals, and then irradiated using UV black lights (115w Sylvania 350BL) to start photooxidation. No seed aerosol was used in this study. All experiments were conducted under dry conditions (relative humidity < 0.1 %) at 300 K. The initial conditions of the experiments are summarized in Table 2-1.

Table 2-1 Summary of initial conditions for chamber experiments and box model simulations.

	Expt.	Initial Conditions for Chamber Experiments and SAPRC Simulations				Initial Conditions for GECKO-A Simulations			
		Camphene (ppb)	Added NO_x (ppb)	*H_2O_2 (ppb)	HC/NO_x (ppb/ppb)	Camphene (ppb)	NO_x (ppb)	H_2O_2 (ppb)	HC/NO_x (ppb/ppb)
without NO_x	WO1	7		854		10		1000	
	WO2	9		1148					
	WO3	28		1212		25		1000	
	WO4	57		1182		50		1000	
	WO5	120		1212		100		1000	
	WO6	223		1576		150		1000	
with NO_x	W1	7	89	854	0.08	10	80	1000	0.13
	W2	25	138	1040	0.18	25	80	1000	0.31
	W3	32	62	1136	0.51				
	W4	43	7	860	5.91	50	80	1000	0.63
	W5	60	94	1227	0.64				
	W6	131	98	1167	1.33	100	80	1000	1.25
	W7	172	60	1121	2.88	150	80	1000	1.88

* H_2O_2 mixing ratio was targeted at 1ppm but corrected based on tracer (perfluorohexane or perfluorobutane) concentration to offset initial reactor volume bias. Corrected H_2O_2 mixing ratios were used in SAPRC modeling.

2.2.3 Model Configurations and Conditions

The chamber experiments were modeled using two different box models, SAPRC and GECKO-A. The SAPRC model was chosen because it has been designed to evaluate gas-

phase chemistry in the UCR chamber. The GECKO-A model was chosen because of the ability to predict both gas and particle phase composition, and the prior work of Afreh et al. (2020), in which GECKO-A was used to study SOA formation from camphene. The initial conditions of the simulations are summarized in Table 2-1.

2.2.3.1 SAPRC

A gas-phase oxidation mechanism was derived using the SAPRC mechanism generation system (MechGen) with modified initial rate constants (camphene with OH, NO_3 and O_3) based on published literature data (Atkinson and Arey, 2003). MechGen, described elsewhere (Carter, 2021; Carter, 2020b; Jiang et al., 2020), is capable of generating fully explicit mechanisms for the atmospheric reactions of many types of organic compounds and the intermediate radicals they form. MechGen uses experimentally derived rate constants and branching ratios if data are available and otherwise uses estimated rate constants and branching ratios based on group additivity and other estimation methods. This system was used to derive reactions of explicit and lumped organic compounds and products in the development of the SAPRC-18 mechanism (Carter, 2020a) and a detailed SAPRC furans mechanism (Jiang et al., 2020).

The MechGen-derived camphene mechanism was implemented into the SAPRC box model to simulate chamber experiments under the same chemical conditions as the chamber experiments, where the initial hydrocarbon concentrations and NO_x levels were as defined in Table 2-1. The SAPRC box model system has been used for chemical mechanism development, evaluation, and box modeling applications since the mid-1970s (Carter, 1990, 1994, 2000, 2010a, 2010b, 2020a). The initial conditions and relevant

chemical parameters for environmental chamber experiments are required inputs; simulations can be performed using multiple versions of the SAPRC gas-phase chemical mechanism. In this work, the recently published version, SAPRC-18 (Carter, 2020a), was selected as the base mechanism because it represents the current state of the science and includes the most up-to-date model species and explicit representation of RO_2 chemistry.

2.2.3.2 GECKO-A

GECKO-A is a nearly explicit mechanism generator and SOA box model. GECKO-A relies on experimental data and structure-activity relationships (SARs) to generate detailed oxidation reaction schemes for organic compounds. The generated reaction schemes are applied in the SOA box model to simulate SOA formation based on the absorptive gas/particle partitioning model of Pankow (1994), where thermodynamic equilibrium between the gas and an ideal particle phase is assumed. Detailed descriptions of GECKO-A, including mechanism generation and SOA formation, are provided by Aumont et al. (2005) and Camredon et al. (2007). GECKO-A has been used to predict SOA in a number of studies (e.g., Aumont et al., 2012; Lannuque et al., 2018; McVay et al., 2016), including camphene (Afreh et al., 2020). Details of the camphene mechanism and SOA box modeling were described in Afreh et al. (2020). Briefly, the camphene mechanism includes 1.3×10^6 reactions and 1.8×10^5 oxidation products; vapor pressures of products were calculated based on the Nannoolal method (Nannoolal et al., 2008).

The GECKO-A simulations were performed for a predefined set of conditions, prior to the chamber experiments, and thus in some cases differ from the experimental conditions. GECKO-A simulations were performed under two NO_x conditions, with 80 ppb of NO_x

and without NO_x (Table 2-1). For both NO_x conditions, the initial hydrocarbon mixing ratios were set at 10, 25, 50, 100, and 150 ppb. All simulations were run under the following initial conditions: 1000 ppb of H_2O_2, 1 μg m^{-3} of organic seed with molecular weight of 250 g mol^{-1}, 298 K temperature, 1% relative humidity, and 50° solar zenith angle (required to compute the photolysis frequencies). Simulation results for camphene were compared with chamber data including SOA mass yields, precursor decay rates, and oxidant levels.

2.3 Experimental and Modeling Results

Table 2-2 summarizes the measured initial NO/NO_2 mixing ratios, initial camphene concentration ($[HC]_0$), reacted camphene concentration ($\Delta[HC]$), SOA mass (M_o) formed, particle density, final peak particle diameter (d_p), photochemical aging time, irradiation time, and SOA mass yield (SOA mass formed, M_o/hydrocarbon reacted, ΔHC) for all 13 experiments. Except for Fig. 2-4, in which SOA mass yields are shown as a function of photochemical age, all SOA mass yields refer to the mass at the end of the experiments (~6 hours). Measured and predicted gas-phase species are presented in Sect. 3.1; SOA mass and yields are presented in Sect. 3.2. The predicted fate of RO_2 in the context of initial HC to initial NO_x mixing ratio ($[HC]_0/[NO_x]_0$) is presented in Sect. 3.3.

Table 2-2 Chamber SOA data, WO indicates experiments without added NO_x and W with added NO_x.

Expt.	Initial NO/NO_2	$[HC]_0$	$\Delta[HC]$	M_o	PM den.	**Peak d_p	Irradiation time	Chemical aging time	SOA mass yield
	ppb	μg m^{-3}	μg m^{-3}	μg m^{-3}	g cm^{-3}	nm	hour	hour	

WO1	0/0	41	41	6.1	1.42	126	4.9	16.1	0.15
WO2	0/0	49	49	3.7	1.42	125	5.0	16.7	0.08
WO3	0/0	155	153	42.0	*1.36	214	6.1	17.7	0.27
WO4	0/0	313	305	84.4	*1.34	270	6.7	15.8	0.28
WO5	0/0	663	597	158.6	1.30	286	6.7	9.5	0.27
WO6	0/0	1230	844	162.4	*1.31	492	6.1	5.0	0.19
W1	86/2	40	40	14.6	1.46	120	5.1	50.6	0.36
W2	114/24	140	140	46.1	1.47	188	5.2	40.6	0.33
W3	51/11	177	177	112.3	*1.44	185	6.0	42.0	0.64
W4	5/2	238	237	96.0	1.35	290	5.9	16.1	0.41
W5	45/49	334	334	199.5	*1.44	430	5.8	33.6	0.60
W6	42/56	724	724	428.8	*1.42	665	5.8	12.7	0.59
W7	45/15	956	950	494.3	*1.39	800	6.4	8.75	0.52

* Estimated using best fit line shown in Fig. 2-17.
** Peak d_p refers to the diameter of particles at the peak of the size distribution plot at the end of the experiment. The uncertainty of peak d_p values is less than 5%.

2.3.1 Gas-Phase Reactivity

Figure 2-2 shows measured and predicted camphene consumption for the 13 photooxidation experiments, and the calculated time-dependent β values (ratio of RO_2 + NO to the sum of RO_2 + NO and RO_2 + HO_2) (Henze et al., 2008; Pye et al., 2010) based on SAPRC predictions for each experimental condition. Additional comparisons of measured and predicted gas-phase species are shown in Fig. 2-12. Higher camphene decay rates and higher OH levels (0.15–0.88 ppt with added NO_x; 0.05–0.29 ppt without added NO_x) were observed and predicted for experiments with added NO_x than without; likely due to the fast recycling of OH when NO_x was present (Fig. 2-2). For all experiments, the

β values changed as a function of time due to changing chemical conditions. Note that due to off-gassing of NO_x from the Teflon reactor (Carter et al., 2005), β values simulated here were larger than 0 even for experiments without added NO_x. Experiments with added NO_x have β values from 0.12–1, while experiments without added NO_x have values < 0.12. For all parameters (camphene consumption, NO_x decay, O_3 formation, and OH levels), the SAPRC simulation results were generally in good agreement with the experimental data. The exception to the generally good agreement was O_3 predictions in experiments without added NO_x, which have a relatively strong dependence on the HONO off-gassing rate. The quantity $\Delta([O_3]-[NO])$ has been used to evaluate the rate of NO oxidation by RO_2 for VOC-NO_x systems in SAPRC mechanism development (Carter and Lurmann, 1990; Carter, 1999; Carter, 2009; Carter, 2020). Figure 2-13 shows the comparison of the $\Delta([O_3]-[NO])$ values between chamber measurements and SAPRC simulations for experiments with added NO_x. The SAPRC box model captures the rates of RO_2+NO well, and supports the use of the SAPRC model to interpret chamber observations especially in the presence of NO_x. Unfortunately, it is hard to quantify how well constrained the other RO_2 reaction rates and product yields are without corresponding measurements, which are not available. In this case, the SAPRC model was largely used to probe the mechanism (diagnostic) and not to predict yields (prognostic).

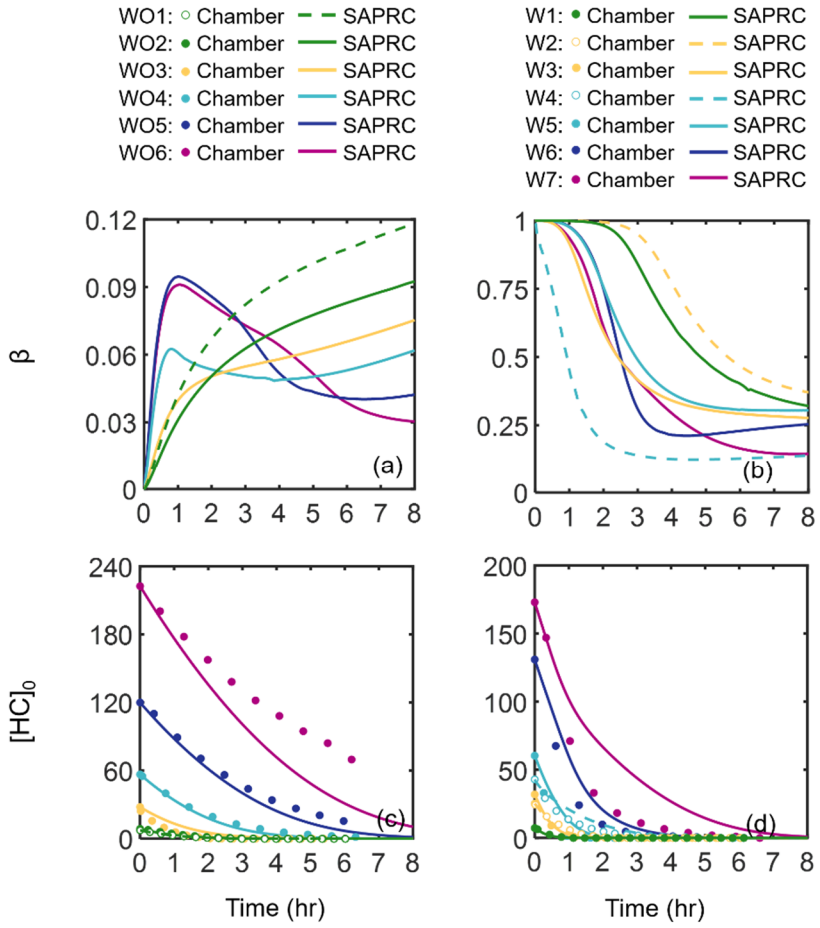

Figure 2-2 SAPRC predicted β values: (a) without added NO_x, and (b) with added NO_x. Measured (circles) and predicted (lines) camphene consumption as a function of irradiation time: (c) without added NO_x, and (d) with added NO_x. The hollow makers used in (c) and (d) are equivalent to dashed lines defined in the legends.

2.3.2 SOA Mass and Yield

Measured SOA mass yields are shown in Fig. 2-3 as a function of SOA mass (M_o) for experiments with (squares) and without (circles) added NO_x. The SOA mass yields were much higher in experiments with added NO_x (0.33–0.64) than experiments without added NO_x (0.08–0.28). The SOA mass yields measured at the lowest $[HC]_0/ \Delta[HC]$ may be an underestimate due to the assumption of negligible vapor wall loss, which would have the largest effect at low Δ[HC] (Krechmer et al., 2020). The observed trends in SOA mass

yields were unexpected based on prior chamber studies of SOA formation from monoterpenes, such as OH oxidation studies of α- and β-pinene, in which SOA mass yields were reported to be suppressed under high-NO_x conditions (Eddingsaas et al., 2012; Pullinen et al., 2020; Sarrafzadeh et al., 2016).

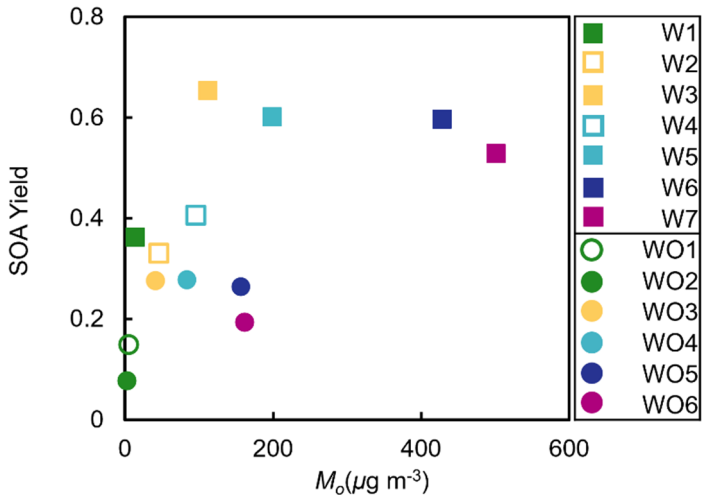

Figure 2-3 Measured camphene SOA mass yields as a function of SOA mass (Mo). Squares indicate experiments with (W) and circles without (WO) added NOx. Initial HC mixing ratios are differentiated by color; open symbols are used to indicate replicate initial HC mixing ratios.

Figure 2-3 shows another unexpected observation: the SOA mass yields decreased at high SOA mass under both NO_x conditions. In the presence of NO_x, the observed SOA mass yields increased with M_o for $M_o \leq 112$ μg m^{-3}, plateaued between 112 μg m^{-3} < $M_o \leq$ 429 μg m^{-3}, and then decreased for $M_o > 429$ μg m^{-3}. Without NO_x, the observed SOA mass yields increased for $M_o \leq 42$ μg m^{-3}, plateaued between 42 μg m^{-3} < $M_o \leq 159$ μg m^{-3}, and then decreased for $M_o > 159$ μg m^{-3}. The difference between the peak SOA mass yield and the SOA mass yield at the highest $[HC]_0$ was ~0.12 with added NO_x and ~0.08 without added NO_x. While the SOA mass yields at the highest $[HC]_0$ may not be statistically different within the uncertainty of the measurements, this trend was also observed in the

GECKO-A model simulations (see Sect. 5) and thus were further investigated, and reasonably explained, by the RO_2 fate based on box model simulations (see Sect. 4 & 5).

The varying [OH] levels in the chamber experiments led to a wide range of photochemical aging times, from hours to days. The irradiation time was converted to equivalent photochemical aging time in the ambient atmosphere using equation (1) (Aumont et al., 2012):

$$\tau = \frac{1}{[\mathrm{OH}]_{\mathrm{atm}}} \int_0^t [\mathrm{OH}]_{\mathrm{sim}} dt \quad (1)$$

where $[OH]_{atm}$ was assumed to be 2×10^6 molecule cm^{-3}. Figure 2-4 shows the measured SOA mass yields as a function of photochemical aging time calculated using OH values predicted by SAPRC ($[OH]_{sim}$). The SOA mass yields are dependent on OH levels and thus photochemical aging time. The yield curves for most experiments plateaued or nearly plateaued by the end of the experiment. Higher $[HC]_0$ generally led to steeper increases in SOA mass yield as a function of aging time. Experiments with added NO_x generally had longer photochemical aging times than experiments without added NO_x; without added NO_x, all experiments may not have fully plateaued and thus would have had higher SOA mass yields at longer irradiation times. However, even at the same aging time (Fig. 2-19), the SOA yields were higher in the experiments with added NO_x. The higher SOA mass yields in experiments with added NO_x may partially be attributed to the difference in [OH] levels and extents of aging. Similar NO_x effects have been reported in many previous studies (e.g., Ng et al., 2007a; Sarrafzadeh et al., 2016). Sarrafzadeh et al. (2016) proposed that in a study of β-pinene the OH level was the main factor that

accounted for differences in SOA mass yields under varying $[NO_x]_0$. In the camphene experiments presented herein, the aging effects were determined to be less important than RO_2 chemistry, since the SOA mass yield curves as a function of photochemical aging already plateau or nearly plateau by the end of experiments (Fig. 2-4) and the shapes of the growth curves (Fig. 2-20 and Fig. 2-21) indicate different kinetics and contributions from oxidation products that form slowly among and between experiments with and without added NO_x (Ng et al., 2006).

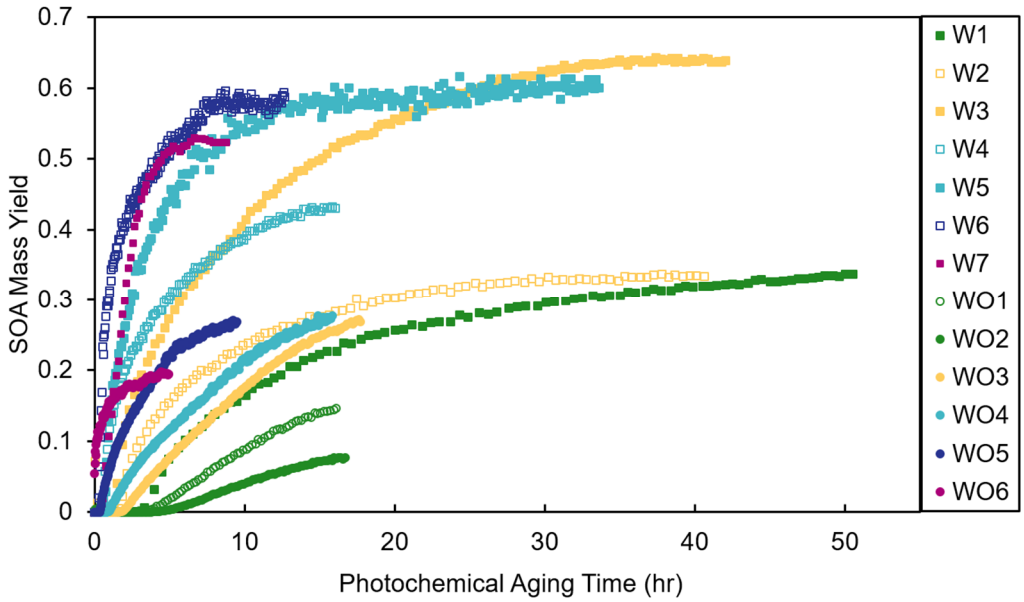

Figure 2-4 Measured SOA mass yields as a function of photochemical aging time in experiments with added NO_x (squares) and experiments without added NO_x (circles).

SOA mass yields are shown as a function of $\Delta[HC]$, $[HC]_0/[NO_x]_0$, and photochemical aging time in Fig. 2-5. For the experiments without added NO_x, a constant value of 1 ppb was used in the calculations of $[HC]_0/[NO_x]_0$ to account for NO_x off-gassing from the Teflon reactors. Based on recent characterization experiments, the UCR chamber has a NO_x off-gassing rate of 2.8 ppt/min in the form of HONO; the camphene experiments

lasted for ~300 to 360 mins. Over low Δ[HC], SOA mass increased in experiments without added NO_x due to the dependence of partitioning on M_o (or Δ[HC]). This trend may be exaggerated due to the assumption of negligible vapor wall loss, which could result in an underestimation of SOA mass yield particularly at low Δ[HC] (Krechmer et al., 2020). The sensitivity of SOA formation to $[HC]_0/[NO_x]_0$ over the range of [HC] sampled is also shown. At a given Δ[HC] level, a lower $[HC]_0/[NO_x]_0$ (when within 0.5–200) led to a higher SOA mass yield (decreasing $[HC]_0/[NO_x]_0$ by ~2 orders of magnitude resulted in a factor of two increase in SOA mass yield). The chamber data presented here indicate that the highest SOA mass yields from camphene were observed in a regime of high Δ[HC] and moderate $[HC]_0/[NO_x]_0$; this regime is distinguished from an extreme $[NO_x]$ regime, proposed in section 4.2, in which SOA mass yields are suppressed at the lowest $[HC]_0/[NO_x]_0$ (also shown in Fig. 2-5). These observations are different from those in studies of α-pinene, in which lower $[HC]_0/[NO_x]_0$ generally led to lower SOA mass yield (Eddingsaas et al., 2012). The observed trends are further explored in the following sections, particularly the role of RO_2 based on SAPRC simulations.

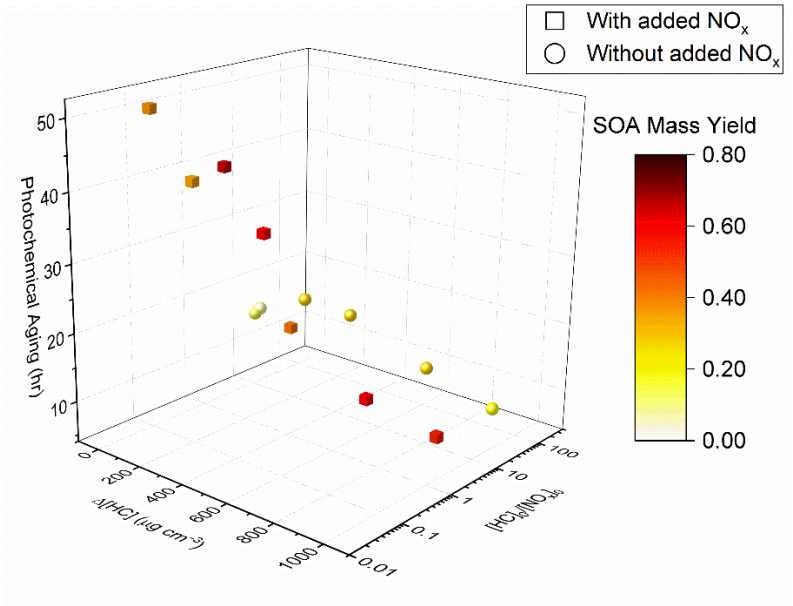

Figure 2-5 SOA mass yield (color bar) as a function of Δ[HC], $[HC]_0/[NO_x]_0$, and photochemical aging time, with added NO_x experiments square markers and without added NO_x experiments round markers.

2.3.3 $[HC]_0/[NOx]_0$ and the Fate of Peroxy Radicals

Table 2-7 shows the experimental $[HC]_0/[NO_x]_0$ and the SAPRC predicted fate of total RO_2 (calculated as the summation of RO_2 radicals that undergo bimolecular reactions) for all the chamber runs. In Fig. 2-6, the fate of total RO_2 is shown as a function of $[HC]_0/[NO_x]_0$. The majority of RO_2 was predicted to undergo bimolecular reactions with HO_2 or NO across the range of $[HC]_0/[NO_x]_0$ values sampled. At $[HC]_0/[NO_x]_0 < 6$, > 50% of the RO_2 was predicted to react with NO; and at $[HC]_0/[NO_x]_0 > 10$, > 50% of the RO_2 was predicted to react with HO_2. A roughly 50:50 branching of RO_2 between NO and HO_2 was reached when $[HC]_0/[NO_x]_0$ was 6:1, which is close to the ratio that was suggested in Presto et al. (2005). When $[HC]_0/[NO_x]_0$ increased over 50, the total fraction of bimolecular $RO_2 + RO_2$ increased from 0 to 30%. In addition, the normalized total RO_2 concentration (total $[RO_2]/[HC]_0$, ppbv/ppbv) increased as $[HC]_0/[NO_x]_0$ decreased (Fig. 2-7), suggesting more

oxygenated RO_2s were formed by NO pathway than others, which is consistent with the formation of HOMs with added NO_x. There is a general trend of increasing SOA mass yield with decreasing $[HC]_0/[NO_x]_0$ (Fig. 2-5 and Fig. 2-7), with the exception of four outliers (W1, W2, WO1, and WO2) that have relatively low SOA mass yields. Experiments WO1, WO2, W1 had the lowest Δ[HC] (49, 41, and 40 μg/m^3, respectively, Table 2-2), indicating the SOA mass yields were influenced by Δ[HC] as well as RO_2 chemistry. The connections between the fate of RO_2 and observed SOA mass yields are further discussed in Sect. 4. Though vapor wall loss has been found to be negligible in previous UCR chamber experiments, such experiments were typically conducted at higher $[HC]_0$. Thus, it is acknowledged that vapor wall loss could affect the measured SOA yields, particularly for experiments W1-2 and WO1-2 with low $[HC]_0$ (or M_o). A vapor wall loss correction for those experiments would increase the measured SOA, but would not affect the following discussion or conclusions regarding the role of RO_2 chemistry.

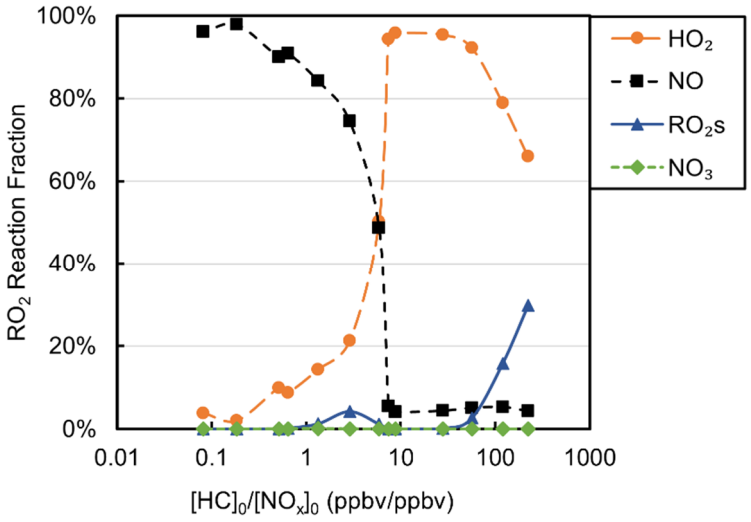

Figure 2-6 Fractions of total RO_2 reactions of each type as a function of $[HC]_0/[NO_x]_0$ based on Table 2-7.

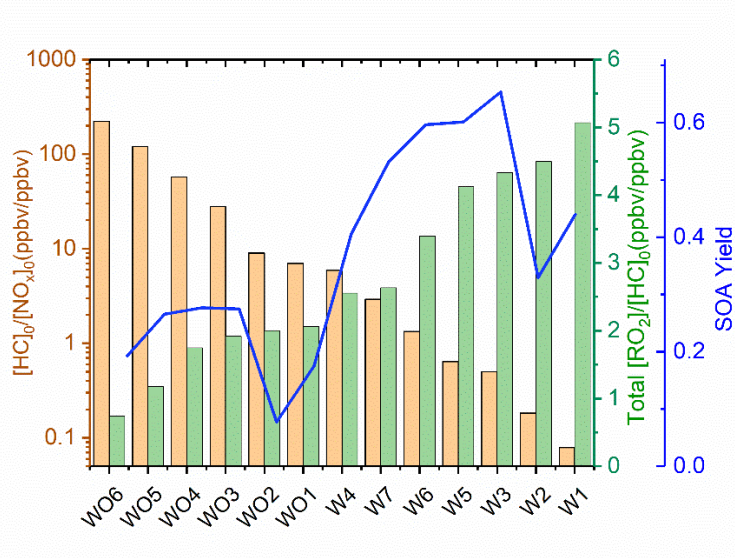

Figure 2-7 Relationship between total $[RO_2]/[HC]_0$, $[HC]_0/[NO_x]_0$, and SOA mass yields.

By assuming the gas-phase chemistry and product distribution were similar when RO_2 + NO accounted for more than 80% of the total RO_2 consumption and when RO_2 + HO_2 accounted for more than 80% of the total RO_2 consumption, experiments with (W1–3, 5–6) and without (WO1–4) added NO_x were grouped and used to derive SOA parameters using the two-product (Odum et al., 1996) and VBS approaches (Donahue et al., 2006; Donahue et al., 2009). The resultant parameters are shown in Table 2-3 (two-product) and Table 2-4 (VBS).

Table 2-3 Two-Product Model SOA parameters.

	α_1	$\log_{10} C^*_1$	α_2	$\log_{10} C^*_2$
Without NO_x	0.0017	1.08	0.3139	0.92
With NO_x	0.4484	1.77	0.2398	-2.94

Table 2-4 VBS Model SOA parameters.

C^*	$^{\dagger}\alpha_{wo}$	$^{\dagger}\alpha_{w}$
0.1	0.0001	0.2657
1	0.0152	0.0008
10	0.3069	0.0357
100	0.0001	0.4222
1000	0.0003	0.0000

† wo refers to without added NO_x; w refers to with added NO_x.

2.4 Discussion

The reaction rate constant of camphene with O_3 is relatively low compared to OH, and thus it is expected that OH is the dominant oxidant in the photooxidation of camphene under chamber conditions, especially with the high initial H_2O_2 (~1 ppm) concentrations. This is supported by SAPRC simulation results (see Fig. 2-14), in which O_3 accounts for 0–3% and NO_3 for 0–16% of camphene oxidation, demonstrating the important role of OH oxidation in these studies.

2.4.1 Camphene + OH Gas-phase Mechanism

Figure 2-8 shows the MechGen predicted reactions and products of OH-initiated oxidation of camphene in the presence of NO_x through one major pathway, which had a yield of 0.83

(a more detailed reaction mechanism schematic is presented in Fig. 2-15). The reaction starts with OH addition to the CH_2=(C) position to form a ring-retaining alkyl radical, which further reacts with O_2 to form the camphene peroxy radical, RO_2-a. RO_2-a can react with oxidants (NO, NO_3, HO_2, and/or other RO_2) to create an alkoxy radical, RO-a, with NO to NO_2 conversion; or form stable products such as organic nitrate (NO3CAMP1), hydroperoxide (HO2CAMP1), and alcohol (RO2CAMP1) compounds. The cyclic alkoxy radical RO-a can undergo prompt beta (β)-scission ring-opening reaction, and then O_2 addition to form another peroxy radical, RO_2-b. In the presence of NO_x, rapid β-scission decomposition, or ring-opening reactions of the camphene alkoxy radicals (RO-b and RO-c) occur through the RO_2 + NO pathway, leading to the generation of the peroxy radical RO_2-d with lower carbon number and higher O:C ratio (increases from 0.30 for RO_2-a to 0.71 for RO_2-d).

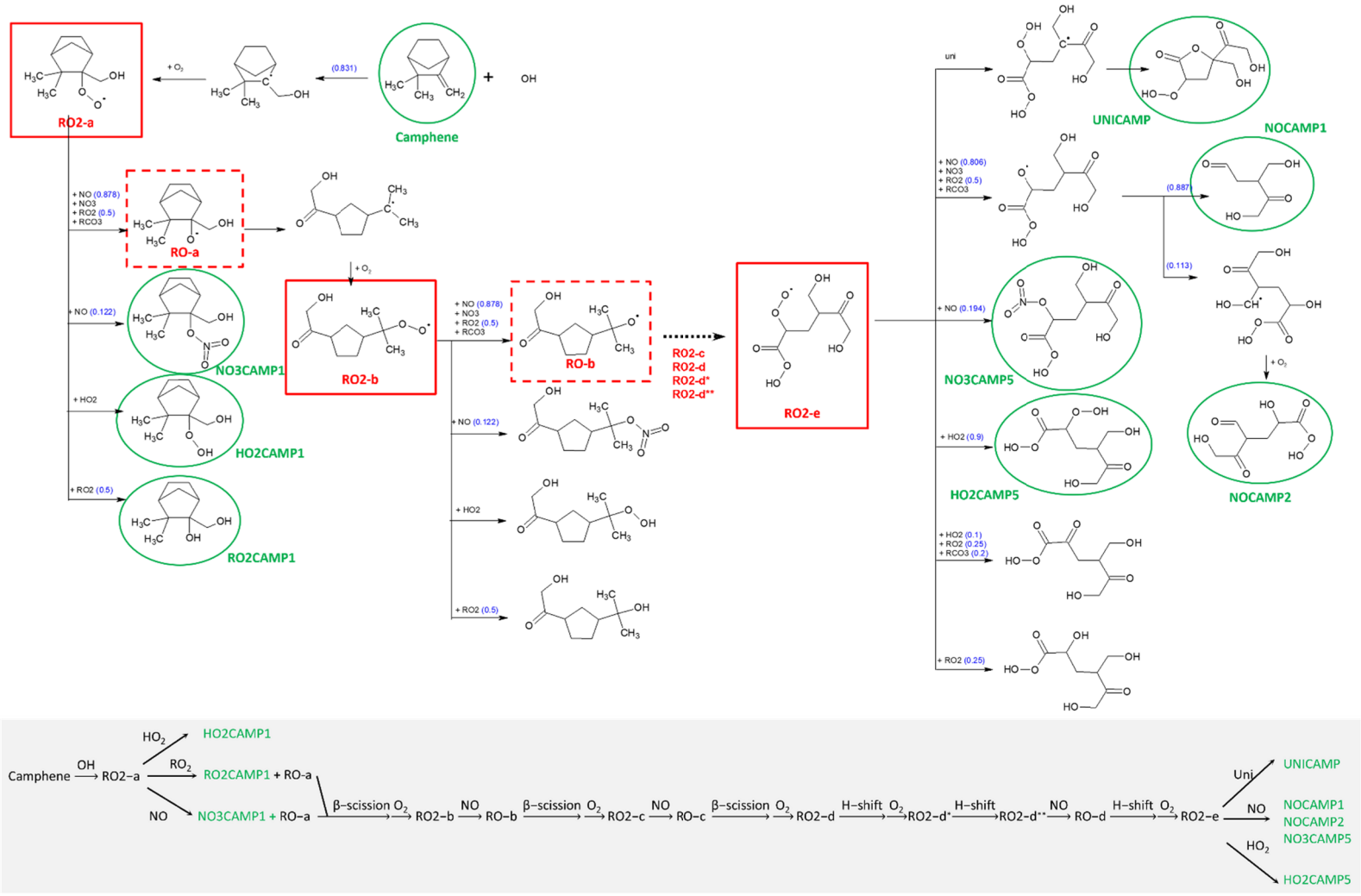

Figure 2-8 Schematic of the OH-initiated oxidation of camphene mechanism in SAPRC at 298 K and atmospheric pressure in the presence of NO_x. Check Fig. 2-15 for more details.

MechGen predicted that RO_2-d could undergo 1,5 H-shift isomerization nearly instantaneously, even in the presence of ~ 100 ppb NO_x. Subsequent rapid addition of O_2 can form a new peroxy radical RO_2-d* which can undergo 1,7 H-shift isomerization and form the peroxy radical RO_2-d**. RO_2-d** can participate in termination reactions with NO and HO_2 to form organic nitrate (NO3CAMP4) and hydroperoxide (HO2CAMP4) products, which are known as highly oxygenated organic molecules (HOMs). In the presence of NO_x, RO_2-d** can also react with NO to form the alkoxy radical RO-d that can undergo 1,4 H-shift isomerization and then O_2 addition to form the new peroxy radical RO_2-e which will also lead to the formation of HOMs such as NO3CAMP5, HO2CAMP5, and UNICAMP. A recent SOA study by Mehra et al. (2020) demonstrated the formation of HOMs in camphene chamber experiments under both low NO_x (30 ppb camphene, ~ 0 ppb NO_x) and medium NO_x (30 ppb camphene, 2.2 ppb NO, 58.4 ppb NO_2) conditions. Based on their observations and analysis, the average molecular formula of the camphene SOA was $C_{7.26}H_{9.85}O_{4.03}$ for low NO_x and $C_{6.63}H_{9.7}N_{0.12}O_{4.21}$ for the medium NO_x conditions, which also suggest the occurrence of ring-opening and decomposition reactions during camphene photooxidation, as predicted by MechGen.

2.4.2 The Formation of HOMs and Influence on SOA Yields

Table 2-5 Log_{10} C^* value for selected 1st generation of stable end products formed from camphene reactions with OH.

Species	Atom				O:C	log_{10} C^*	Species	Atom				O:C	log_{10} C^*
	C	H	O	N				C	H	O	N		
HO2CAMP1	10	18	3	0	0.30	2.5	NO3CAMP1	10	17	4	1	0.40	3.5
HO2CAMP2	10	18	4	0	0.40	1.7	NO3CAMP2	10	17	5	1	0.50	2.6
HO2CAMP3	7	12	4	0	0.57	2.5	NO3CAMP3	7	11	5	1	0.71	3.5
HO2CAMP4	7	12	7	0	1.00	-1.3	NO3CAMP4	7	11	8	1	1.14	-0.1
HO2CAMP5	7	12	8	0	1.14	-4.3	NO3CAMP5	7	11	9	1	1.29	-2.8
RO2CAMP1	10	18	2	0	0.20	3.8	NOCAMP1	6	10	4	0	0.67	2.6
UNICAMP	7	10	7	0	1.00	-3.9	NOCAMP2	7	10	7	0	1.00	-1.1

Table 2-6 Fractions of peroxy radical RO_2-a reactions of each type, calculated based on SAPRC simulations.

Expt.	$[HC]_0$ (ppb)	*$[HC]_0/[NO_x]_0$ (ppbv/ppbv)	SOA Mass Yield	Fraction of RO_2-a Reaction				
				NO	HO_2	RCO_3	RO_2	NO_3
WO1	7	7	0.15	0.03	0.97	0	0	0
WO2	9	9	0.08	0.02	0.98	0	0	0
WO3	28	28	0.27	0.02	0.97	0	0	0
WO4	57	57	0.28	0.03	0.89	0	0.08	0
WO5	120	120	0.27	0.03	0.64	0.02	0.30	0
WO6	223	223	0.19	0.03	0.54	0.02	0.41	0
W1	7	0.08	0.36	1.00	0	0	0	0
W2	25	0.18	0.33	1.00	0	0	0	0
W3	32	0.51	0.64	0.97	0.03	0	0	0
W4	43	5.91	0.41	0.46	0.53	0.01	0	0
W5	60	0.64	0.60	0.97	0.03	0	0	0
W6	131	1.33	0.59	0.88	0.12	0.01	0.01	0
W7	172	2.88	0.52	0.65	0.30	0.03	0.01	0

*The $[HC]_0/[NO_x]_0$ for WO1–6 experiments were estimated assuming 1 ppb of NO_x.

Table 2-5 lists the log *C** values and O:C ratios for the major camphene products predicted; vapor pressures of products were calculated based on the Nannoolal method (Nannoolal et al., 2008). HOMs have much lower volatilities than the earlier terminal products such as NO3CAMP1, HO2CAMP1, and RO2CAMP1. HOMs formed by autoxidation steps in camphene radical chain reactions are mediated by the H-shift isomerization of RO_2-d and RO-d. Table 2-6 shows the SAPRC predicted fate of RO_2-a for all chamber runs; the fate of summed RO_2 is shown in Table 2-7, which includes RO_2-a~d and all the RO_2 radicals formed from other minor pathways. For the experiments without

added NO_x (WO1–6), once the initial peroxy radical RO_2-a was formed, a large fraction of RO_2-a (0.54-0.98) quickly reacted with HO_2 to form the terminal product HO2CAMP1, while only 2–3% of RO_2-a reacted through the NO pathway and led to the generation of HOMs. For the experiments with added NO_x (W1–7), much higher RO_2-a + NO fractions (0.65–1.00) were predicted by SAPRC. The fates of summed RO_2 also suggested that not only RO_2-a, but also the other RO_2 radical intermediates would tend to favor further reactions through the NO reaction chain to form lower volatility products.

Based on the predicted fate of RO_2 in SAPRC simulations, the higher SOA mass yields in experiments with NO_x were due to the formation of HOMs through autoxidation in the presence of NO_x. In general, faster RO_2 reaction with NO, HO_2 or other RO_2 limits HOM formation by autoxidation (Bianchi et al., 2019). In previous monoterpene SOA studies, HOM formation was often observed when NO_x was absent or under lower NO_x conditions (Pye et al., 2019; Schervish and Donahue, 2020; Zhao et al., 2018). For example, Zhao et al. (2018) demonstrated that autoxidation for some RO_2 is competitive with RO_2 + NO at ppb levels of NO for O_3-initiated α-pinene oxidation. They also reported that HOM formation decreased as the initial NO concentration increased from 0 ppb to 30 ppb. In the camphene experiments presented herein, the reverse trend was observed (see experiments WO4, W4 and W5 conducted with ~50 ppb camphene at different NO_x levels). This was due to the key RO_2 species, RO_2-d, which was predicted to form only in the presence of NO_x and had a fast enough autoxidation rate constant to effectively compete with bimolecular reactions.

While the decreasing SOA mass yields at high $[HC]_0$ and M_o in experiments with and without added NO_x (shown in Fig. 2-3) may not be statistically different within the uncertainty of the measurements, RO_2 chemistry was explored as an explanation for the apparent trends. For experiments with added NO_x, a shift in the RO_2 reaction pathways from NO to HO_2 can explain the decreasing SOA mass yields. The fraction of RO_2-a + NO decreased from 0.97 (W5) to 0.65 (W7) while the fraction of RO_2-a + HO_2 increased from 0.03 (W5) to 0.3 (W7). For the experiments without NO_x, the shift from RO_2 + HO_2 to self- and cross-reactions of RO_2 at high $[HC]_0$ and M_o can explain the decreasing SOA mass yields. When $[HC]_0$ increased from 57 ppb to 223 ppb, the fractions of RO_2-a + HO_2 decreased from 0.89 (WO4) to 0.54 (WO6) and the fraction of RO_2-a + RO_2 increased by a factor of five, from 0.08 to 0.41. Moreover, this shift from bimolecular reactions with HO_2 to RO_2 as $[HC]_0$ increased also occurred in the context of the total RO_2 (Table 2-7). Generally, products that were predicted to form from one RO_2 reacting with another RO_2 in the absence of NO_x, had relatively higher volatility than those formed from that RO_2 reacting with HO_2; for example, RO2CAMP1 formed from RO_2-a + RO_2 was more volatile than HO2CAMP1 formed from RO_2-a + HO_2 (Table 2-5). The increasing fraction of self- and cross-reactions of RO_2 therefore is one likely explanation for the decreasing SOA mass yields at high ΔHC and M_o in the experiments without NO_x.

The relatively low SOA mass yields in experiments W1 and W2 (0.36 and 0.33), also can be explained due to differences in product distribution. An underestimation of the SOA mass yields in these experiments due to the assumption of negligible wall loss is not sufficient to explain these relatively low yields. A comparison of the product distributions

between W1, W2, W3 and W5 suggested similar yields of NO3CAMP1–5 and NOCAMP1–2, but major differences in yields of UNICAMP and HO2CAMP1–5 (Fig. 2-16). Experiments W3 and W5 were selected for comparison because of their closest total RO_2 fractional reaction distribution (approximately 90% RO_2 + NO and 10% RO_2 + HO_2) to W2 (98% RO_2 + NO and 2% RO_2 + HO_2) and W1 (96% RO_2 + NO and 4% RO_2 + HO_2) but higher SOA mass yield (0.64 and 0.6). W1 and W2 were predicted to have much smaller SOA mass yield than W3 and W5 in the low volatility products HO2CAMP1–5 (especially product HO2CAMP5, the lowest volatility among all listed products in Table 2-5, $\log_{10}C^* = -4.3$) and UNICAMP (the second lowest volatility shown in Table 2-5, $\log_{10}C^* = -3.9$), which can contribute to the lower SOA mass yield. Further analysis of W1 and W2 revealed a likely cause for the different yields of HO2CAMP1–5 and UNICAMP. W1 and W2 were predicted to have delayed peaks of [OH] (after 3–4 hours of irradiation) which likely was due to the high NO_x concentrations (Fig. 2-12b). Correspondingly, the [HO_2] was highly suppressed during the first 2 hours of irradiation. Under high [NO_x], the RO_2-e + HO_2 pathway shown in Fig. 2-8 therefore could be suppressed, resulting in a lower yield of HO2CAMP5. This indicates a second "extreme NO_x" regime may exist at high [NO_x] and significantly lower $[HC]_0/[NO_x]_0$.

2.5 GECKO-A simulations

2.5.1 SOA Mass and Yield

The comparison of gas- and particle-phase species between chamber experiments and GECKO-A model simulations are shown in Fig. 2-12a and Fig. 2-12b. Without added NO_x, GECKO-A predicts much smaller camphene consumption rates and no O_3 formation, while both the chamber data and SAPRC simulations suggest a final O_3 mixing ratio of ~10 ppb (Fig. 2-12a). This may be due to an underrepresentation of data and relevant pathways for low to no NO_x conditions in the GECKO-A mechanism generation system, and the incomplete treatment of wall effects in the application of the GECKO-A box model. The without added NO_x simulations therefore are not further discussed. With added NO_x, GECKO-A shows good agreement with the experimental data and SAPRC simulations in the context of camphene consumption, O_3, and OH levels.

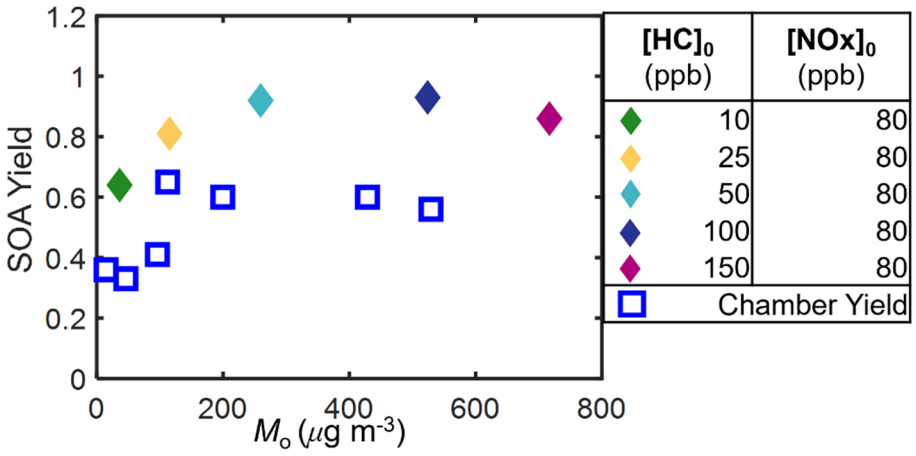

Figure 2-9 Predicted SOA mass yields based on GECKO-A model simulations.

Figure 2-9 shows the predicted SOA mass yields based on GECKO-A. For simulations with added NO_x, while the model predicted higher SOA mass yields (0.64–0.93) than were

observed (0.33–0.64), the trends in the SOA mass yields were consistent between chamber observation and simulations. The simulated SOA mass yield increased with SOA mass for SOA mass < 260μg m^{-3}, plateaued for SOA mass between 260 and 524 μg m^{-3}, and then decreased for SOA mass > 524 μg m^{-3}.

The predicted O:C ratio and average carbon number (Fig. 2-10), defined as the mole-weighted averaged carbon number for the main products (~95% by mass), were consistent with the plateauing/decreasing SOA yields at higher $[HC]_0$ (Fig. 2-9). The average carbon number was calculated using equation (2):

$$\text{Average carbon number} = \frac{\sum_i \frac{n\mathrm{C}_i \times M_{\mathrm{o},i}}{\mathrm{MW}_i}}{\sum_i \frac{M_{\mathrm{o},i}}{\mathrm{MW}_i}} \quad (2)$$

where $n\mathrm{C}_i$, $M_{\mathrm{o},i}$, and MW_i are the carbon number, mass, and molecular weight of species i, respectively. With added NO_x, the average carbon number of both the gas and particle phases increased as $[HC]_0$ increased, while the O:C ratio decreased. These trends indicate there is a significant fraction of higher volatility compounds formed that contribute to SOA at higher $[HC]_0$ (or M_o), resulting in lower SOA mass yields. In addition, only at the highest two $[HC]_0$ were non-negligible fractions of precursor predicted to react with O_3 and NO_3 (Fig. 2-18), suggesting a larger fraction of higher-volatility nitrogen-containing products. More detailed comparisons of GECKO-A simulations with chamber experiments are presented by Afreh et al. (2020) for camphene and McVay et al. (2016) for α-pinene.

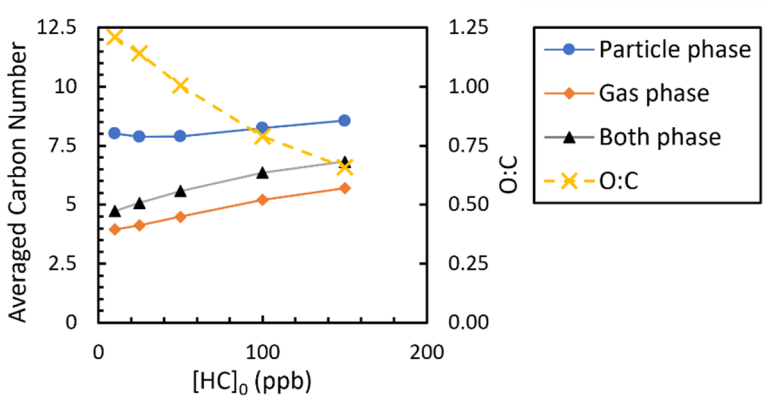

Figure 2-10 GECKO-A predicted particle O:C and mole-weighted averaged carbon number of products with added NO_x.

2.5.2 Particle Density and O:C

Figure 2-11a shows the GECKO-A predicted O:C ratio and measured O:C ratio as a function of $[HC]_0/[NO_x]_0$ for all experiments. A good agreement in O:C ratios was observed between the model predictions and chamber data. The O:C ratio decreased from 1.21 to 0.39 as $[HC]_0/[NO_x]_0$ increased from 0.13 to 223, supporting that more highly oxygenated products were formed at lower $[HC]_0/[NO_x]_0$.

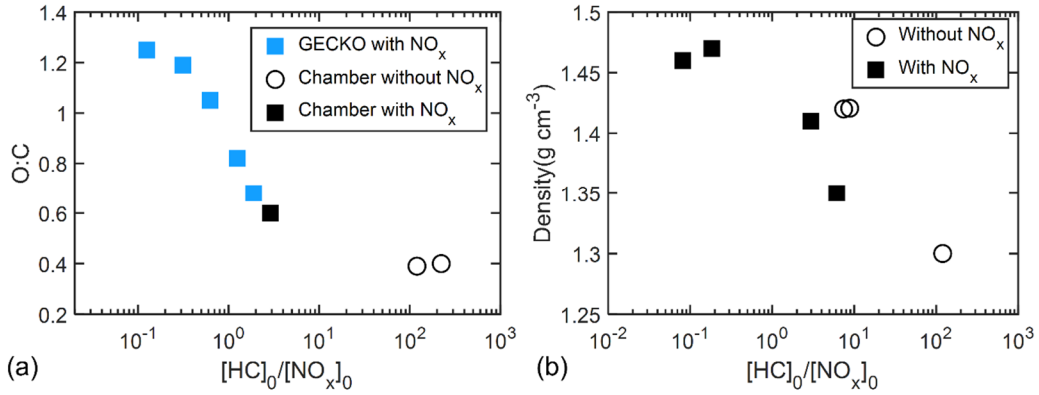

Figure 2-11 (a), O:C ratio as a function of $[HC]_0/[NO_x]_0$ with AMS data and prediction by GECKO-A simulation. (b), Particle density (directly measured by APM–SMPS) shown as a function of $[HC]_0/[NO_x]_0$.

A negative correlation was also observed between measured particle density and $[HC]_0/[NO_x]_0$. The final density of particles decreased from 1.47 g cm^{-3} to 1.30g cm^{-3} as $[HC]_0/[NO_x]_0$ increased from 0.08 to 120 (Fig. 2-11b). The change in O:C ratio could account for the change in density. O:C and H:C have been used in semi-empirical SOA density parameterizations (Nakao et al., 2013; Kuwata et al., 2012), in which O:C plays a dominant role in determining organic particle density compared to H:C. Consistent with the semi-empirical formulations, the density of particles formed from oxidation of camphene increased as O:C increased (from 0.39 to 1.21), while H:C varies over a smaller range (from 1.42 to 1.79). The change in density supports the proposed explanation that more oxygenated products were formed under lower $[HC]_0/[NO_x]_0$. The wide range in final density and the correlation with $[HC]_0/[NO_x]_0$ shown here has not been previously reported. The SOA mass of each experiment in this study was calculated with its own density of SOA, instead of applying an averaged density. A list of particle densities used in this study can be found in Table 2-2.

2.6 Conclusions

The first SOA mass yields from oxidation of camphene based on experiments performed in UCR environmental chamber with varying $[NO_x]_0$ are presented herein. Higher SOA mass yields were measured with added NO_x (0.33–0.64) than without added NO_x (0.08–0.26) at atmospherically relevant OH concentrations. SOA formation from the oxidation of camphene showed different NO_x dependence than what has previously been reported for other monoterpenes (e.g., α-pinene, d-limonene) and n-alkanes (carbon≤ 10), in which higher SOA mass yields were measured when $[NO_x]$ was lower (Nøjgaard et al., 2006; Ng et al., 2007b). For camphene oxidation, higher Δ[HC] and lower $[HC]_0/[NO_x]_0$ (within 0.5–200) generally led to higher SOA mass yields. Similar NO_x dependence has been observed for two sesquiterpenes (longifolene and aromadendrene) but was attributed to the production of nonvolatile organic nitrates with no detailed mechanistic analysis provided at that time (Ng et al., 2007b).

Although $[HC]_0/[NO_x]_0$ shows clear correlation with SOA mass yield, this quantity cannot completely represent the underlying RO_2 chemistry. The RO_2 chemistry and the competition between varying bimolecular RO_2 and unimolecular RO_2 reaction pathways, explored using SAPRC MechGen, can be used to explain the dependence of SOA mass yields on HC and NO_x. The RO_2 + NO pathway favored in experiments with added NO_x formed HOMs with much lower volatilities than products formed in other pathways. In addition to the regular NO_x regime introduced above ($[HC]_0/[NO_x]_0 > 0.5$), the results suggested an extreme NO_x regime where high $[NO_x]$ may suppress SOA mass yield. High NO_x levels may suppress HO_2 levels at the beginning of the experiments, causing a

subsequent reduction in the yields of low volatility products such as UNICAMP and HO2CAMP5. This suggests that if the reactions happened in NO_x-rich environments with extremely high ratios of NO to HO_2 (NO/HO_2), the SOA mass yield from oxidation of camphene might be significantly suppressed. As demonstrated here, simulations with chemically detailed box models such as SAPRC are useful for identifying SOA formation regimes.

Overall, SOA formation from oxidation of camphene may be larger in polluted environments (e.g., urban environments) than NO_x-free environments. This reveals a possible underestimation of SOA formed from oxidation of camphene and potentially other VOCs that are assumed to have lower SOA mass yields at higher NO_x levels. Further chamber and modeling studies of other understudied VOCs will be important for identifying other systems in which moderate NO_x levels can promote HOM formation.

2.7 Appendix

Table 2-7 Weighted fractions of total peroxy radical bimolecular reactions of each type, calculated based on SAPRC simulations.

Expt.	$[HC]_0$ (ppb)	$[HC]_0/[NO_x]_0$ (ppbv/ppbv)	SOA Yield	Total RO_2[a] (ppb)	Fraction of total RO_2 Reaction			
					NO	HO_2	NO_3	RO_2s[b]
WO1	7	7	0.15	15	0.06	0.94	0.00	0.00
WO2	9	9	0.08	18	0.04	0.96	0.00	0.00
WO3	28	28	0.27	54	0.04	0.95	0.00	0.00
WO4	57	57	0.28	99	0.05	0.92	0.00	0.03
WO5	120	120	0.27	141	0.05	0.79	0.00	0.16
WO6	223	223	0.19	165	0.04	0.66	0.00	0.30
W1	7	0.08	0.36	37	0.96	0.04	0.00	0.00
W2	25	0.18	0.33	114	0.98	0.02	0.00	0.00
W3	32	0.51	0.64	139	0.90	0.10	0.00	0.00
W4	43	5.91	0.41	110	0.49	0.50	0.00	0.01
W5	60	0.64	0.60	249	0.91	0.09	0.00	0.00
W6	131	1.33	0.59	445	0.84	0.14	0.00	0.01
W7	172	2.88	0.52	455	0.74	0.21	0.00	0.04

[a] Total RO_2 is calculated as the summation of RO_2 that undergo bimolecular reactions.

[b] "RO_2s" refers to the sum of RO_2 reacting with RO_2 and with RCO_3.

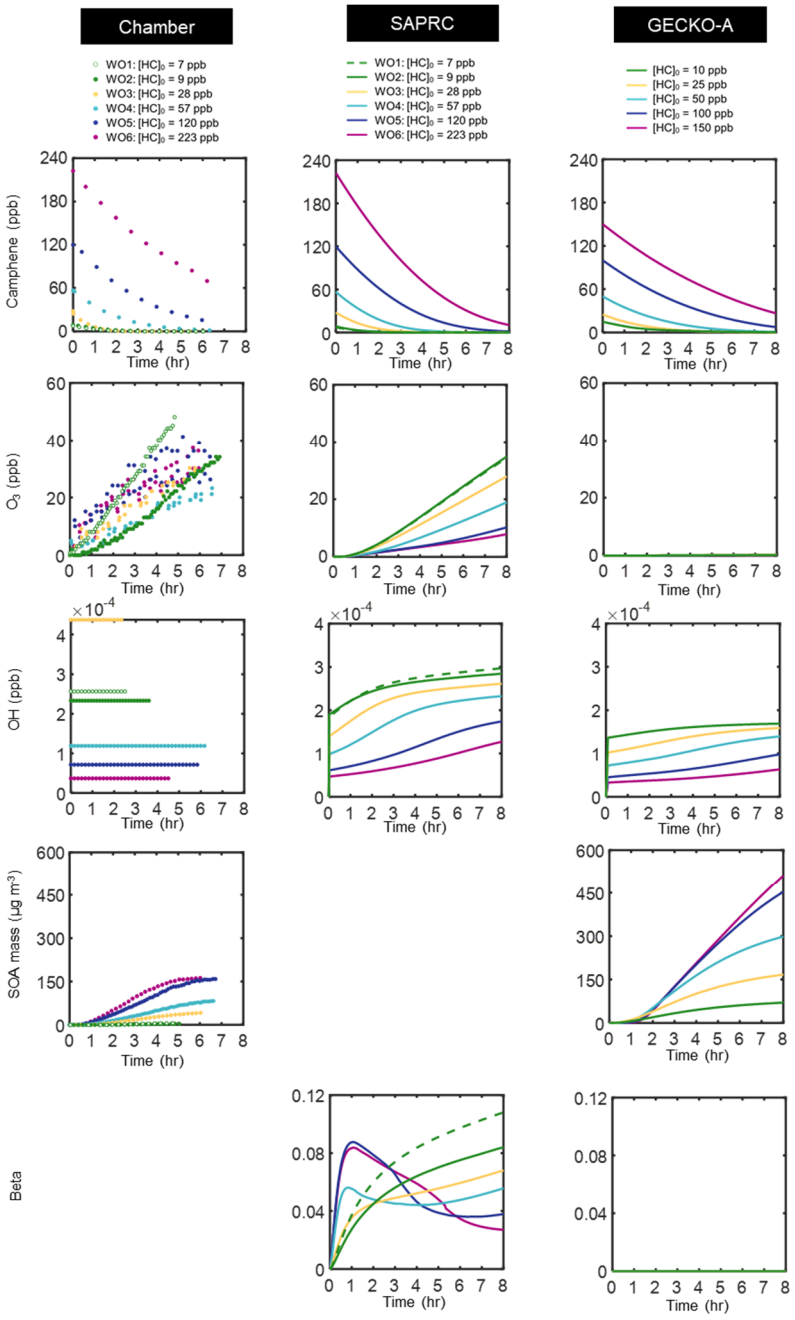

Figure 2-12a Comparison of chamber data (circles) and model simulation results (lines) for the photooxidation of camphene (without added NO_x). Regarding the missing figures, the SAPRC box model used does not calculate SOA formation and measurement data are insufficient to calculate beta values. The chamber OH mixing ratio was calculated as follows:

$$[OH]_{exp} = \frac{\frac{d[cam]_{exp}}{dt} - k_{cam,O_3}[cam]_{exp}[O_3] - k_{cam,NO_3}[cam]_{exp}[NO_3]_{exp}}{k_{cam,OH}[cam]_{exp}}$$

, assuming $[NO_3]_{exp} \approx [NO_3]_{sim}$, chamber [OH] was averaged over the duration of the experiment or until consumption of camphene was complete.

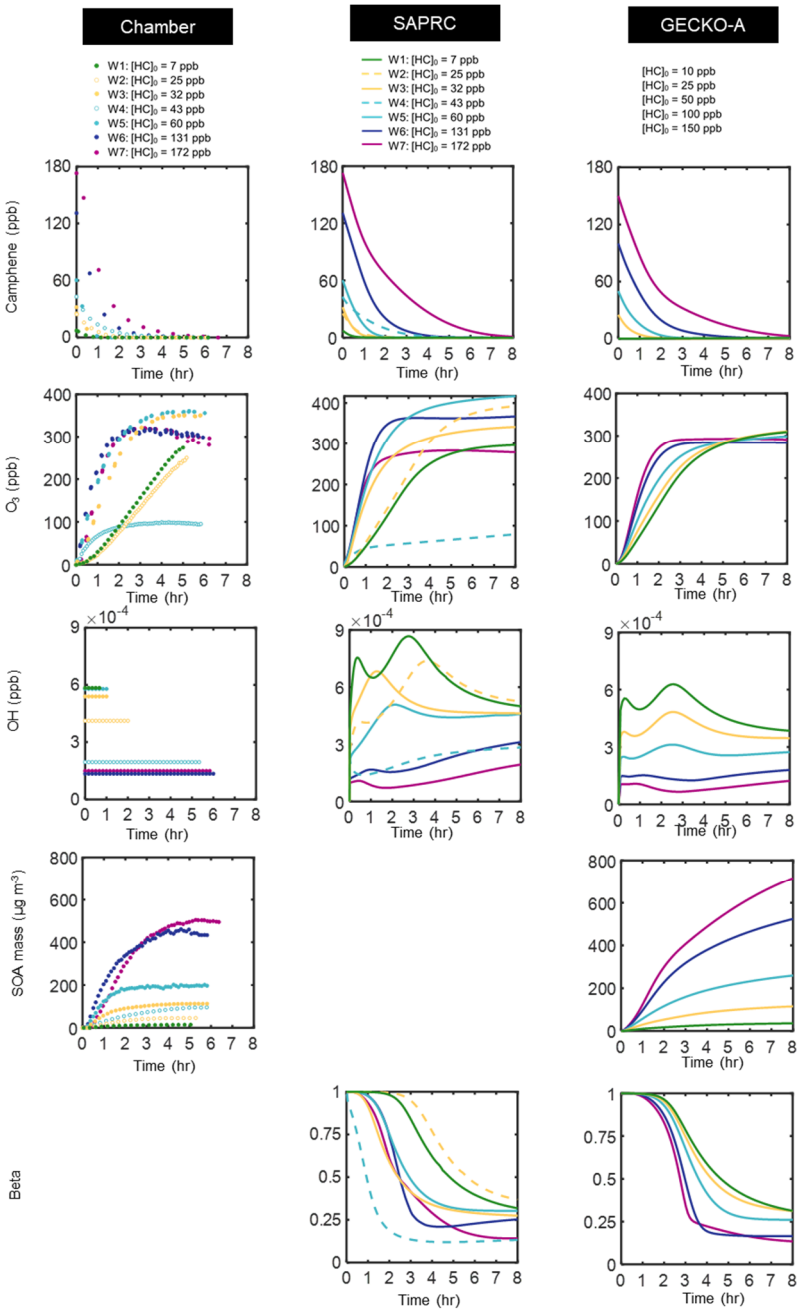

Figure 2-12b Comparison of chamber data (circles) and model simulation results (lines) for the photooxidation of camphene (with added NOx). Regarding the missing figures, the SAPRC box model used does not calculate SOA formation and measurement data are insufficient to calculate beta values. The chamber OH mixing ratio was calculated as follows:

$[\mathbf{OH}]_{\mathbf{exp}} = \frac{\frac{d[\mathbf{cam}]_{\mathbf{exp}}}{dt} - k_{\mathbf{cam,O_3}}[\mathbf{cam}]_{\mathbf{exp}}[\mathbf{O_3}] - k_{\mathbf{cam,NO_3}}[\mathbf{cam}]_{\mathbf{exp}}[\mathbf{NO_3}]_{\mathbf{exp}}}{k_{\mathbf{cam,OH}}[\mathbf{cam}]_{\mathbf{exp}}}$**, assuming** $[\mathbf{NO_3}]_{\mathbf{exp}} \approx [\mathbf{NO_3}]_{\mathbf{sim}}$**, chamber [OH] was averaged over the duration of the experiment or until consumption of camphene was complete.**

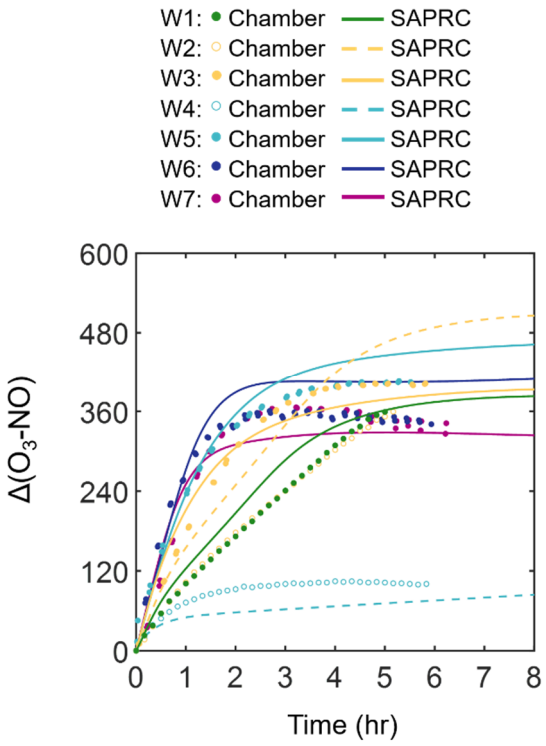

Figure 2-13 Comparison of the chamber data (circles) and SAPRC model simulation results (lines) for camphene photooxidation experiments with added NO_x.

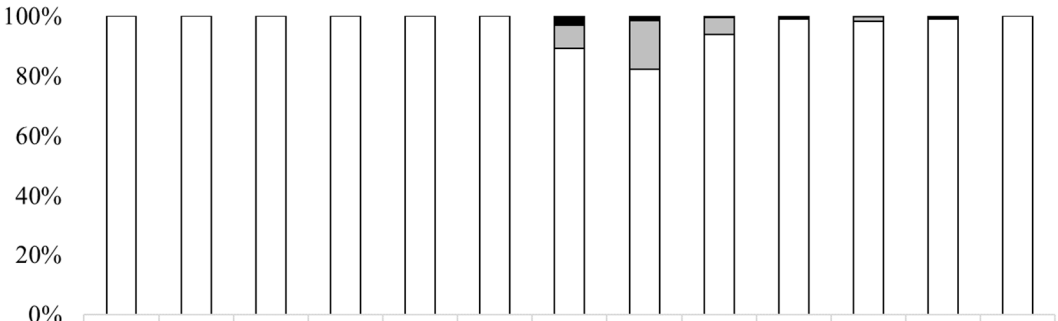

	WO1	WO2	WO3	WO4	WO5	WO6	W1	W2	W3	W4	W5	W6	W7
■O3	0.00	0.00	0.00	0.00	0.00	0.00	0.03	0.02	0.00	0.00	0.00	0.00	0.00
▨NO3	0.00	0.00	0.00	0.00	0.00	0.00	0.08	0.16	0.06	0.01	0.02	0.00	0.00
□OH	1.00	1.00	1.00	1.00	1.00	1.00	0.89	0.82	0.93	0.99	0.98	0.99	1.00

Figure 2-14 Fractional precursor reactivity for each experiment (with added NOx and without added NOx) based on SAPRC simulations.

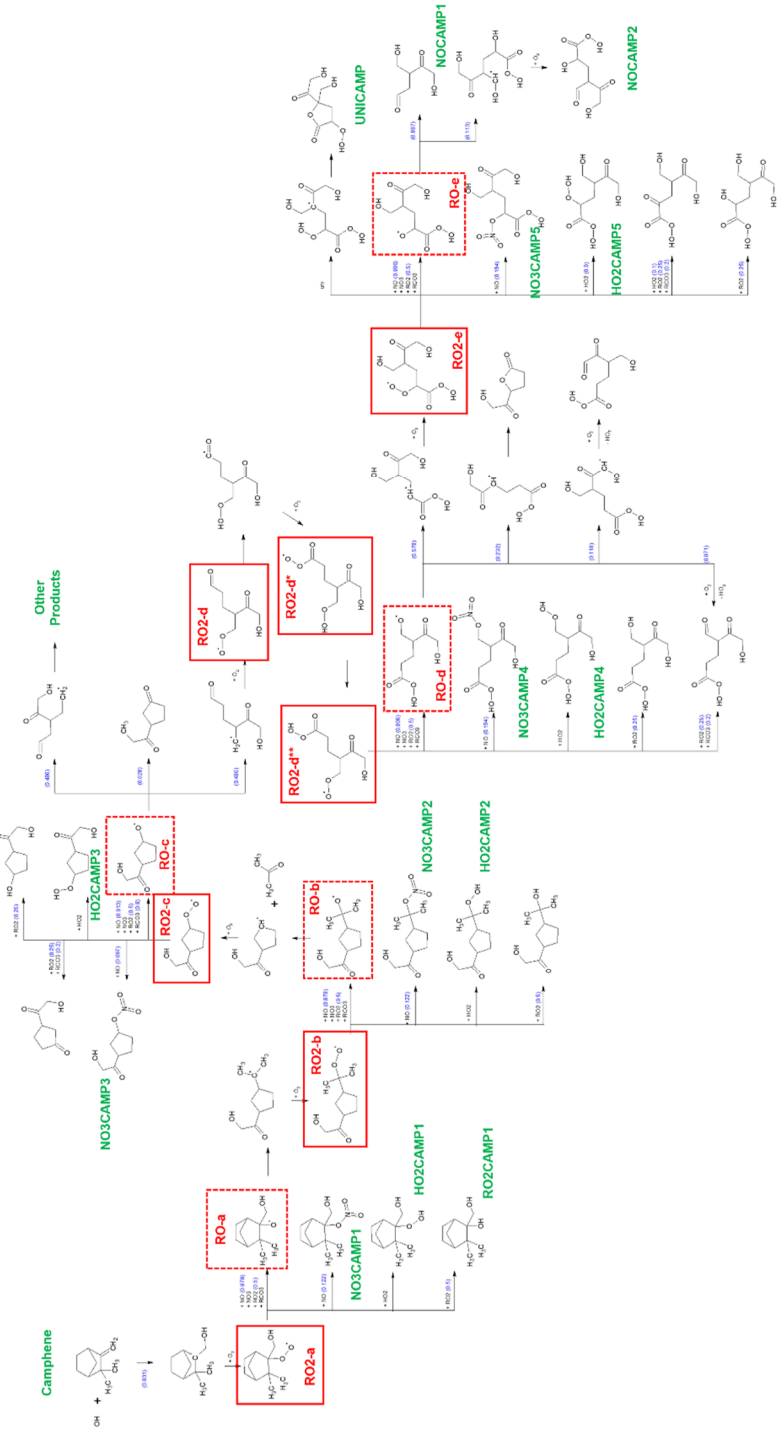

Figure 2-15 Detailed schematic of the OH-initiated oxidation of camphene at 298 K and atmospheric pressure with added NOx as in SAPRC.

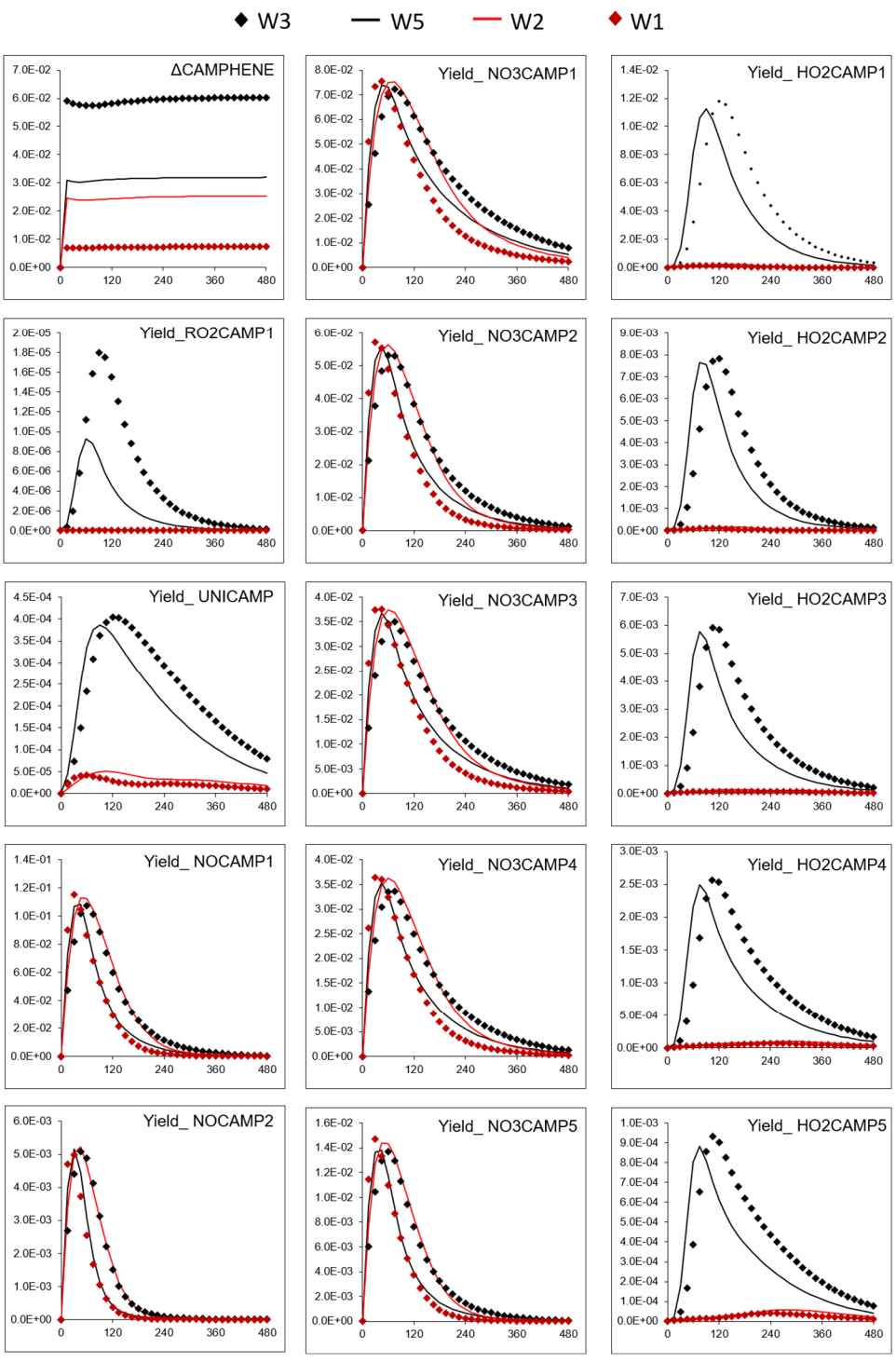

Figure 2-16 Time-resolved product yield distributions for W3, W5, W1 and W2 predicted by SAPRC. The yield of the product is calculated as: $\mathbf{Yield} = \Delta[\mathbf{product}]/\Delta[\mathbf{camphene}]$.

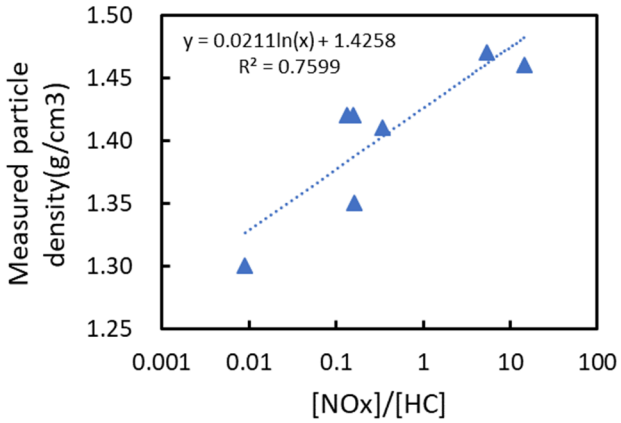

Figure 2-17 Fit function for measured particle density as a function of [NOx]0/[HC]0.

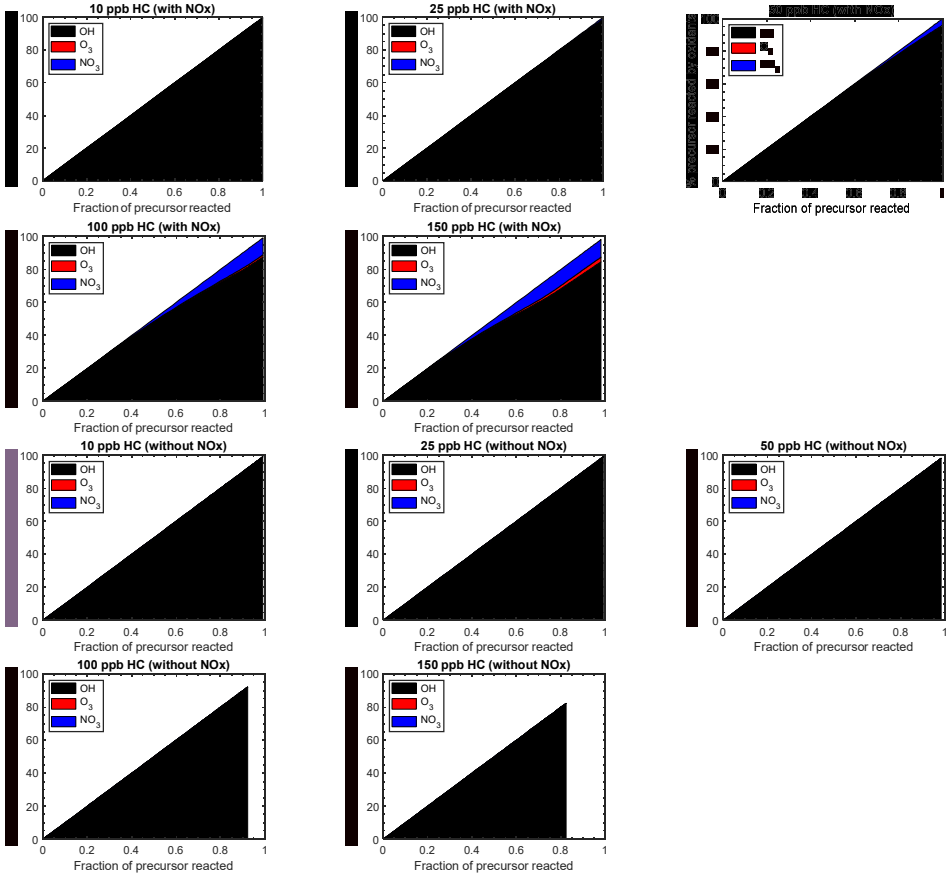

Figure 2-18 Fractional precursor reactivity as predicted by GECKO-A (for experiments with added NOx and without added NOx).

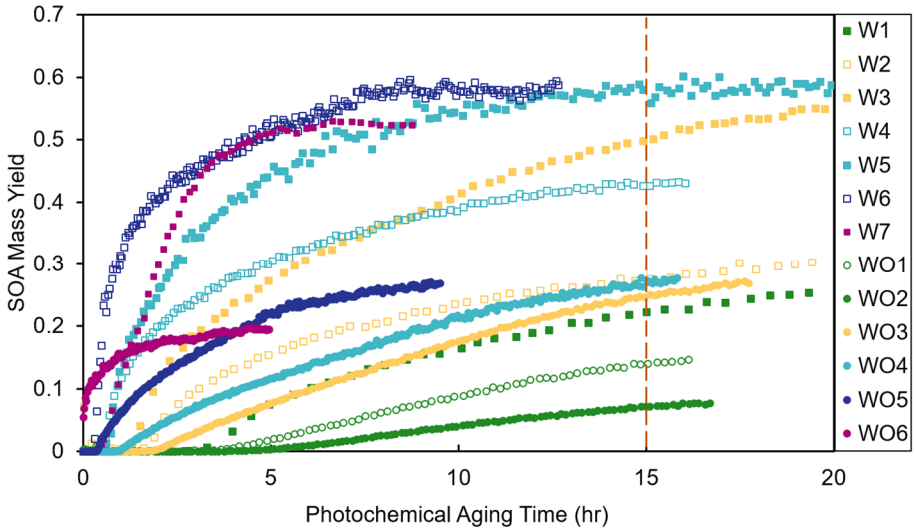

Figure 2-19 SOA mass yields as functions of photochemical aging time in experiments with added NO_x (squares); and experiments without added NO_x (circles) **with cutoff line at 15 hours to highlight a single aging time across experiments**.

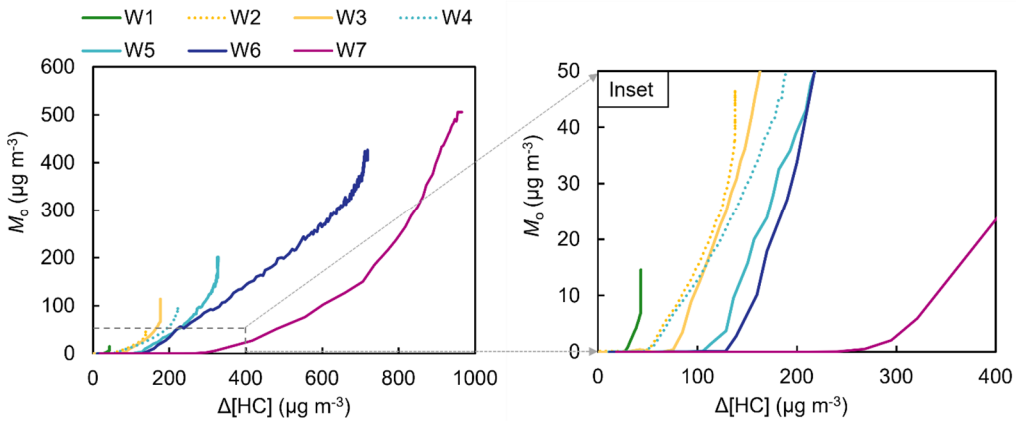

Figure 2-20 Measured SOA mass concentrations as a function of reacted camphene concentration with added NO_x; inset shows the lowest camphene concentrations from 0 – 400 µg m^{-3}.

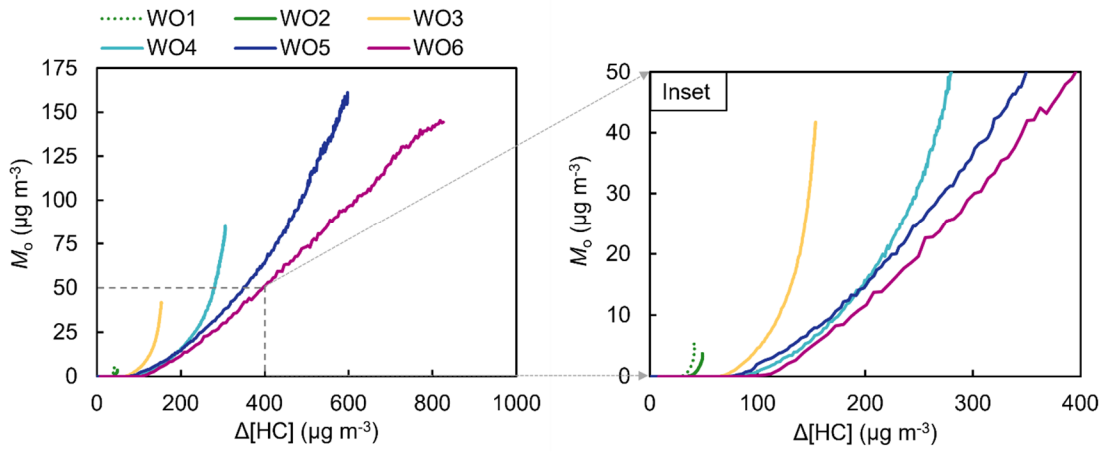

Figure 2-21 Measured SOA mass concentrations as a function of reacted camphene concentration without added NO_x; inset shows the lowest camphene concentrations from 0 – 400 µg m-3.

2.8 Reference

Afreh, I. K., Aumont, B., Camredon, M., and Barsanti, K. C.: Using GECKO-A to derive mechanistic understanding of SOA formation from the ubiquitous but understudied camphene, Atmos. Chem. Phys. Discuss., https://doi.org/10.5194/acp-2020-829, 2020.

Akagi, S. K., Yokelson, R. J., Burling, I. R., Meinardi, S., Simpson, I., Blake, D. R., McMeeking, G. R., Sullivan, A., Lee, T., Kreidenweis, S., Urbanski, S., Reardon, J., Griffith, D. W. T., Johnson, T. J., and Weise, D. R.: Measurements of reactive trace gases and variable O3 formation rates in some South Carolina biomass burning plumes, Atmos. Chem. Phys., https://doi.org/10.5194/acp-13-1141-2013, 2013.

Atkinson, R. and Arey, J.: Gas-phase tropospheric chemistry of biogenic volatile organic compounds: A review, Atmos. Environ., 37, 197–219, https://doi.org/10.1016/S1352-2310(03)00391-1, 2003.

Atkinson, R., Aschmann, S. M., and Arey, J.: Rate constants for the gas-phase reactions of OH and NO3 radicals and O3 with sabinene and camphene at 296±2 K, Atmos. Environ. Part A, Gen. Top., https://doi.org/10.1016/0960-1686(90)90144-C, 1990.

Aumont, B., Szopa, S., and Madronich, S.: Modelling the evolution of organic carbon during its gas-phase tropospheric oxidation: Development of an explicit model based on a self generating approach, Atmos. Chem. Phys., https://doi.org/10.5194/acp-5-2497-2005, 2005.

Aumont, B., Valorso, R., Mouchel-Vallon, C., Camredon, M., Lee-Taylor, J., and Madronich, S.: Modeling SOA formation from the oxidation of intermediate volatility n-alkanes, Atmos. Chem. Phys., 12, 7577–7589, https://doi.org/10.5194/acp-12-7577-2012, 2012.

Baruah, S. D., Gour, N. K., Sarma, P. J., and Deka, R. C.: OH-initiated mechanistic pathways and kinetics of camphene and fate of product radical: a DFT approach, Environ. Sci. Pollut. Res., https://doi.org/10.1007/s11356-017-0646-2, 2018.

Benelli, G., Govindarajan, M., Rajeswary, M., Vaseeharan, B., Alyahya, S. A., Alharbi, N. S., Kadaikunnan, S., Khaled, J. M., and Maggi, F.: Insecticidal activity of camphene, zerumbone and α-humulene from Cheilocostus speciosus rhizome essential oil against the Old-World bollworm, Helicoverpa armigera, Ecotoxicol. Environ. Saf., 148, 781–786, https://doi.org/10.1016/j.ecoenv.2017.11.044, 2018.

Bianchi, F., Kurtén, T., Riva, M., Mohr, C., Rissanen, M. P., Roldin, P., Berndt, T., Crounse, J. D., Wennberg, P. O., Mentel, T. F., Wildt, J., Junninen, H., Jokinen, T., Kulmala, M., Worsnop, D. R., Thornton, J. A., Donahue, N., Kjaergaard, H. G., and Ehn, M.: Highly Oxygenated Organic Molecules (HOM) from Gas-Phase Autoxidation Involving Peroxy Radicals: A Key Contributor to Atmospheric Aerosol, https://doi.org/10.1021/acs.chemrev.8b00395, 27 March 2019.

Camredon, M., Aumont, B., Lee-Taylor, J., and Madronich, S.: The SOA/VOC/NOx system: An explicit model of secondary organic aerosol formation, Atmos. Chem. Phys., https://doi.org/10.5194/acp-7-5599-2007, 2007.

Canagaratna, M. R., Jimenez, J. L., Kroll, J. H., Chen, Q., Kessler, S. H., Massoli, P., Hildebrandt Ruiz, L., Fortner, E., Williams, L. R., Wilson, K. R., Surratt, J. D., Donahue, N. M., Jayne, J. T., and Worsnop, D. R.: Elemental ratio measurements of organic compounds using aerosol mass spectrometry: Characterization, improved calibration, and implications, Atmos. Chem. Phys., 15, 253–272, https://doi.org/10.5194/acp-15-253-2015, 2015.

Carter, W. P. L.: A detailed mechanism for the gas-phase atmospheric reactions of organic compounds, Atmos. Environ. Part A, Gen. Top., 24, 481–518, https://doi.org/10.1016/0960-1686(90)90005-8, 1990.

Carter, W. P. L.: Development of ozone reactivity scales for volatile organic compounds, J. Air Waste Manag. Assoc., 44, 881–899, https://doi.org/10.1080/1073161x.1994.10467290, 1994.

Carter, W. P. L. Documentation of the SAPRC-99 Chemical Mechanism for VOC Reactivity Assessment, 1999; p 329.

Carter, W. P. L.: Documentation of the SAPRC-99 Chemical Mechanism for VOC Reactivity Assessment, Report to the California Air Resources Board. Available at http://cert.ucr.edu/~carter/absts.htm#saprc99 and http://www.cert.ucr.edu/~carter/reactdat.htm., 2000.

Carter, W. P. L. Development of the SAPRC-07 Chemical Mechanism and Updated Ozone Reactivity Scales; Final Report to the California Air Resources Board Contract No. 03-318, March 2009.

Carter, W. P. L.: Development of a condensed SAPRC-07 chemical mechanism, Atmos. Environ., 44, 5336–5345, https://doi.org/10.1016/j.atmosenv.2010.01.024, 2010a.

Carter, W. P. L.: Development of the SAPRC-07 Chemical Mechanism and Updated Ozone Reactivity Scales, 2010b.

Carter, W. P. L.: Documentation of the SAPRC-18 Mechanism; Report to California Air Resources Board Contract No. 11-761, May, 2020. [online] Available from: https://intra.engr.ucr.edu/~carter/SAPRC/18/, 2020a.

Carter, W. P. L.: Gateway to the SAPRC Mechanism Generation System: http://mechgen.cert.ucr.edu/, last access: 30 March 2021.

Carter, W. P. L.: Estimates and Assignments used in the SAPRC-18 Mechanism Generation System; Report to California Air Resources Board Contract No. 11-761. In preparation. When completed, will be available at http://intra.engr.ucr.edu/~carter/SAPRC/18, 2020b.

Carter, W. P. L. and Lurmann, F.W., 1990. Evaluation of the RADM gas-phase chemical mechanism. US Environmental Protection Agency, Atmospheric Research and Exposure Assessment Laboratory, Office of Research and Development.

Carter, W. P. L., Cocker, D. R., Fitz, D. R., Malkina, I. L., Bumiller, K., Sauer, C. G., Pisano, J. T., Bufalino, C., and Song, C.: A new environmental chamber for evaluation of gas-phase chemical mechanisms and secondary aerosol formation, Atmos. Environ., 39, 7768–7788, https://doi.org/10.1016/j.atmosenv.2005.08.040, 2005.

Clark, C. H., Kacarab, M., Nakao, S., Asa-Awuku, A., Sato, K., and Cocker, D. R.: Temperature Effects on Secondary Organic Aerosol (SOA) from the Dark Ozonolysis and Photo-Oxidation of Isoprene, Environ. Sci. Technol., 50, 5564–5571, https://doi.org/10.1021/acs.est.5b05524, 2016.

Cocker, D. R., Flagan, R. C., and Seinfeld, J. H.: State-of-the-art chamber facility for studying atmospheric aerosol chemistry, Environ. Sci. Technol., 35, 2594–2601, https://doi.org/10.1021/es0019169, 2001.

Crounse, J. D., Nielsen, L. B., Jørgensen, S., Kjaergaard, H. G., and Wennberg, P. O.: Autoxidation of Organic Compounds in the Atmosphere, J. Phys. Chem. Lett., 4, 3513–3520, https://doi.org/10.1021/JZ4019207, 2013.

DeCarlo, P. F., Kimmel, J. R., Trimborn, A., Northway, M. J., Jayne, J. T., Aiken, A. C., Gonin, M., Fuhrer, K., Horvath, T., Docherty, K. S., Worsnop, D. R., and Jimenez, J. L.: Field-deployable, high-resolution, time-of-flight aerosol mass spectrometer, Anal. Chem., 78, 8281–8289, https://doi.org/10.1021/ac061249n, 2006.

Donahue, N. M., Robinson, A. L., Stanier, C. O., and Pandis, S. N.: Coupled partitioning, dilution, and chemical aging of semivolatile organics, Environ. Sci. Technol., 40, 2635–2643, https://doi.org/10.1021/es052297c, 2006.

Donahue, N. M., Robinson, A. L., and Pandis, S. N.: Atmospheric organic particulate matter: From smoke to secondary organic aerosol, Atmos. Environ., 43, 94–106, https://doi.org/10.1016/j.atmosenv.2008.09.055, 2009.

Eddingsaas, N. C., Loza, C. L., Yee, L. D., Chan, M., Schilling, K. A., Chhabra, P. S., Seinfeld, J. H., and Wennberg, P. O.: α-pinene photooxidation under controlled chemical conditions-Part 2: SOA yield and composition in low-and high-NO x environments, Atmos. Chem. Phys., 12, 7413–7427, https://doi.org/10.5194/acp-12-7413-2012, 2012.

Ehn, M., Berndt, T., Wildt, J., and Mentel, T.: Highly Oxygenated Molecules from Atmospheric Autoxidation of Hydrocarbons: A Prominent Challenge for Chemical Kinetics Studies, Int. J. Chem. Kinet., 49, 821–831, https://doi.org/10.1002/KIN.21130, 2017.

Fry, J. L., Draper, D. C., Barsanti, K. C., Smith, J. N., Ortega, J., Winkler, P. M., Lawler, M. J., Brown, S. S., Edwards, P. M., Cohen, R. C., and Lee, L.: Secondary Organic Aerosol Formation and Organic Nitrate Yield from NO 3 Oxidation of Biogenic Hydrocarbons Terms of Use CC-BY, Environ. Sci. Technol, 48, https://doi.org/10.1021/es502204x, 2014.

Gaona-Colmán, E., Blanco, M. B., Barnes, I., Wiesen, P., and Teruel, M. A.: OH- and O3-initiated atmospheric degradation of camphene: temperature dependent rate coefficients, product yields and mechanisms, RSC Adv., 7, 2733–2744, https://doi.org/10.1039/c6ra26656h, 2017.

Geron, C., Rasmussen, R., Arnts, R. R., and Guenther, A.: A review and synthesis of monoterpene speciation from forests in the United States, Atmos. Environ., https://doi.org/10.1016/S1352-2310(99)00364-7, 2000.

Gilman, J. B., Lerner, B. M., Kuster, W. C., Goldan, P. D., Warneke, C., Veres, P. R., Roberts, J. M., De Gouw, J. A., Burling, I. R., and Yokelson, R. J.: Biomass burning emissions and potential air quality impacts of volatile organic compounds and other trace gases from fuels common in the US, Atmos. Chem. Phys., https://doi.org/10.5194/acp-15-13915-2015, 2015.

Griffin, R. J., Cocker, D. R., Flagan, R. C., and Seinfeld, J. H.: Organic aerosol formation from the oxidation of biogenic hydrocarbons, J. Geophys. Res. Atmos., https://doi.org/10.1029/1998JD100049, 1999.

Guenther, A.: A global model of natural volatile organic compound emissions, J. Geophys. Res., https://doi.org/10.1029/94JD02950, 1995.

Hakola, H., Arey, J., Aschmann, S. M., and Atkinson, R.: Product formation from the gas-phase reactions of OH radicals and O3 with a series of monoterpenes, J. Atmos. Chem., https://doi.org/10.1007/BF00694375, 1994.

Hatch, L. E., Luo, W., Pankow, J. F., Yokelson, R. J., Stockwell, C. E., and Barsanti, K. C.: Identification and quantification of gaseous organic compounds emitted from biomass burning using two-dimensional gas chromatography-time-of-flight mass spectrometry, Atmos. Chem. Phys., https://doi.org/10.5194/acp-15-1865-2015, 2015.

Hatch, L. E., Jen, C. N., Kreisberg, N. M., Selimovic, V., Yokelson, R. J., Stamatis, C., York, R. A., Foster, D., Stephens, S. L., Goldstein, A. H., and Barsanti, K. C.: Highly Speciated Measurements of Terpenoids Emitted from Laboratory and Mixed-Conifer Forest Prescribed Fires, Environ. Sci. Technol., https://doi.org/10.1021/acs.est.9b02612, 2019.

Hatfield, M. L. and Huff Hartz, K. E.: Secondary organic aerosol from biogenic volatile organic compound mixtures, Atmos. Environ., 45, 2211–2219, https://doi.org/10.1016/j.atmosenv.2011.01.065, 2011.

Hayward, S., Muncey, R. J., James, A. E., Halsall, C. J., and Hewitt, C. N.: Monoterpene emissions from soil in a Sitka spruce forest, Atmos. Environ., https://doi.org/10.1016/S1352-2310(01)00213-8, 2001.

Henze, D. K., Seinfeld, J. H., Ng, N. L., Kroll, J. H., Fu, T. M., Jacob, D. J., and Heald, C. L.: Global modeling of secondary organic aerosol formation from aromatic hydrocarbons: High- vs. low-yield pathways, Atmos. Chem. Phys., 8, 2405–2421, https://doi.org/10.5194/acp-8-2405-2008, 2008.

Hurley, M. D., Sokolov, O., and Wallington, T. J.: Organic aerosol formation during the atmospheric degradation of toluene, Environ. Sci. Technol., 35, 1358–1366, https://doi.org/10.1021/es0013733, 2001.

Jay R. Odum, Thorsten Hoffmann, Frank Bowman, Don Collins, Richard C. Flagan, and John H. Seinfeld: Gas/Particle Partitioning and Secondary Organic Aerosol Yields, 2580–2585 pp., https://doi.org/10.1021/ES950943, 1996.

Jiang, J., Carter, W. P. L., Cocker, D. R., and Barsanti, K. C.: Development and Evaluation of a Detailed Mechanism for Gas-Phase Atmospheric Reactions of Furans, ACS Earth Sp. Chem., 4, 1254–1268, https://doi.org/10.1021/acsearthspacechem.0c00058, 2020a.

Jiang, J., Carter, W. P. L., Cocker, D. R., and Barsanti, K. C.: Development and Evaluation of a Detailed Mechanism for Gas-Phase Atmospheric Reactions of Furans, ACS Earth Sp. Chem., 4, 1254–1268, https://doi.org/10.1021/acsearthspacechem.0c00058, 2020b.

Jokinen, T., Sipilä, M., Richters, S., Kerminen, V.-M., Paasonen, P., Stratmann, F., Worsnop, D., Kulmala, M., Ehn, M., Herrmann, H., and Berndt, T.: Rapid Autoxidation Forms Highly Oxidized RO2 Radicals in the Atmosphere, Angew. Chemie Int. Ed., 53, 14596–14600, https://doi.org/10.1002/ANIE.201408566, 2014.

Komenda, M.: Monoterpene emissions from Scots pine (*Pinus sylvestris*): Field studies of emission rate variabilities, J. Geophys. Res., 107, 4161, https://doi.org/10.1029/2001JD000691, 2002.

Krechmer, J. E., Day, D. A., and Jimenez, J. L.: Always Lost but Never Forgotten: Gas-Phase Wall Losses Are Important in All Teflon Environmental Chambers, Environ. Sci. Technol., 54, 12890–12897, https://doi.org/10.1021/ACS.EST.0C03381/SUPPL_FILE/ES0C03381_SI_001.PDF, 2020.

Kroll, J. H. and Seinfeld, J. H.: Chemistry of secondary organic aerosol: Formation and evolution of low-volatility organics in the atmosphere, https://doi.org/10.1016/j.atmosenv.2008.01.003, 1 May 2008.

Kroll, J. H., Ng, N. L., Murphy, S. M., Flagan, R. C., and Seinfeld, J. H.: Secondary organic aerosol formation from isoprene photooxidation, Environ. Sci. Technol., 40, 1869–1877, https://doi.org/10.1021/es0524301, 2006.

Kuwata, M., Zorn, S. R., and Martin, S. T.: Using elemental ratios to predict the density of organic material composed of carbon, hydrogen, and oxygen, Environ. Sci. Technol., 46, 787–794, https://doi.org/10.1021/es202525q, 2012.

La, Y. S., Camredon, M., Ziemann, P. J., Valorso, R., Matsunaga, A., Lannuque, V., Lee-Taylor, J., Hodzic, A., Madronich, S., and Aumont, B.: Impact of chamber wall loss of gaseous organic compounds on secondary organic aerosol formation: Explicit modeling of SOA formation from alkane and alkene oxidation, Atmos. Chem. Phys., 16, 1417–1431, https://doi.org/10.5194/ACP-16-1417-2016, 2016.

Lannuque, V., Camredon, M., Couvidat, F., Hodzic, A., Valorso, R., Madronich, S., Bessagnet, B., and Aumont, B.: Exploration of the influence of environmental conditions on secondary organic aerosol formation and organic species properties using explicit simulations: Development of the VBS-GECKO parameterization, Atmos. Chem. Phys., 18, 13411–13428, https://doi.org/10.5194/acp-18-13411-2018, 2018.

Li, L., Tang, P., and Cocker, D. R.: Instantaneous nitric oxide effect on secondary organic aerosol formation from m-xylene photooxidation, Atmos. Environ., 119, 144–155, https://doi.org/10.1016/j.atmosenv.2015.08.010, 2015.
Li, L., Tang, P., Nakao, S., and Cocker, D. R.: Impact of molecular structure on secondary organic aerosol formation from aromatic hydrocarbon photooxidation under low-NOx conditions, Atmos. Chem. Phys., 16, 10793–10808, https://doi.org/10.5194/ACP-16-10793-2016, 2016.
Li, Q., Hu, D., Leungsakul, S., and Kamens, R. M.: Large outdoor chamber experiments and computer simulations: (I) Secondary organic aerosol formation from the oxidation of a mixture of d-limonene and α-pinene, Atmos. Environ., 41, 9341–9352, https://doi.org/10.1016/j.atmosenv.2007.09.017, 2007.
Ludley, K. E., Jickells, S. M., Chamberlain, P. M., Whitaker, J., and Robinson, C. H.: Distribution of monoterpenes between organic resources in upper soil horizons under monocultures of Picea abies, Picea sitchensis and Pinus sylvestris, Soil Biol. Biochem., https://doi.org/10.1016/j.soilbio.2009.02.002, 2009.
Maleknia, S. D., Bell, T. L., and Adams, M. A.: PTR-MS analysis of reference and plant-emitted volatile organic compounds, Int. J. Mass Spectrom., https://doi.org/10.1016/j.ijms.2006.11.010, 2007.
Malloy, Q. G. J., Nakao, S., Qi, L., Austin, R., Stothers, C., Hagino, H., and Cocker, D. R.: Real-Time aerosol density determination utilizing a modified scanning mobility particle sizer aerosol particle mass analyzer system, Aerosol Sci. Technol., 43, 673–678, https://doi.org/10.1080/02786820902832960, 2009.
Mazza, G. and Cottrell, T.: Volatile components of roots, stems, leaves, and flowers of Echinacea species, J. Agric. Food Chem., https://doi.org/10.1021/jf981117y, 1999.
McVay, R. C., Zhang, X., Aumont, B., Valorso, R., Camredon, M., La, Y. S., Wennberg, P. O., and Seinfeld, J. H.: SOA formation from the photooxidation of α-pinene: Systematic exploration of the simulation of chamber data, Atmos. Chem. Phys., 16, 2785–2802, https://doi.org/10.5194/acp-16-2785-2016, 2016.
Mehra, A., Krechmer, J. E., Lambe, A., Sarkar, C., Williams, L., Khalaj, F., Guenther, A., Jayne, J., Coe, H., Worsnop, D., Faiola, C., and Canagaratna, M.: Oligomer and highly oxygenated organic molecule formation from oxidation of oxygenated monoterpenes emitted by California sage plants, Atmos. Chem. Phys., 20, 10953–10965, https://doi.org/10.5194/acp-20-10953-2020, 2020.
Moukhtar, S., Couret, C., Rouil, L., and Simon, V.: Biogenic Volatile Organic Compounds (BVOCs) emissions from Abies alba in a French forest, Sci. Total Environ., 354, 232–245, https://doi.org/10.1016/j.scitotenv.2005.01.044, 2006.
Mutzel, A., Rodigast, M., Iinuma, Y., Böge, O., and Herrmann, H.: Monoterpene SOA - Contribution of first-generation oxidation products to formation and chemical composition, Atmos. Environ., 130, 136–144, https://doi.org/10.1016/j.atmosenv.2015.10.080, 2016.
Nakao, S., Tang, P., Tang, X., Clark, C. H., Qi, L., Seo, E., Asa-Awuku, A., and Cocker, D.: Density and elemental ratios of secondary organic aerosol: Application of a density prediction method, Atmos. Environ., 68, 273–277, https://doi.org/10.1016/j.atmosenv.2012.11.006, 2013.

Nannoolal, Y., Rarey, J., and Ramjugernath, D.: Estimation of pure component properties part 3. Estimation of the vapor pressure of non-electrolyte organic compounds via group contribution and group interactions, Fluid Phase Equilib., 269, 117–133, https://doi.org/10.1016/j.fluid.2008.04.020, 2008.

Ng, N. L., Chhabra, P. S., Chan, A. W. H., Surratt, J. D., Kroll, J. H., Kwan, A. J., McCabe, D. C., Wennberg, P. O., Sorooshian, A., Murphy, S. M., Dalleska, N. F., Flagan, R. C., and Seinfeld, J. H.: Effect of NOx level on secondary organic aerosol (SOA) formation from the photooxidation of terpenes, Atmos. Chem. Phys., 7, 5159–5174, https://doi.org/10.5194/acp-7-5159-2007, 2007a.

Ng, N. L., Chhabra, P. S., Chan, A. W. H., Surratt, J. D., Kroll, J. H., Kwan, A. J., McCabe, D. C., Wennberg, P. O., Sorooshian, A., Murphy, S. M., Dalleska, N. F., Flagan, R. C., and Seinfeld, J. H.: Effect of NOx level on secondary organic aerosol (SOA) formation from the photooxidation of terpenes, Atmos. Chem. Phys., https://doi.org/10.5194/acp-7-5159-2007, 2007b.

Ng, N. L., Kroll, J. H., Keywood, M. D., Bahreini, R., Varutbangkul, V., Flagan, R. C., Seinfeld, J. H., Lee, A., and Goldstein, A. H.: Contribution of first- versus second-generation products to secondary organic aerosols formed in the oxidation of biogenic hydrocarbons, Environ. Sci. Technol., 40, 2283–2297, https://doi.org/10.1021/ES052269U/SUPPL_FILE/ES052269USI20060124_070140.PDF, 2006.

Nøjgaard, J. K., Bilde, M., Stenby, C., Nielsen, O. J., and Wolkoff, P.: The effect of nitrogen dioxide on particle formation during ozonolysis of two abundant monoterpenes indoors, Atmos. Environ., 40, 1030–1042, https://doi.org/10.1016/j.atmosenv.2005.11.029, 2006.

Pankow, J. F.: An absorption model of the gas/aerosol partitioning involved in the formation of secondary organic aerosol, Atmos. Environ., 41, 75–79, https://doi.org/10.1016/j.atmosenv.2007.10.060, 1994.

Presto, A. A., Huff Hartz, K. E., and Donahue, N. M.: Secondary organic aerosol production from terpene ozonolysis. 2. Effect of NOx concentration, Environ. Sci. Technol., 39, 7046–7054, https://doi.org/10.1021/es050400s, 2005.

Pullinen, I., Schmitt, S., Kang, S., Sarrafzadeh, M., Schlag, P., Andres, S., Kleist, E., Mentel, T. F., Rohrer, F., Springer, M., Tillmann, R., Wildt, J., Wu, C., Zhao, D., Wahner, A., and Kiendler-Scharr, A.: Impact of NOx on secondary organic aerosol (SOA) formation from α-pinene and β-pinene photooxidation: The role of highly oxygenated organic nitrates, Atmos. Chem. Phys., 20, 10125–10147, https://doi.org/10.5194/acp-20-10125-2020, 2020.

Pye, H. O. T., Chan, A. W. H., Barkley, M. P., and Seinfeld, J. H.: Global modeling of organic aerosol: The importance of reactive nitrogen (NOx and NO3), Atmos. Chem. Phys., 10, 11261–11276, https://doi.org/10.5194/ACP-10-11261-2010, 2010.

Pye, H. O. T., D'Ambro, E. L., Lee, B. H., Schobesberger, S., Takeuchi, M., Zhao, Y., Lopez-Hilfiker, F., Liu, J., Shilling, J. E., Xing, J., Mathur, R., Middlebrook, A. M., Liao, J., Welti, A., Graus, M., Warneke, C., de Gouw, J. A., Holloway, J. S., Ryerson, T. B., Pollack, I. B., and Thornton, J. A.: Anthropogenic enhancements to production of highly

oxygenated molecules from autoxidation, Proc. Natl. Acad. Sci. U. S. A., 116, 6641–6646, https://doi.org/10.1073/pnas.1810774116, 2019.

Quéléver, L. L. J., Kristensen, K., Jensen, L. N., Rosati, B., Teiwes, R., Daellenbach, K. R., Peräkylä, O., Roldin, P., Bossi, R., Pedersen, H. B., Glasius, M., Bilde, M., and Ehn, M.: Effect of temperature on the formation of highly oxygenated organic molecules (HOMs) from alpha-pinene ozonolysis, Atmos. Chem. Phys., 19, 7609–7625, https://doi.org/10.5194/ACP-19-7609-2019, 2019.

Sarrafzadeh, M., Wildt, J., Pullinen, I., Springer, M., Kleist, E., Tillmann, R., Schmitt, S. H., Wu, C., Mentel, T. F., Zhao, D., Hastie, D. R., and Kiendler-Scharr, A.: Impact of NOx and OH on secondary organic aerosol formation from β-pinene photooxidation, Atmos. Chem. Phys., 16, 11237–11248, https://doi.org/10.5194/acp-16-11237-2016, 2016.

Schervish, M. and Donahue, N. M.: Peroxy radical chemistry and the volatility basis set, Atmos. Chem. Phys., 20, 1183–1199, https://doi.org/10.5194/acp-20-1183-2020, 2020.

Schwantes, R. H., Charan, S. M., Bates, K. H., Huang, Y., Nguyen, T. B., Mai, H., Kong, W., Flagan, R. C., and Seinfeld, J. H.: Low-volatility compounds contribute significantly to isoprene secondary organic aerosol (SOA) under high-NOx conditions, Atmos. Chem. Phys., 19, 7255–7278, https://doi.org/10.5194/ACP-19-7255-2019, 2019.

Song, C., Na, K., and Cocker, D. R.: Impact of the hydrocarbon to NOx ratio on secondary organic aerosol formation, Environ. Sci. Technol., https://doi.org/10.1021/es0493244, 2005.

White, M. L., Russo, R. S., Zhou, Y., Mao, H., Varner, R. K., Ambrose, J., Veres, P., Wingenter, O. W., Haase, K., Stutz, J., Talbot, R., and Sive, B. C.: Volatile organic compounds in northern New England marine and continental environments during the ICARTT 2004 campaign, J. Geophys. Res. Atmos., https://doi.org/10.1029/2007JD009161, 2008.

Xavier, C., Rusanen, A., Zhou, P., Dean, C., Pichelstorfer, L., Roldin, P., and Boy, M.: Aerosol mass yields of selected biogenic volatile organic compounds - A theoretical study with nearly explicit gas-phase chemistry, Atmos. Chem. Phys., 19, 13741–13758, https://doi.org/10.5194/ACP-19-13741-2019, 2019.

Ye, P., Ding, X., Hakala, J., Hofbauer, V., Robinson, E. S., and Donahue, N. M.: Vapor wall loss of semi-volatile organic compounds in a Teflon chamber, 50, 822–834, https://doi.org/10.1080/02786826.2016.1195905, 2016.

Ye, Q., Wang, M., Hofbauer, V., Stolzenburg, D., Chen, D., Schervish, M., Vogel, A., Mauldin, R.L., Baalbaki, R., Brilke, S., and Dada, L.: Molecular Composition and Volatility of Nucleated Particles from α-Pinene Oxidation between -50 °C and +25 °C, Environ. Sci. Technol., 53, 12357–12365, https://doi.org/10.1021/ACS.EST.9B03265, 2019.

Zhang, S.-H., Shaw, M., Seinfeld, J. H., and Flagan, R. C.: Photochemical Aerosol Formation From c-Pinene-and 13-Pinene, JOURNAL OF GEOPHYSICAL RESEARCH, 717–737 pp., 1992.

Zhang, X., Cappa, C. D., Jathar, S. H., McVay, R. C., Ensberg, J. J., Kleeman, M. J., and Seinfeld, J. H.: Influence of vapor wall loss in laboratory chambers on yields of

secondary organic aerosol, Proc. Natl. Acad. Sci., 111, 5802–5807, https://doi.org/10.1073/PNAS.1404727111, 2014.
Zhang, X., Lambe, A. T., Upshur, M. A., Brooks, W. A., Bé, A. G., Thomson, R. J., Geiger, F. M., Surratt, J. D., Zhang, Z., Gold, A., Graf, S., Cubison, M. J., Groessl, M., Jayne, J. T., Worsnop, D. R., and Canagaratna, M. R.: Highly Oxygenated Multifunctional Compounds in α-Pinene Secondary Organic Aerosol, Environ. Sci. Technol., 51, 5932–5940, https://doi.org/10.1021/ACS.EST.6B06588, 2017.
Zhang, X., Schwantes, R. H., McVay, R. C., Lignell, H., Coggon, M. M., Flagan, R. C., and Seinfeld, J. H.: Vapor wall deposition in Teflon chambers, Atmos. Chem. Phys., 15, 4197–4214, https://doi.org/10.5194/ACP-15-4197-2015, 2015.
Zhao, Y., Thornton, J. A., and Pye, H. O. T.: Quantitative constraints on autoxidation and dimer formation from direct probing of monoterpene-derived peroxy radical chemistry, Proc. Natl. Acad. Sci. U. S. A., 115, 12142–12147, https://doi.org/10.1073/pnas.1812147115, 2018.
Ziemann, P. J. and Atkinson, R.: Kinetics, products, and mechanisms of secondary organic aerosol formation, Chem. Soc. Rev., 41, 6582–6605, https://doi.org/10.1039/c2cs35122f, 2012.

Chapter 3 : Chamber Optimization and SOA Formation Characterization of Volatile Consumer Products (VCPs) Related Compounds

3.1 Introduction

Environmental chamber has been serving as one of the most important sources for advancing our understanding on secondary organic aerosol (SOA) formation from oxidation of volatile organic compounds (VOCs) for over 30 years (Odum et al., 1997). The indoor environmental chambers provide important insights for atmospheric reaction mechanisms. In years of development, environmental chambers were designed, built, and upgraded for different targets and/or achieving different functionality, such as maximum incremental reactivity (MIR) study, engine emission study, humidity effects (Carter et al., 1995; Jahn et al., 2021; Nakao et al., 2011), etc. Various purposes require different experimental protocols, including operation procedures and data analysis methods that potentially introduce bias between systems, which can lead to a low consistency between results from different chamber systems or even within the same one. Since volatile consumer products (VCPs) has become the next important source for VOC emission after car emissions regulations getting strict year by year (McDonald et al., 2018), study on LVP-VOC, which is a typical VOC category in VCPs and is highly under-studied, is becoming urgent for the modeling updates. The LVP-VOC, due to the low vapor pressure feature, is extremely hard to be worked with and challenging the traditional experimental protocols on regular VOCs, which typically has a relatively high vapor pressure and are easy to be injected with little loss to walls when flow through tubing. The low vapor pressure not only caused a potential longer delay in VOC tubing transport, but also made the compound significantly hard to be calibrated on GC using “pillow” bags due to the limited size of the

bag and high demanding of total volume of carrier gas for fully evaporation of the LVP-VOC.

The different correction method for particle-wall and vapor-wall interactions used in different groups can be developed based on each group's own dataset, as a result, of which the assumptions underneath may be under evaluated on their effects on particle/vapor wall loss. Although the particle charge effects on particle wall interaction were determined to be negligible in Caltech 19m^3 chamber (Charan et al., 2018), this doesn't necessarily suggest particle charge has no potential effects on accelerating particle wall deposition. In fact, the observation of negligible effects of particle charge can be explained by the chamber wall being electric "neutral". "Neutral" here refers to the absolute value of surface voltage of the bag being low rather than the total charge being low because Teflon rubbing itself can also cause high absolute surface voltage but the net ±charge is "0" since no outer electrons are introduced to the Teflon material in this case. Without sufficient surface charge on the chamber wall, the encouraging effects of charge on particles wall loss could not be achieved. In the new UCR fixed-volume chamber, there is no measurable difference observed in particle wall loss between the experiments done with soft X ray off during experiment and X ray on through the experiments. The latter condition was expected to force a relatively "neutral" status of the particles. This is also consistent with the dramatic difference in particle number decay rate between the charged and discharged UCR chamber, which is discussed in this thesis. In addition, this could also form an explanation for not seeing statistical difference in organic compound loss rate between 4m^3 and 60m^3 chambers in study by Toro et al. (1985), in which the electrostatic might have strongly

accelerated the process of molecules travel and interaction with wall. Those observation further suggested that electric static surface charge on the Teflon chamber wall is so far the most critical factor in determining particle wall loss to the best of our knowledge but is often under-evaluated and ignored due to un-rigorous assumptions of "neutral" bags. Furthermore, the significant loss of particle or vapor molecules driven by surface static charge on the chamber may cause varying bias of the SOA formation and confuse the investigation of vapor wall loss effects across different chambers. This could be a possible reason for mismatching data between chamber and modeling results of vapor wall loss effects in addition to the varying vapor wall loss fraction potential of different compounds due to products volatility distribution proposed by modeling works (Krechmer et al., 2020; La et al., 2016). Here, I present an updated particle wall loss correction method for data analysis of experiments done in "neutral" chambers and our up-to-date observation of vapor wall loss with a serious of seeded m-xylene oxidation experiments.

In our recent study, a great discrepancy of up to 100% was observed in SOA yields from benzyl alcohol oxidation experiments done under the same targeted conditions between the Caltech chamber and UCR chamber. This was not expected due to the history of chamber developing that both chambers share many assumptions and design ideas, suggesting that unknown factors were existing that can dramatically affect the oxidation results. A detailed comparison was conducted between the two chambers to advance our understanding of effects from different factors (such as chamber size, light intensity, injection method, etc.) using oxidation of benzyl alcohol as a case study. It is noted that due to the complex of environmental chamber systems, the existing of some unevaluated factors (such as the little

difference in clean air composition at different locations) that may affect the chamber results within a limited degree is acceptable and are not discussed further in this thesis.

3.2 Standardization and Optimization of Environmental Chamber

3.2.1 Chamber comparison

A comprehensive comparison was conducted among three chambers: the UCR dual collapsible chamber, the new UCR fix-volume chamber, and the Caltech dual chamber. Comparison terms can be classified into two categories: the basic information of chamber setup and the key differences that are experimental protocol related. Instruments inventory of both groups shares much similarity thus they are not included in the current form. Table 3-1 represents the most up-to-date chamber setting after necessary modifications. A series of experiments were conducted under such chamber setting, which also forms the protocol for future VCP related chamber study.

Table 3-1 Summary of chamber comparison between the UCR chambers and Caltech chamber.

Terms	UCR collapsible chamber	UCR new fixed-volume chamber	Caltech dual chamber
Size	~90m^3 × 2	~118m^3	~19m^3 × 2
Dimensions	Collapsible ~ 6m(H) × ~3m(W) × ~5m(D)	~ 4.6m(H) × ~4.9m(W) × ~5.3m(D)	~2.7m(H) × ~2.7m(W) × ~2.4m(D)
Surface area to volume ratio	Start at 1.43 m^{-1} , gradually increase to 2.68 m^{-1}	~1.22 m^{-1}	~2.2 m^{-1}
Material	FEP Teflon	FEP Teflon	FEP Teflon
Temperature	~5- 40°C ±1°C	~5- 40°C ±1°C	~10- 45°C ±1°C
Relative humidity	0-100%	0-100%	0-100%
Clean air source	Compressed air purified by canisters of Purafil, heated Carulite 300, and particle filter pack	Compressed air purified by canisters of Purafil, heated Carulite 300, and particle filter pack	Compressed ambient air filtered to remove particulate, water vapor (silica gel), NO_x (Purafil), and small carbon compounds (activated carbon and molecular sieve).
Shortest distance from chamber to light	~16 ft	~14.3 ft	~1 ft

[1]Enclosure purge air	Up to 1,600 SCFH	Up to 1,000 SCFH	N/A
Pressure differential (inside minus outside)	>0.01 inH_2O	0.008-0.012 inH_2O during cleaning; dilution correction according to tracer level	~0 pressure differential
Black lights	Sylvania BL350 115 W	Sylvania BL350 115 W	Sylvania BL350 40 W
Light intensity	$k_{NO2\rightarrow NO}$=0.402 min^{-1}	$k_{NO2\rightarrow NO}$=0.402 min^{-1}	$k_{NO2\rightarrow NO}$=0.372 min^{-1}
UV peak wavelength	350nm(main), 435nm, 545nm, 577nm	350nm(main), 435nm, 545nm, 577nm	350nm(main), 435nm, 545nm, 577nm
VOC injection	Weighted regular VOC is injected to glass tubing with heated clean air flow at 50°C, 10 LPM for 15mins; tubing to chamber is heated and black-out. Weighted LVP-VOC is injected onto glass wool(hydrophilic or hydrophobic depends on VOC solubility) tube held in a 50-60°C oven and being flushed with 10 LPM 50-60°C clean air for up to	Weighted regular VOC is injected to glass tubing with heated clean air flow at 50°C, 10 LPM for 15mins; tubing to chamber is heated and black-out. Weighted LVP-VOC is injected onto glass wool(hydrophilic or hydrophobic depends on VOC solubility) tube held in a 50-60°C oven and being flushed with 10 LPM 50-60°C clean air for up to	A measured volume of L/VOC is placed on an enclosed **Teflon filter**. Warmed N_2 (60 °C) is blown over the filter into the chamber. A measured volume of L/VOC is placed in an **enclosed reservoir**. Warmed air (60 °C) is blown

	30mins; ~100% injection efficiency.	30mins; ~100% injection efficiency.	over the reservoir and through glass wool. A measured volume of L/VOC is placed in a vial of **glass wool**. N_2 is blown over the glass wool into the chamber. Typically, injections are done at 5 LPM. Injection times vary.
Chamber surface charge	Charged due to Teflon film rubbing with reflective aluminum sheet; average surface voltage is unknown	"Neutral"; Teflon reactor is isolated from the aluminum wall/ground with Teflon mat underneath each frame feet; Soft X-ray PhotoIonizers were on before/through the experiments to discharge bag to "neutral"; surface voltage around ±10V	"Neutral"; Chamber access is strictly restricted to avoid charge being introduced onto the bag; the bag is hung to suspend in the air and isolated; surface voltage around ±10V
VOC concentration determination	GC-FID	GC-FID	GC-FID, FT-IR, CIMS

Sampling line to GC	Not heated, no particle filter to avoid gas phase sorption losses	Not heated, no particle filter to avoid gas phase sorption losses	Not heated; with particle filter, GC is retrofitted to have all Teflon-plumbing (no metal to avoid reacting our sample)
SOA background	<0.1 $\mu m^3/cm^3$ (tested at 1ppm H_2O_2)	<0.01 $\mu m^3/cm^3$ (tested at 2ppm H_2O_2)	To be characterized

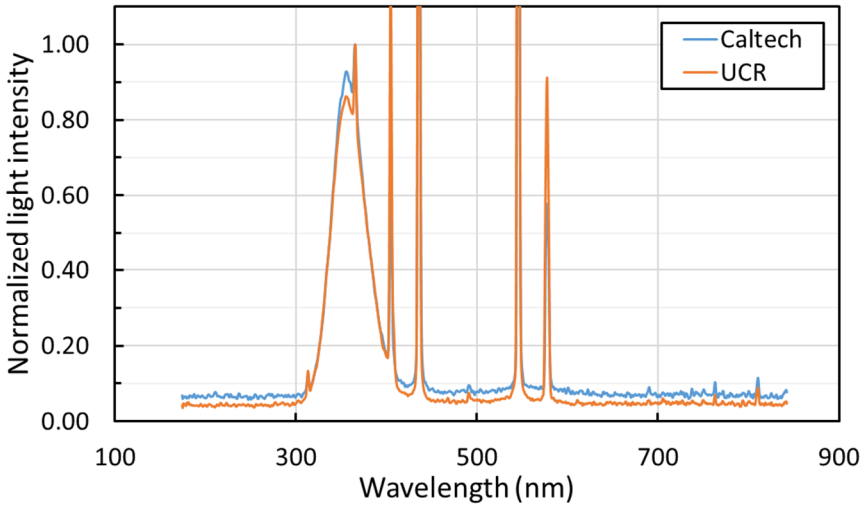

Figure 3-1 UV light wavelength comparison of Caltech and UCR chambers as measured in winter 2022.

In addition to the compared terms included in Table 3-1, one of the most unique features that distinguished the new UCR fixed-volume chamber from traditional chambers is the application of three Hamamatsu soft X-ray PhotoIonizers that were tested to be able to fully cover the whole 118m^3 Teflon bag and discharge the bag from over ±10000V to within ±10V in 2 minutes. The PhotoIonizers are located at ceiling above the bag and two sides of the bag, respectively (Figure 3-2). PhotoIonizers were tested to be able to discharge both sides of the Teflon film almost simultaneously from a distance of 5.25ft. The neutrality of the bag is always remembered by easy to be broken unconsciously. FEP film that statically sit overnight shows around ±30-100V at places that touch aluminum sheet, over ±200V at where FEP film touches FEP film, and over ±10,000 V after being slightly rubbed by bare hand. Rubbing FEP with aluminum sheet gently can charge the film to ±3000 V. The data was measured by Ultra Stable Surface Volt Meter, Model USSVM II, ALPHALAB INC.

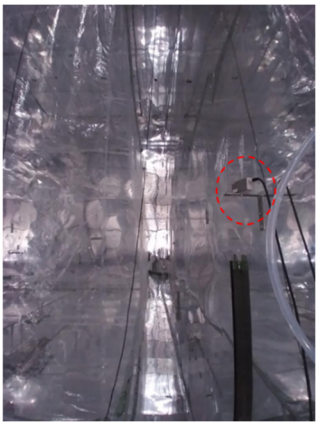

Figure 3-2 Right alleyway with Soft X-ray PhotoIonizer (red circle) mounted on the wall. Chamber bag is located at the left side in the figure.

According to the equation of SOA mass yield calculation,

$$\text{SOA mass yield} = \frac{\text{SOA mass formation}}{\text{Hydrocarbon reacted mass}},$$

two datasets are of critical importance to generate an accurate SOA mass yield: the data from SMPS with density estimated from APM and data from GC or other instruments for reacted VOC. The importance of determining the correct reacted amount of parent hydrocarbon was reflected in the benzyl alcohol case study, which is shown in section 3.3.

3.2.1.1 Particle number and volume concentration

The SMPS of Caltech chamber was brought to the UCR chamber and connected in parallel with the UCR dual-SMPS to sample from the same particle source. The data comparison shows great consistence between two instruments.

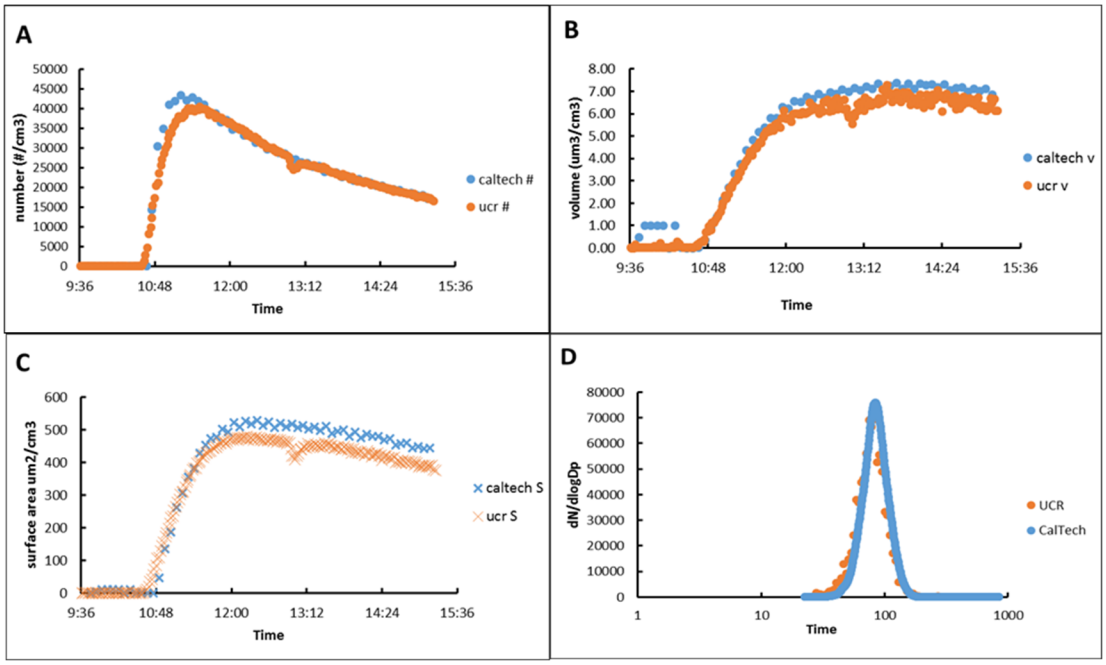

Figure 3-3 Comparison of SMPS performance. (A) number concentration; (B) volume concentration; (C) surface area concentration; (D) particle size distribution at the same moment

The particle density is one of the most important parameters that can easily affect the SOA mass calculation but have been under evaluated in many reports by assuming one single approximate number for all experiments. Based on the previous oxidation experiments results in the UCR chamber, the density of particles formed from oxidation of m-xylene varied from +1% to +10% compared to 1.40 g cm^{-3}(a typical density for secondary organic aerosol) under different experimental conditions; density for oxidation of camphene varied from –7.1% to +5% compared to 1.40 g cm^{-3} under different experimental conditions (chapter 2). As a result, the SOA mass yields reported with one applying a single density value of 1.40 g cm^{-3} to all experiments can have a notable uncertainty (e.g., up to 10% in the m-xylene case), which can be even higher when SOA mass yield data is compared across studies done in different groups.

3.2.1.2 Initial VOC mixing ratio determination

The value of reacted VOC concentration is one of the most critical parameters that may easily affect the value of SOA mass yield, especially in LVP-VOC related studies due to the difficulty in operating compounds with such low volatility.

UCR and Caltech use slightly different GC calibration methods: both UCR and Caltech typically use Teflon pillow bag to get the response factor of a VOC. The UCR group uses either a 120L pillow bag or a large 30m^3 Teflon chamber depending on the vapor pressure of the LVP-VOC. Caltech group uses a 140L Teflon pillow bag with GC and fourier transform infrared absorption (FT-IR) spectroscopy with absorption cross sections from the Pacific Northwest National Laboratory (PNNL) database. In addition, Caltech also uses a CIMS as an alternate to determine the VOC concentration.

3.2.2 Wall loss correction

3.2.2.1 Particle wall loss

The particle number decay rate (β) is used to describe the particle wall loss rate and is defined as

$$\frac{dN(D_p,t)}{dt} = -\beta(D_p)N(D_p,t),$$

where $N(D_p, t)$ is the particle number concentration of particles with diameter D_p at time t. A series of repeated α-pinene ozonolysis experiments were conducted under varying charging status of the UCR old collapsible chamber. Chamber was pre-charged by being rubbed against nitrile gloves in some of the tests. The application of soft X-ray over the

chamber effectively reduced the particle number decay (Table 3-2) to 4.5-4.61 day^{-1} compared to 5.46-6.13 day^{-1} when chamber was pre-charged and no soft X-ray was applied. The smallest decay rate was observed in experiment 2612, in which neither chamber pre-charging nor soft X-ray was applied. This is likely because this specific run followed a different set of reactions that did not have a secondary nucleation burst, which happened in all of the other runs that caused double particle size distribution peaks at the end of the experiments. Note that the data shown in Table 3-2 was not corrected for coagulation.

Table 3-2 Particles number decay rate distribution over different chamber charging status by repeated α-pinene ozonolysis test in the old UCR collapsible chamber starting with ~80ppb α-pinene and ~250ppb O_3.

Run ID	Oxidation duration (min)	Pre-charged	Soft X-ray on throughout	Fitted decay rate of total number (day^{-1})
2612	281	No	No	3.41
2613	316	Yes	No	6.13
2614	340	No	Yes	4.5
2615	346	Yes	Yes	4.61
2616	277	Yes	No	5.46

The particle total-number decay rate in the new UCR fixed volume chamber without coagulation correction was also evaluated in a purpose to compare to the UCR old chamber. By isolating the bag from enclosure walls and ground and eliminating the chamber moving elevator system, the total-number decay rate in the new UCR chamber became less than 2 day^{-1} without coagulation correction.

The estimation of the size dependent particle decay rate was done by poly-dispersed seed (ammonia sulfate) deposition tests in the UCR old chamber and monodispersed seed test

in the new fixed-volume chamber (Figure 3-3) (Le and Li, et al., 2022). The particle decay rate of the Caltech chamber (Figure 3-3) is derived from coagulation corrected poly-dispersed seed (ammonia sulfate) test (Charan et al., 2018).

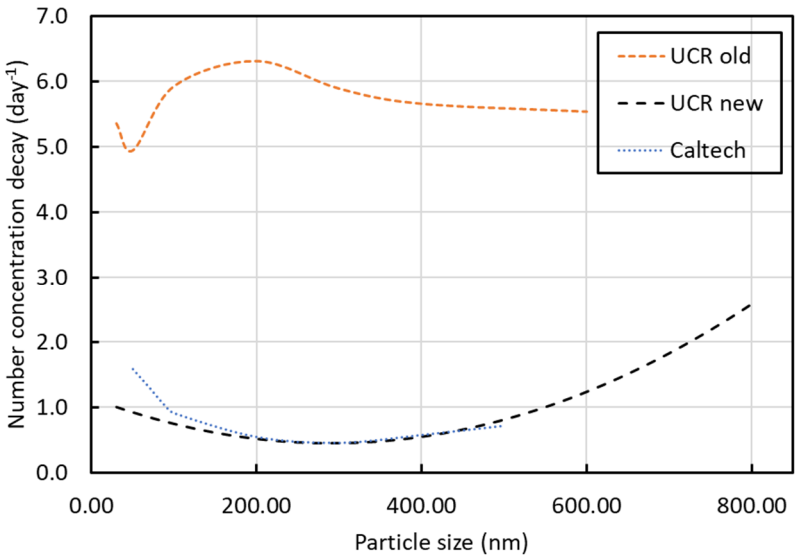

Figure 3-4 Particle number concentration decay rate of UCR old collapsible chamber, UCR new fixed-volume chamber and Caltech chamber. Note the data are coagulation corrected except for UCR old chamber data. (Le and Li, et al., 2022).

Shown in Figure 3-3, the UCR averaged particle decay rate decreased from ~6 day^{-1} (old collapsible chamber, without coagulation correction, ~3 day^{-1} with coagulation correction) to ~1 day^{-1} (new fixed-volume chamber with coagulation correction). The particle decay rate in the old UCR chamber was nearly consistent across regular lab study range of particles due to the surface charge effects of the Teflon film (Le and Li, et al., 2022). Therefore, the old UCR chamber ran day-by-day particle decay rate fit of the total particle number concentration data and conducted size-independent particle wall loss correction using the fitted decay rate (Cocker et al., 2001). It is noted that the coagulation effect can also contribute to the number concentration decay, in addition to the particle wall loss, but

was neglected in the original wall loss correction method due to the previous assumption of negligible coagulation effects at relatively low number concentration (β was fitted using data close to the end of the experiment). The coagulation effect is now found to be able to account for ~50% of the total particle number decay in experiments using the UCR old collapsible chamber with N around 40,000 particles cm^{-3} under typical lab conditions (Le and Li, et al., 2022). The inconsideration of coagulation effects to β in the previous correction method can cause an overestimation in the SOA yield results reported by the UCR old collapsible chamber. The fraction of the overestimation highly depends on the particle concentration and size distribution and will be reported in the future publication of the lab after previous data being reprocessed.

On the contrary, the particle decay rate curve of the UCR new fixed-volume chamber is mostly overlapped with the curve of the Caltech chamber for particle size ≥ 200nm. For particle size < 200nm, the particle decay rate of the UCR fixed-volume chamber is less than the one of the Caltech chamber, which is likely because of the smaller diffusion loss rate of the UCR fixed-volume chamber ($118m^3$ vs Caltech $19m^3$) due to the big size difference of the Teflon bags.

Updated particle loss correction method with UCR fixed volume chamber

Due to the significantly reduced particle wall loss achieved by keeping reactor "neutral", the particle loss caused by coagulation (exceeding detection range) and dilution became notable. The new correction method was built containing both of them and the size dependent particle wall loss. The coagulation code was developed by Chen Le based on

the formula in Atmospheric Chemistry and Physics: From Air Pollution to Climate Change (John Seinfeld and Pandis, 2016). At each SMPS scan interval, the exceed-range particle loss (dV_1) is calculated using the last uncorrected particle number concentration for each size bin, representing the coagulation happened during this interval (typically 2-4 mins). A total exceed-range particle loss (ΔV_1) is formed by summing up the values throughout the experiment. Another new contributor that is considered for the new UCR fixed-volume chamber is the effects from dilution, which was "0" in the previous UCR collapsible chamber due to its positive pressure differential control. The dilution ratio in the new fixed-volume chamber is calculated based on the tracer (e.g. PFH or PFB) mixing ratio change. The particle "loss" (ΔV_2) caused by dilution at a given time t is calculated by equation:

$$\Delta V_2(t) = V_t(\frac{[Trc]_I}{[Trc]_t} - 1),$$

where V_t represents the uncorrected volume concentration at t according to SMPS data, $[Trc]_I$ and $[Trc]_t$ represents the initial mixing ratio and mixing ratio at t of the tracer, respectively. It should be noted that $\Delta V_2(t)$ already represents the "total loss" of particles due to dilution at t.

Particle wall deposition, the last contributor to the total particle loss, is decided to be size-dependent for the new UCR fixed-volume chamber. Shown in Figure 3-3, the particle number decay rate (β, day^{-1}) for each size bin was calculated using a function developed based on monodispersed seed deposition tests (Chen Le, paper in preparation).

$$\beta = 8.15100 \times 10^{-6} {D_{pi}}^2 - 4.72675 \times 10^{-3} D_{pi} + 1.14137$$

where D_{pi} is the particle size in nm.

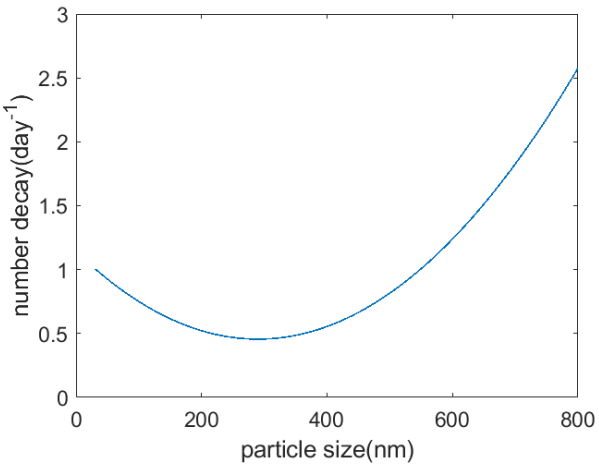

Figure 3-5 Particle number decay rate shown as a function of particle size as used on Feb 24th, 2022 (same as Figure 3-3).

The particle wall deposition loss (ΔV_3) is integrated from corrected number concentration table calculated by a first order kinetics described in Cocker et al. (2001). The total particle loss at t is then the sum of $\Delta V_1(t)$, $\Delta V_2(t)$ and $\Delta V_3(t)$.

New Particle Loss Correction Method Validation

Particle loss test with pure seed injection only were carried out in the new UCR fixed volume chamber to validate the new particle loss correction method. Particle data analysis using the updated particle loss correction method introduced above shows 100% recovery of the initial particle loading (Figure 3-5). Table 3-2 shows that dilution and particle wall deposition contributed the majority of the total particle loss in this case. Although exceed measurement loss due to coagulation is negligible here, it may cause a notable loss with larger particle size at higher number concentration and/or a narrow detection range.

Table 3-3 Particle loss correction of pure seed test in the new UCR fixed-volume chamber. Unit: $\mu m^3 cm^{-3}$.

Initial volume	Corrected end volume	Uncorrected end volume	Exceed range loss ΔV_1	Dilution loss ΔV_2	Particle deposition loss ΔV_3
37.97(±0.66)	38.05(±0.79)	30.61(±0.74)	0.25(±0.00)	4.06(±0.14)	2.57(±0.02)
Fraction to total particle loss			3.6%	59.0%	37.4%

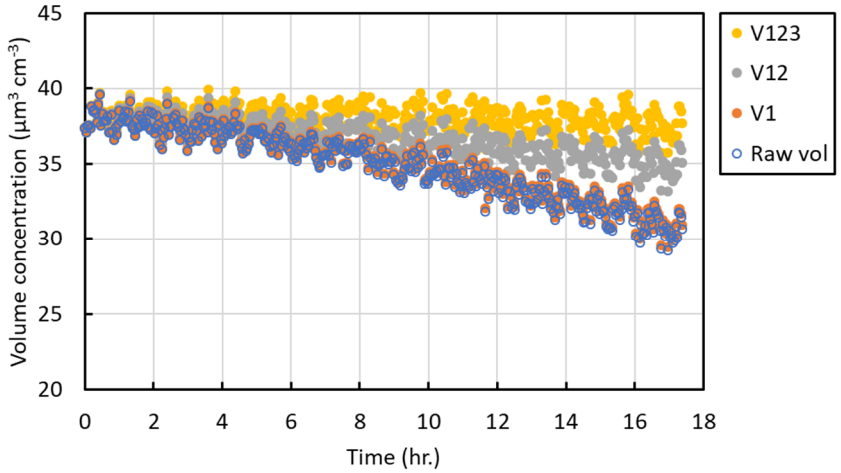

Figure 3-6 Uncorrected and corrected particle volume concentration shown as a function of time. Data shown is being corrected by (V1) exceed measurement range loss due to coagulation, (V12) V1 plus dilution correction, (V123) V12 plus size dependent particle wall loss.

The new UCR fixed-volume chamber was also characterized with a series of repeated oxidation experiments of m-xylene. The final SOA mass yield of the selected experiments were similar between the old and new UCR chambers after data being corrected using the two particle loss correction methods, respectively. However, the SOA mass yield was corrected by 100-300% for particle loss in the UCR old chamber while in the new chamber the correction was much smaller: 2-4% of raw final volume concentration. It is noted that, in the processing of particle loss correction, the data from the UCR old chamber did not include coagulation effects or vapor wall loss, among which the former one can cause an overestimation of the SOA formation while missing the latter one can cause an underestimation of the SOA formation. The exploration of the real offset of the data

requires reprocessing of the previous data using coagulation engaged correction method and future investigation on vapor wall loss dependence on the physical and chemical properties of VOC. Furthermore, the below measurable difference in SOA formation between seeded and non-seeded m-xylene experiment observed in the old UCR chamber (Li et al., 2016) could likely be explained by the missing of coagulation correction. The pre-injected seed could lead to a possible less overestimation of SOA formation in experiments done with seed than without seed due to the nucleation restriction by seed.

3.2.2.2 Vapor wall loss

Benefited by the low particle wall loss rate, vapor wall loss effects were revealed in the new UCR fixed volume chamber. Figure 3-7 shows final SOA mass yield increases by around 80% from 0.046 to 0.083 as seed surface area concentration increases (Table 3-4 Corrected initial *V*). The final SOA mass yield nearly plateaus at high seed loading. The difference in SOA mass formation is due to vapor (oxidation products) wall loss and its associated effects on stopped further oxidation when vapor losses to wall. The observation supported the existing of vapor wall loss in the new UCR fixed-volume chamber but the plateaued SOA mass yield may still not be free of vapor wall loss at such seed surface area concentration suggested by modeling works (Krechmer et al., 2020; La et al., 2016).

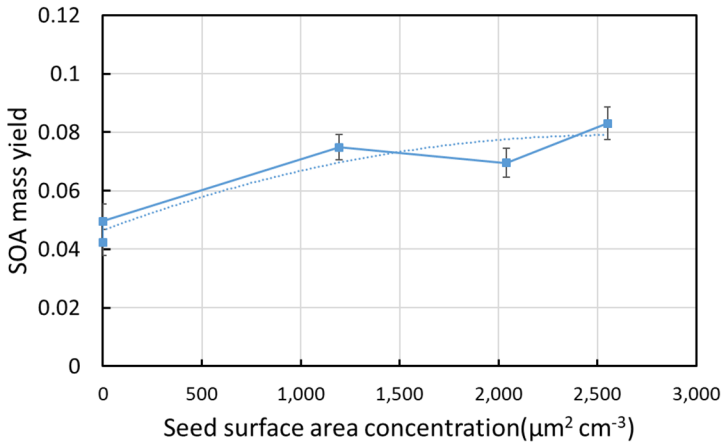

Figure 3-7 Oxidation of m-xylene under different $(NH_4)_2SO_4$ seed loadings in the new UCR fixed volume chamber with corrected initial *V* of seed.

Table 3-4 Experimental conditions and parameters of a series of ·OH initiated oxidation experiments of m-xylene at varying seed loading. Data is shown with corrected initial volume concentration (+7.7%) and uncorrected initial volume concentration.

	Expt.	SOA mass yield	Seed area	Initial V	End V	ΔV_1	ΔV_3	ΔV_2	Dilution	Total correction	Δ[HC]	Corrected SOA
			$\mu m^2\ cm^{-3}$	$\mu m^3\ cm^{-3}$	$\mu m^3\ cm^{-3}$	$\mu m^3\ cm^{-3}$	$\mu m^3\ cm^{-3}$	$\mu m^3\ cm^{-3}$	%	$\mu m^3\ cm^{-3}$	$\mu g\ cm^{-3}$	$\mu g\ cm^{-3}$
Corrected initial V	2701	0.042	0	0.05	9.33	0.000	0.210	0.104	1.107	0.315	317.24	13.43
	2688	0.050	0	0.04	9.76	0.000	0.208	0.199	2.000	0.407	286.00	14.17
	2693	0.075	1194	38.04	53.01	0.004	0.927	1.304	2.400	2.234	321.87	24.09
	2684	0.070	2040	76.03	85.69	0.038	1.954	2.489	2.823	4.481	284.82	19.80
	2689	0.083	2552	96.16	107.30	0.036	2.011	1.717	1.575	3.764	251.24	20.87
Uncorrected initial V	2701	0.042	0	0.05	9.33	0.000	0.210	0.104	1.107	0.315	317.24	13.43
	2688	0.050	0	0.04	9.76	0.000	0.208	0.199	2.000	0.407	286.00	14.17
	2693	0.087	1194	35.32	53.01	0.004	0.927	1.304	2.400	2.234	321.87	27.90
	2684	0.096	2040	70.59	85.69	0.038	1.954	2.489	2.823	4.481	284.82	27.41
	2689	0.121	2552	89.28	107.3	0.036	2.011	1.717	1.575	3.764	251.24	30.49

An interesting finding during the study is that the determination of initial volume concentration of the seed can strongly affect the SOA mass yield trend or even drive the trend, leading to misunderstanding of the vapor wall loss effects. Shown in Table 3-4 and Figure 3-8, when initial volume concentration of the seed is not corrected for a 7.7% underestimation, the plotted SOA mass yield keeps an obviously increasing trend at even high seed level. The SOA mass yields of seeded experiments were significantly overestimated by ~16-46% in this case depending on seed level and seed size distribution. Generally, higher seed level would lead to greater overestimation of the SOA formation when size distribution stays relatively constant. The 7.7% correction fraction of the initial particle volume concentration was derived from two pure seed deposition tests that were done at similar seed level as the m-xylene experiments shown here. The volume concentration of the pure seed grew ~7-8% in the first 3-6 hours after seed injection stopped and operator performed internal mixing. Possible reasons for this increase include missing reading of sub-measurement fine particles of SMPS, low charging efficiency of particles

with smaller diameter by nebulizer of SMPS, and estimation error of SMPS when particle size distribution peak shifts from small diameters to large diameters. More studies are required for further investigation on this.

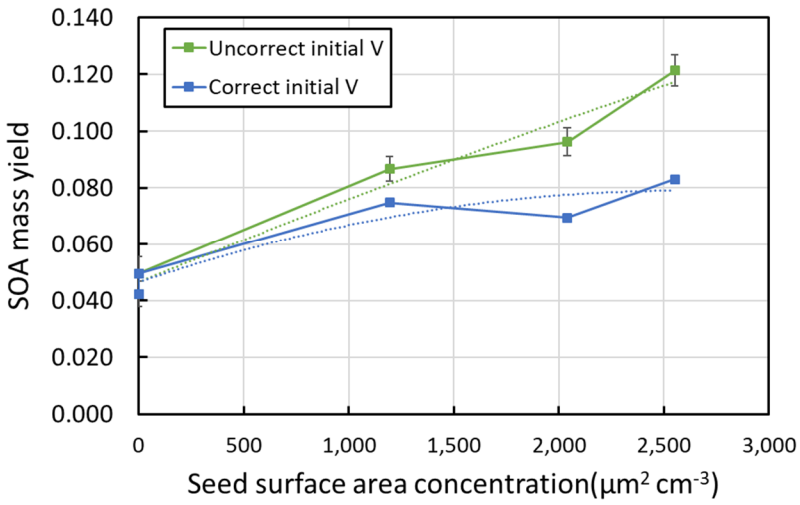

Figure 3-8 Correction of initial volume affects the trend between SOA mass yield of m-xylene and surface area of seed.

3.3 Experimental Protocol Validation with Case Study on Benzyl Alcohol and Other VCPs

3.3.1 Chamber comparison

The chamber comparison was conducted with series of experiments on the oxidation of benzyl alcohol being carried out to consolidate the understanding of effects from factors that are different between chambers. The SOA mass yield results were significantly different at the beginning of the comparison with Caltech reporting yields over 1.5 while UCR reporting yields below 0.65. Experiments done in UCR old chamber had initial [HC] ranged from 60ppb to 180ppb with 20-100ppb NO_x, while conditions of Caltech experiments can be found in (Charan et al., 2020). The gap was figured out to be caused by the side peak of benzaldehyde (Figure 3-9) shown on the GC which was likely caused by heat degradation of benzyl alcohol on metal sampling line of GC and was not accounted for originally. The side peak was estimated to cause a ~60% underestimation of the injected benzyl alcohol mixing ratio. To solve the problem, Caltech switched to the CIMS data for determination of reacted benzyl alcohol while replacing GC metal sampling part with Teflon material. UCR double-checked on the effects of the side peak and found its effects to be negligible (Figure 3-9, note the secondary y axis is not in ppb but area shown on GC).

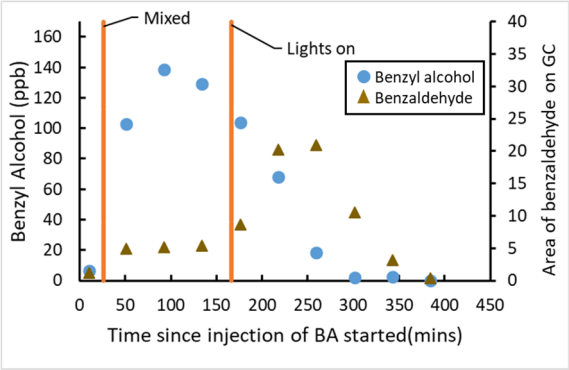

Figure 3-9 Monitoring mixing ratios of benzyl alcohol and benzaldehyde over time.

After the major correction on the Δ[HC], the gap was closed enough to show overlaps at the middle SOA formation range (Figure 3-10). However, shown in the left figure of Figure 3-10, the averaged SOA mass yield observed in the Caltech chamber was still higher than the ones observed in the UCR chamber. To investigate the possible reason for why UCR chamber could not reach a higher SOA mass yield or, in other words, higher SOA formation after the same irradiation duration of the experiments done under similar initial conditions in the Caltech chamber, all data was reprocessed with an assumption of Ω=1, which is assuming gas-particle partitioning can still happen after particle deposited onto chamber wall. The output results were not encouraging that although SOA mass yields from the UCR chamber increased and reached similar high SOA mass yield the absolute SOA formation was still low. This indicated that Ω was not the key missing factor that suppressed the SOA formation. However, the significant increase of SOA mass yield after applying Ω=1 in the UCR data reveals how sensitive the corrected results can be to the value of Ω when the particle number decay is huge. The Caltech data shows very little difference between Ω=1 and Ω=0. A comparison of particle number concentration and volume concentration during typical benzyl alcohol experiments done in UCR old chamber

and Caltech chamber are shown in Figure 3-11, which shows the UCR volume correction fraction is 4 times higher than one of Caltech chamber. An advantage of keeping chamber "neutral" is perfectly reflected here by the case study of benzyl alcohol: the effects from partitioning assumption of whether deposited particle keeps growing or not is negligible when chamber is "neutral".

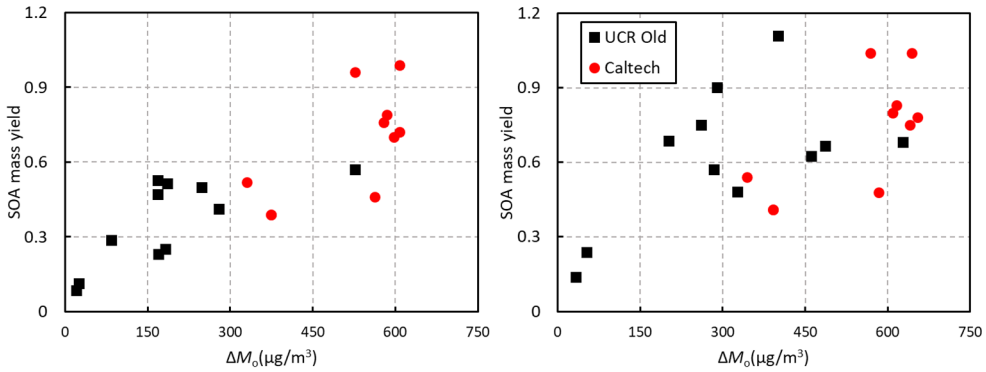

Figure 3-10 SOA mass yield shown as a function of SOA formation. Left with assumption of Ω=0; right with assumption of Ω=1.

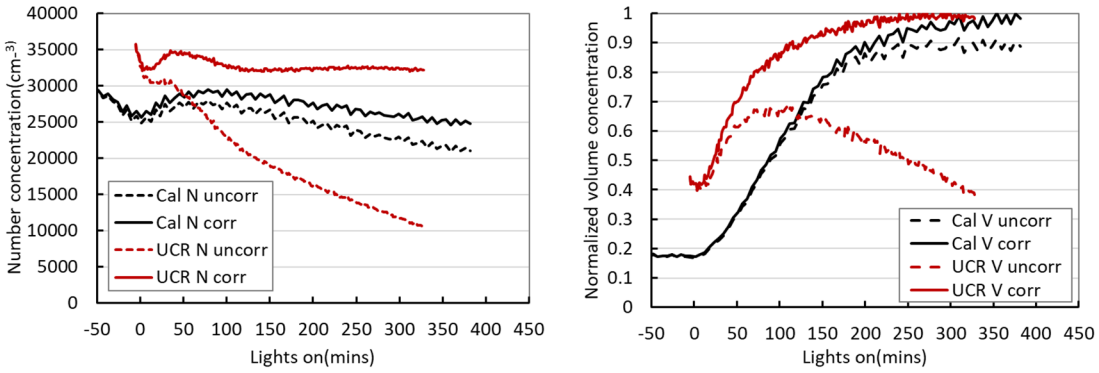

Figure 3-11 Particle number concentration and volume concentration shown as a function of time of typical benzyl alcohol experiment in UCR old chamber and Caltech chamber.

3.3.2 Discrepancy still exists in seed effect

The seed effects in oxidation of benzyl alcohol observed in Caltech chamber (Figure 3-12 modified plot with permission from authors) (Charan et al., 2020) were not confidentially reproduced in either the old or the new UCR chamber. The data from UCR old collapsible chamber does show an increasing over seed surface area. However, the two points with the lowest SOA yield shown in Figure 3-12 were experiments conducted with 50% light intensity. In addition, considering the particle loss correction method used in the UCR old collapsible chamber likely overestimated the SOA yield in the presence of seed. The trend should be re-evaluated after the data being reprocessed using updated wall loss correction and coagulation correction.

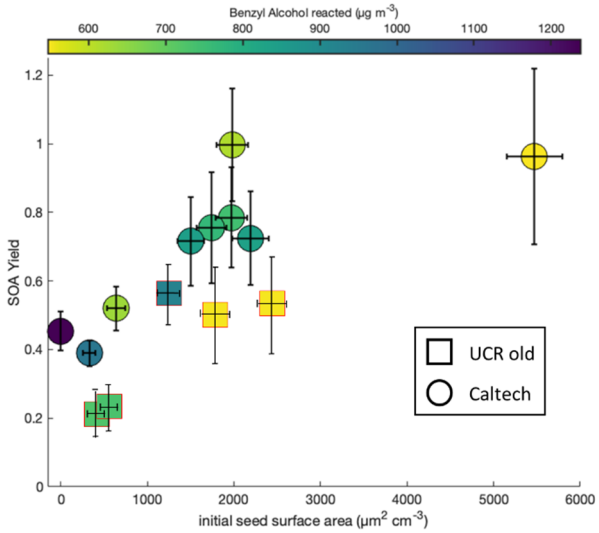

Figure 3-12 Oxidation of benzyl alcohol at different seed levels in UCR old collapsible chamber and Caltech chamber.

Although vapor wall loss is suggested in m-xylene experiment, the seed effect in oxidation of benzyl alcohol in the new UCR fixed volume chamber is unclear and requires more experiments. Figure 3-13 shows the high seed level did not lead to a higher SOA mass

yield using the updated particle loss correction methods. This may be due to the different chemical and physical property of benzyl alcohol (as an LVP-VOC) compared to m-xylene but further investigation is definitely required before any speculations being given.

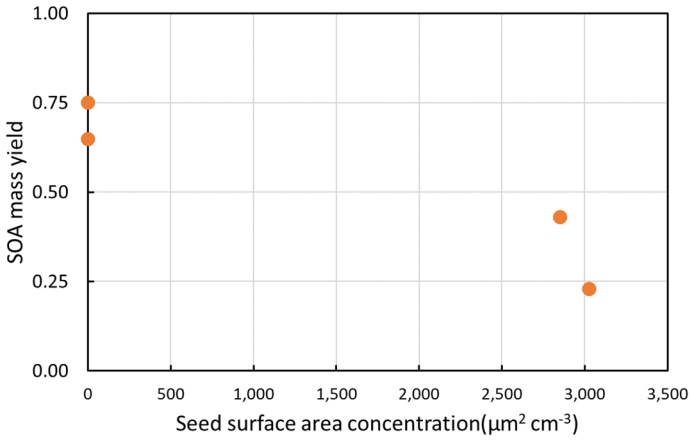

Figure 3-13 SOA mass yield from oxidation of benzyl alcohol with and without seed.

3.3.3 SOA formation from oxidation of other selected VCP compounds

A series of other selected VCP related VOCs was studied in the new UCR fixed-volume chamber by following the refined experimental protocol validated by the presented work as mentioned above. A summary of the experiments is presented in Table 3-5 with phenoxyethanol and hexylene glycol showing notable amount of SOA formation. This is going to lead to a publication with a discussion of the selected VOCs that were tested here in the VCPs category.

Table 3-5 Summary of oxidation results of selected VCP related VOC.

Name	Initial Conditions	SOA mass yield	SOA mass formation

	[HC] ppb	[NO_x] ppb	[H_2O_2] ppm		μg m^3
Phenoxyethanol	200	0	1	>7%	57.0
Hexylene glycol	200	0	1	5.3%	19.4
i-butyl acetate	80	0	1	0	0.01
Decamethylcyclopentasiloxane	80	0	1	0	0.4
*Propylene glycol methyl ether	80	0	1	*0	0.02
	80	50	1	*0	0.21
*Dipropylene glycol	300	100	3	*0	0.3
Tetrahydrofuran	80	0	1	0	0.05
Ethyl acetate	80	0	1	0.76%	0.35
	80	100	1	0	0.01

*Cannot be detected by GC-FID under such mixing ratio or due to tubing delay that requires further modification.

3.4 Conclusions

Here we presented a detailed comparison of chambers between UCR old collapsible chamber and UCR new fixed volume chamber and Caltech chamber in basic setups and key differences with critical perimeters that SOA formation are highly sensitive to. The quantification of reacted hydrocarbon and increased SOA volume concentration requires accurate evaluation of the data. With advanced understanding from the comparison, the 300% gap in SOA mass yield of benzyl alcohol was closed by eliminating a confusing side peak (which is also products from oxidation) of benzaldehyde from the GC. In addition, with advanced understanding on the surface static charge effects of bags on particle loss, the particle number decay rate was reduced by a factor of 6 compared to old UCR

collapsible chamber. An updated three-component (including exceeding detection range loss, chamber dilution, and particle wall loss) particle loss correction method was presented, which was validated by explaining 100% of particle loss in pure seed deposition tests. By reducing the particle wall loss rate of particles at the middle size range (200-500 nm), the vapor wall loss was observed in the oxidation experiments of m-xylene with varying initial seed surface area concentrations, while applying the updated three-component particle loss correction. The lack of consideration of coagulation effect in the previous particle loss correction method in the old UCR collapsible chamber could be the reason for no measurable SOA mass yields difference in seeded and non-seeded oxidation experiments of m-xylene. Depending on the size distribution and number concentration of the seed, the inconsideration of coagulation effects may cause overestimation of SOA mass yield by a significantly varying range. The SOA mass yield from oxidation of m-xylene without seed can be 50% overestimated by using the previous correction method in the old UCR collapsible chamber when compared to the results processed with coagulation corrected particle wall loss rate. The study reveals another scenario, under which the vapor wall loss potential observed in multi-level seed experiments can be caused by/ affected by not fully accounting for the sub-measurement particles. The pure seed deposition experiments suggested the sub-measurement particles can account for over 7% of the total particle volume at ~40,000 cm^{-3} with initial peak diameter being at ~84nm.

This work provided concerning parameters and recommendations to all groups who use environmental chambers. UCR chamber keeps exploring the effects of varying factors to advance the understanding of chamber system and refine the data analysis.

3.5 Reference

Carter, W. P. L., Pierce, J. A., Luo, D. and Malkina, I. L.: Environmental chamber study of maximum incremental reactivities of volatile organic compounds, Atmos. Environ., 29(18), 2499–2511, doi:10.1016/1352-2310(95)00149-S, 1995.

Charan, S. M., Kong, W., Flagan, R. C. and Seinfeld, J. H.: Effect of particle charge on aerosol dynamics in Teflon environmental chambers, https://doi.org/10.1080/02786826.2018.1474167, 52(8), 854–871, doi:10.1080/02786826.2018.1474167, 2018.

Charan, S. M., Buenconsejo, R. S. and Seinfeld, J. H.: Secondary organic aerosol yields from the oxidation of benzyl alcohol, Atmos. Chem. Phys., 20(21), 13167–13190, doi:10.5194/ACP-20-13167-2020, 2020.

Cocker, D. R., Flagan, R. C. and Seinfeld, J. H.: State-of-the-art chamber facility for studying atmospheric aerosol chemistry, Environ. Sci. Technol., 35(12), 2594–2601, doi:10.1021/es0019169, 2001.

Jahn, L. G., Wang, D. S., Dhulipala, S. V. and Ruiz, L. H.: Gas-Phase Chlorine Radical Oxidation of Alkanes: Effects of Structural Branching, NOx, and Relative Humidity Observed during Environmental Chamber Experiments, J. Phys. Chem. A, 125(33), 7303–7317, doi:10.1021/ACS.JPCA.1C03516/SUPPL_FILE/JP1C03516_SI_001.PDF, 2021.

Krechmer, J. E., Day, D. A. and Jimenez, J. L.: Always Lost but Never Forgotten: Gas-Phase Wall Losses Are Important in All Teflon Environmental Chambers, Environ. Sci. Technol., 54(20), 12890–12897, doi:10.1021/ACS.EST.0C03381/SUPPL_FILE/ES0C03381_SI_001.PDF, 2020.

La, Y. S., Camredon, M., Ziemann, P. J., Valorso, R., Matsunaga, A., Lannuque, V., Lee-Taylor, J., Hodzic, A., Madronich, S. and Aumont, B.: Impact of chamber wall loss of gaseous organic compounds on secondary organic aerosol formation: Explicit modeling of SOA formation from alkane and alkene oxidation, Atmos. Chem. Phys., 16(3), 1417–1431, doi:10.5194/ACP-16-1417-2016, 2016.

Le, C., Li, Q. and Cocker, D. R.: Characterization of Environmental Chamber Wall Loss, in preperation, expect to publish in 2022

Li, L., Tang, P., Nakao, S., and Cocker, D. R.: Impact of molecular structure on secondary organic aerosol formation from aromatic hydrocarbon photooxidation under low-NOx conditions, Atmos. Chem. Phys., 16, 10793–10808, https://doi.org/10.5194/ACP-16-10793-2016, 2016.

McDonald, B. C., De Gouw, J. A., Gilman, J. B., Jathar, S. H., Akherati, A., Cappa, C. D., Jimenez, J. L., Lee-Taylor, J., Hayes, P. L., McKeen, S. A., Cui, Y. Y., Kim, S. W.,

Gentner, D. R., Isaacman-VanWertz, G., Goldstein, A. H., Harley, R. A., Frost, G. J., Roberts, J. M., Ryerson, T. B. and Trainer, M.: Volatile chemical products emerging as largest petrochemical source of urban organic emissions, Science (80-.)., 359(6377), 760–764, doi:10.1126/SCIENCE.AAQ0524/SUPPL_FILE/AAQ0524_MCDONALD_SM.PDF, 2018.

Nakao, S., Shrivastava, M., Nguyen, A., Jung, H. and Cocker, D.: Interpretation of Secondary Organic Aerosol Formation from Diesel Exhaust Photooxidation in an Environmental Chamber, http://dx.doi.org/10.1080/02786826.2011.573510, 45(8), 964–972, doi:10.1080/02786826.2011.573510, 2011.

Odum, J. R., Jungkamp, T. P. W., Griffin, R. J., Flagan, R. C. and Seinfeld, J. H.: The atmospheric aerosol-forming potential of whole gasoline vapor, Science (80-.)., 276(5309), 96–99, doi:10.1126/SCIENCE.276.5309.96/ASSET/DA3A2F20-FC6E-4C6C-B780-C9BED98B53E0/ASSETS/GRAPHIC/SE1274925003.JPEG, 1997.

Seinfeld, J. H., and Pandis, S. N. (2016). Atmospheric Chemistry and Physics: From Air Pollution to Climate Change. John Wiley & Sons, Hoboken, 3rd edition.

Toro, D., McMurry, P. H. and Grosjean, D.: “A Rapid Method for Estimating Log P for Organic Chemicals” Gas and Aerosol Wall Losses in Teflon Film Smog Chambers^, J. Fish. Res. Board Can, 19(23), 457 [online] Available from: https://pubs.acs.org/sharingguidelines (Accessed 19 February 2022), 1985.

Chapter 4 : Health Effects Investigation of Salton Sea Spray on Mice Using Animal Whole-Body Exposure Environmental Chamber

4.1 Introduction

The Salton Sea is a 345 mi^2 inland body of water located in California's Riverside and Imperial counties. The Sea is primarily fed by agricultural runoff as well as inflow from the Alamo, New, and Whitewater rivers. In recent decades, the Sea has been undergoing a rapid retreat. This retreat is causing increased exposure of dry lakebed (playa), resulting in increased dust production which is spreading throughout the region and impacting the surrounding population. Moreover, the drying Sea has become hypersaline, at approximately 74 parts per thousand, over twice that of Pacific Ocean water (Bureau of Reclamation, 2020). The consequent rapid change in the Sea's ecology has resulted in periodic algal blooms, and fish and migratory bird dieoffs (Carmichael and Li, 2006; Xu et al., 2016). Pesticide and herbicide use from agricultural areas located to the southeast and northwest of the Sea (Xu et al., 2016), as well as heavy metal contamination from

elements such as selenium (Zhou et al., 2017), paint an overall picture of ill-health in the Sea itself.

This ecosystem's ill health is also reflected in the surrounding communities. The human population surrounding the Salton Sea includes a high proportion of migrant workers, with high rates of poverty and poor access to health care. Area residents suffer from one of the highest rates of childhood asthma in California at 20%–22.4%, compared to an average of 14.5% for the rest of the State (Farzan et al., 2019). Predictably, the surrounding area also has one of the highest rates of hospitalization for asthma (California Environmental Protection Agency, 2018), making it a serious health crisis in an already underserved community.

Asthma is a disease of airway restriction, defined as an increase in airway hyperreactivity, and usually associated with allergies (referred to as “atopic” asthma), characterized by increased immunoglobulin E (IgE) production, Th2 cytokine secretion and the recruitment of eosinophils to the lungs (Bousquet et al., 2000). Atopic asthma exacerbations can occur in response to exposure to environmental or household allergens (Wark and Gibson, 2006). High levels of particulate matter (PM) have also been known to exacerbate asthma (Guarnieri and Balmes, 2014). Unfortunately for the communities surrounding the Salton Sea, there are many potential allergens and asthma exacerbating particles. The region has consistently high levels of particulate matter between 10 μm and 2.5 μm in diameter (PM10) and under 2.5 μm in diameter (PM2.5; Environmental Protection Agency, 2012; Evan, 2019; Frie et al., 2019). Indoor household allergens, such as Alternaria alternata, and other fungi, are also prevalent (Sinclair et al., 2018). Up to 70% of patients with fungal allergies

show a positive skin test response to Alternaria (Bush and Prochnau, 2004). Additionally, household Alternaria exposure is linked to an increased odds ratio for developing asthma symptoms (Salo et al., 2006).

However, the region's rampant asthma may have more complex origins than simple dust levels, largely pointing to the Salton Sea itself. Studies have identified a variety of pesticides, including DDT, organophosphates and pyrethroid, in both the water and the sediment of sites around and within the Sea (LeBlanc and Kuivila, 2008). Organophosphates have been linked to increased risk of childhood asthma (Shaffo et al., 2018). Additionally, the Sea experiences periodic algal blooms and has been shown to contain low levels of microcystin-LR and YR, cyanotoxins known to cause ill-health (Carmichael and Li, 2006). These microcystins have been shown to cause damage to the lungs after chronic exposure (Li et al., 2016; Wang et al., 2016). Some algal blooms, such as red tides off the coast of Florida, have also been directly linked to the development of asthma and asthma exacerbations (Fleming et al., 2007; Zaias et al., 2011). Additionally, cyanobacteria, which make up a large part of algal blooms, may serve directly as sensitizing allergens, exacerbating the harmful effects of the algae (Bernstein et al., 2011).

Despite suggestive associations between the Salton Sea and asthma, more direct mechanistic information on Salton Sea aerosols and their potential impact on pulmonary health are still needed. To address this issue, we began studies to simulate chronic aerosol exposures in a mouse model of pulmonary inflammation. In the present study, we focused on the direct effect of Salton Sea “spray” aerosols on lung responses.

4.2 Materials and methods

4.2.1 Water sample collection

Two batches of Salton Sea water were collected at the edge of Salton City. The first was collected on March 2nd, 2019 (33°19′25.9″N 115°56′ 18.3″W) and the second was collected on May 13th, 2020 (33°19′53.2″ N 115°56′30.0″W). Water samples were collected with a homemade raft; because aerosols are most likely generated at the surface layer of the sea, the design of the raft aims to collect water from the top few centimeters of the water column. Four sampling ports were square distributed, sticking out of the bottom of the raft at a length of 2 in., to ensure sampling surface water only and avoiding floating debris. Two 4.96 m poles were installed and used to move the raft to places with large depth. Water samples were taken by a hand pump on the shore. The whole system was sterilized thoroughly by bleach solution and flushed by MilliQ water before being used on site. More than 2 L of water samples were taken before sample collection to rinse the system. The collected water was stored on ice while transported to the University of California, Riverside campus. Once there, water samples were stored at 4 °C until processed. Pacific Ocean water was also collected in two batches. The first was collected at Torrey Pines on March 9th, 2019. The second was also collected at Torrey Pines on October 2nd, 2020 (32°55′51.4″N 117°15′ 37.7″W). Water was collected directly by containers without using the raft since ocean water is relatively well mixed due to tides. Samples were stored at 4 °C until processed.

4.2.2 Water processing

Before using for aerosolization studies, the water was filtered through an acid-washed, sterilized glass funnel using a sterile 0.2 μm filter (47-mm diameter; Pall Supor 200 Sterile Grid filters, Pall Corporation, Por Washington) into an acid-washed sterilized collecting flask below via vacuum filtration. After filtration, filtrate was either stored at 4 °C or as aliquots archived at −80 °C for long-term storage. The pH of all filtrates was measured; all filtrates were approximately pH 7.0 (±0.8%). The filtered water was stored for various periods from weeks to several months between collection and use in the chamber exposure studies; we were unable to detect any difference in the magnitude of the reported effects on mouse lung responses associated with storage time.

4.2.3 Animals

Animal studies were performed in accordance with UCR institutional IACUC and NIH guidelines and approved protocols. Adult male and female (8–9 weeks old) C57BL/6 J mice were purchased from Jackson Labs, Sacramento. Mice were acclimated for one week in the University of California, Riverside SPF vivarium before being placed into the exposure chamber when they were 9–10 weeks old. Mice were kept 3–4 to a cage and given food and water ad libitum, with bedding being changed at least once weekly. A 12-hour day/night cycle was provided. Exposure studies were performed in dual animal chambers (an exposure chamber and a control chamber) developed from the chamber described in Peng (2019). When in the exposure chamber, mice were given a mixture of dry filtered air (0.5–1 lpm) and aerosolized spray (dried by silica gel, 3.5–4.5 lpm) with a total particle

concentration of approximately 1500 μg m^{-3} . The three types of PM were generated from solutions of Alternaria alternata and Alternaria tenuis filtrate (Greer Laboratories, Lenoir, NC, USA; 0.4 g/L), Salton Sea water (133-200× dilution), or Pacific Ocean water (40× dilution) with proper concentrations or dilution ratios, respectively. Example of typical exposure PM levels for different PM types are shown in Fig. 4-1a with weekly averaged PM level being 1425 μg m^{-3} for Alternaria, 1377 μg m^{-3} for Pacific Ocean spray, and 1523 μg m^{-3} for Salton Sea spray. Sample aerosolization was accomplished by using a homemade nebulizer with silica-gel dryers (Peng et al., 2019). Mice in the control chamber were given filtered dry air (5.0 lpm) only, with other conditions the same as the exposure chamber, including bedding replacement, food and water supplies, and corresponding day/night cycle. Particulate matter was only monitored within the exposure chamber by a scanning mobility particle sizer (SMPS, including Series 3080 Electrostatic Classifier and Ultrafine Condensation Particle Counter 3776, TSI) to assist in maintaining stable PM concentration of 1500 μg m^{-3}. Concentration was similar to our previous study in Peng et al. (2018), 24 where 1500 μg m^{-3} of Alternaria was sufficient to generate neutrophil and eosinophil recruitment to the lungs. Relative humidity (40–60%) and ammonia (weekly averaged $[NH_4] < 25$ ppm) were selectively measured in some of the exposures to ensure consistent quality control. For each exposure, we used an equal number of male and female mice. Each exposure had a control air cohort that matched the number and sex of the exposure group. The number of mice for each exposure is as follows: 8 mice for the 3/2/2019 Salton Sea collection, 10 mice for the 5/13/2020 Salton Sea collection, 4 mice for

the 3/9/2019 Pacific Ocean collection, 6 mice for the 10/2/2020 Pacific Ocean collection, 10 mice for the Alternaria exposure.

After 7 days, the mice were removed from the chamber, anesthetized via isoflurane and sacrificed by cervical dislocation. The mice were then processed for either RNA extraction and flow cytometry or histological analysis. For the RNA extraction/flow cytometry mice, BALF was collected via 3 injections of 0.8 mL PBS, after which the right lung lobe was extracted and flash frozen in liquid nitrogen and kept at −80 °C until RNA extraction, while the left lobe was digested using 0.5 mg/mL collagenase D (Roche Diagnostics, Mannheim, Germany), 50 U/mL DNAse I (Sigma Aldrich, St. Louis, USA) in RPMI 1640 (Gibco, Grand Island, USA) supplemented with 10% heat-inactivated FBS (Gibco, Grand Island, USA) preheated to 37 °C. The lung was left to digest for 30 min at 37 °C before being diced into small (~1–2 mm) sections and pushed through a cell strainer (Corning, Corning, USA). The cell strainer was rinsed with RPMI 1640 with 10% heat-inactivated FBS before being centrifuged and resuspended for use in Flow Cytometry. For the histological mice, the lung was inflated with 0.7 mL of a 1:1 OCT:PBS mixture before being flash frozen via liquid nitrogen in an OCT block.

4.2.4 Flow cytometry

BALF and post-digested lungs were centrifuged at 1500 rpm before being resuspended in 100 μL of a 1:50 dilution of Mouse BD FC block (BD Pharmingen, San Jose, USA; Clone 2.4G2) in FACS Buffer. Cells were stained using fluorescent antibodies: anti-CD45 FITC (BioLegend, San Diego, USA; Clone 30-F11), anti-CD19 PE-Cy5

(eBioscience, San Diego, USA; Clone MB19-1), anti-CD3 Alexa Fluor 700 (BioLegend, San Diego, USA; Clone 17A2), anti-Ly6G BV510 (BioLegend, San Diego, USA; Clone 1A8), anti-CD11b BV421 (BioLegend, San Diego, USA; Clone M1/70), anti-CD11c PE-Cy7 (BioLegend, San Diego, USA; Clone N418) and anti-SiglecF APC (BioLegend, San Diego, USA; Clone S17007L). Samples were run on a MoFlo Astrios (Beckman Coulter, Carlsbad, USA). Gating and analysis were performed using FlowJo (Version 10.71, Ashland, USA). Note that the figures show different Yaxis ranges in order to best illustrate the magnitude of the differences in cells recovered from lavage versus tissue; however, the absolute values are also presented in the text.

4.2.5 RNA extraction

RNA was extracted using TRIzol© (Ambion, Carlsbad, USA). Briefly, ~100 mg of frozen lung tissue was placed in a mortar, covered with liquid nitrogen, then ground into dust using a pestle before adding to TRIzol©. Chloroform was added, mixed and centrifuged. The aqueous phase was removed and mixed with isopropanol and centrifuged, leaving a pellet which was then washed 3× with 75% ethanol before drying at room temperature. The pellet was resuspended in DEPC-Treated water (Ambion, Austin, USA). Concentration and purity of RNA was checked via NanoDrop 2000 (Thermo Scientific, Carlsbad, USA).

4.2.6 NanoString analysis

Purified RNA was analyzed using an nCounter® Sprint Profiler (NanoString Technologies, Seattle, USA) with the nCounter® Mouse Immunology Panel according to manufacturer

protocols. Gene expression was analyzed using the nSolver® 4.0 software (NanoString Technologies, Seattle, USA). Statistical analysis was done using nSolver® Advanced Analysis 2.0 (NanoString Technologies, Seattle, USA); false discovery rates (FDR) were calculated, using the Benjamini-Hochberg method.

Differences in lung immune gene expression profiles (from nCounter® Mouse Immunology Panel) for each mouse sampled were analyzed using Principal Component Analyses (PCA; Pielou, 1984) using the "prcomp" function in R version 4.0.3 (R version 4.0.3; R Core Team, 2020). Normalized and log transformed gene expression data matrices were constructed as data points were projected onto the 2-D plane, such that the variance is maximized. As dimensions were reduced, they spread out in two directions to explain most of the differences in the data. X-axes (labeled as PC1) in the ordination space represent the first principal component, which separates data points to represent the most variation in the dataset; y-axes (labeled as PC2) are orthogonal to PC1 and separate data points to represent the next greatest amount of variation within these gene expression datasets, across exposure types. We used the ggplot2 package (Wickham, 2009) and the "stat ellipse" function, with 95% confidence intervals, to visualize these PCA plots in R (R version 3.2.1; R Core Team, 2017).

4.2.7 Histology

OCT embedded lungs were sectioned at 20 μm in a Cryostat. Sections were stored at −80 °C until staining. Before staining with H&E, slides were fixed with 4% PFA for 10

min. Histological images were taken using a Keyence BZ-X710 (Keyence Corporation of America, Itasca, USA).

4.2.8 Aerosol mass spectrometry

Chemical composition of aerosolized particles was measured by an HR-ToF-AMS (DeCarlo et al., 2006) Particles were generated using the same atomizer system as chamber exposures, as described by Peng et al. (2018). The outlet of our atomizer system was split into two ports, with one connected to the sampling inlet of the aerosol mass spectrometer (AMS) and the other venting through a HEPA filter. The Salton Sea and Pacific Ocean stock samples were diluted 10× with MilliQ water to generate particles at suitable concentrations. Alternaria solutions were the same concentrations as those used in chamber exposures. ToF-AMS Analysis Toolkit 1.57 and PIKA 1.16 on Igor Pro 6.36 were used in data processing.

4.2.9 Statistical analysis

All statistical analysis was done using GraphPad Prism 6 (GraphPad, San Diego, USA). p-Value was calculated using the Mann-Whitney U test for nonparametric data. We analyzed multivariate homogeneity of group dispersions (variances) using PERMDISP2 procedures in the R package vegan, with the function “betadisper” (Oksanen et al., 2016) in R. Euclidean distances between objects and group centroids were handled by reducing the original distances to principal coordinates. We used Tukey's Honest Significant Difference methods as “TukeyHSD.betadisper” to create 95% confidence intervals on differences

between mean distance-to-centroids across exposures, as compared with mice in chambers containing control air.

4.3 Results

4.3.1 Control of exposure to aerosol particulate levels

To ensure consistent levels of simulated chronic environmental aerosol exposures, our environmental chamber system was set up to continuously monitor suspended aerosols by particulate size as well as steady-state mass concentrations. In this study, we performed exposure studies using aerosolized suspensions generated from aqueous solutions of Alternaria filtrate, Salton Sea water, and Pacific Ocean water. Mass concentrations of PM generated from different sources were stable over 7 days, with averaged mass concentrations around 1500 μg m−3 (±10%; Fig. 4-1a). Average size distributions of the different types of PM were generated using the same atomizer system, under identical conditions (Fig. 4-1b). Only minor differences in average particle size were observed between samples; peak particle mobility diameter for Pacific Ocean PM was 79.1 nm; Alternaria PM was 88.2 nm, and Salton Sea PM was 94.7 nm. Because the injection method was consistent between each exposure, minor differences in PM size distribution were primarily due to composition differences of each aerosolized solution. Moreover, differences in particle densities were seen with higher "salty" PM densities, as compared to the "organic" PM (Alternaria PM 1.36 g cm−3 < Pacific Ocean PM 1.96 g cm−3 < Salton Sea PM 2.07 g cm−3). Importantly, a majority of PM was either fine (PM with a diameter

between 0.1 µm–2.5 µm) or ultrafine (PM with a diameter of less than 0.1 µm), with the vast majority of PM under 1 µm in mobility diameter. This is critical to consistent exposure effects, as ultrafine PM is expected to be able to travel deep into lung tissue down to the alveoli.

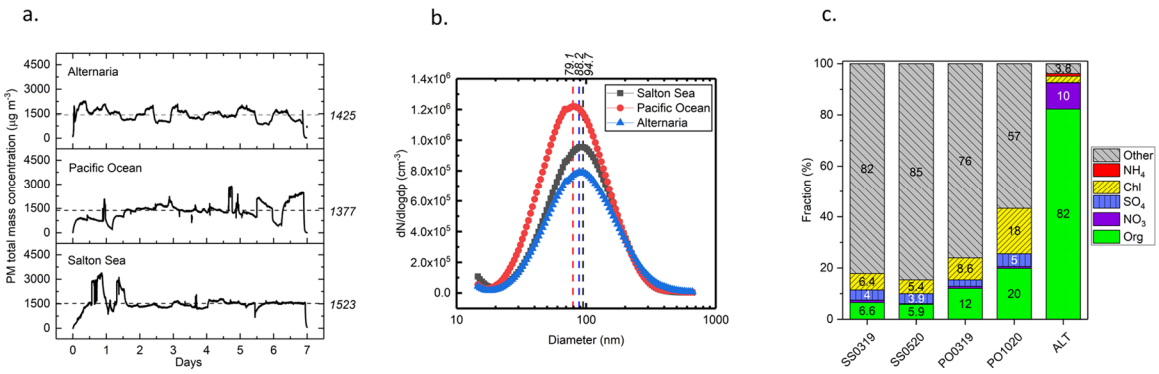

Figure 4-1 Quantification of Alternaria (ALT), Pacific Ocean (PO) and Salton Sea (SS) aerosols. PM mass concentration was measured by a scanning mobility particle sizer. Chemical composition was determined by AMS. (A) PM mass concentration during 7-day exposure of SS, PO and ALT. Dash line shows the 7-day averaged mass concentration of PM. All units are in µg m^{-3}. (B) Averaged mobility diameter distribution of different PM used in exposure experiments. (C) Chemical composition of dry particulate matters generated from different materials collected in different season (mm/yr). Other includes metals (sodium, calcium, magnesium), trace metals and other inorganics. (Key: SS0319, Salton Sea/March 2019; SS0520, Salton Sea/May 2020; PO0319, Pacific Ocean/March 2019; PO1020, Pacific Ocean/October 2020; ALT, Alternaria filtrate).

PM surface area has been proposed to be an important factor in studies on the health effects of PM on lungs. However, as all three types of PM used in this experiment were generated from aqueous solutions, with no inert components; the particles were – by their nature – highly water soluble. Accordingly, particle size could change within the lung due to the high relative humidity of the lung microenvironment (Löndahl et al., 2007); therefore, for comparability across different material exposures, we chose to control the total mass concentration of the different types of PM instead of total surface area.

Due to the complexity of multiple factors, including particle size and depth of penetration into lung tissue, as well as the extent of animal activity, age, or relative humidity fluctuation,

it is difficult to estimate the actual dose of material deposited in the lung of a mouse over the course of a 7-day exposure. Since we maintained a target mass concentration in the chamber, with similar particle size distributions across each of three aerosol suspensions, we expect that particle suspensions of all three materials were delivered in similar fashion. Moreover, since the particles were all generated using aqueous solutions, it is likely that all particles coming into direct contact with lung tissue (i.e., alveolar or airway epithelium) will similarly fully dissolve and release their components to diffuse into the tissue.

4.3.2 PM chemical composition analysis by aerosol mass spectrometer

Since the aerosol suspensions of particles were all using aqueous solutions with no inert particulate matter, the biological impacts of the exposures are expected to be based on the release of soluble components of particulates into the tissue, rather than on the particulate physical properties. Thus, we determined the soluble composition of the aqueous solutions using AMS. There was a large difference in the organic fraction between PM from the Salton Sea (5.9–6.6%), Pacific Ocean (12–20%) and the Alternaria (82%). Additionally, Alternaria PM had a notable fraction of NO3 (10%) compared to the others (<0.1%). Detectable levels of NH_4 (1.01%) were only measured for the Alternaria PM. There were also key differences between the "salty" PMs (Salton Sea and Pacific Ocean). The Salton Sea PM was lower in organic content than the Pacific Ocean PM. In contrast, the fraction of metal ions and other inorganics were higher in the Salton Sea PM than in the Pacific Ocean PM (Fig. 4-1c).

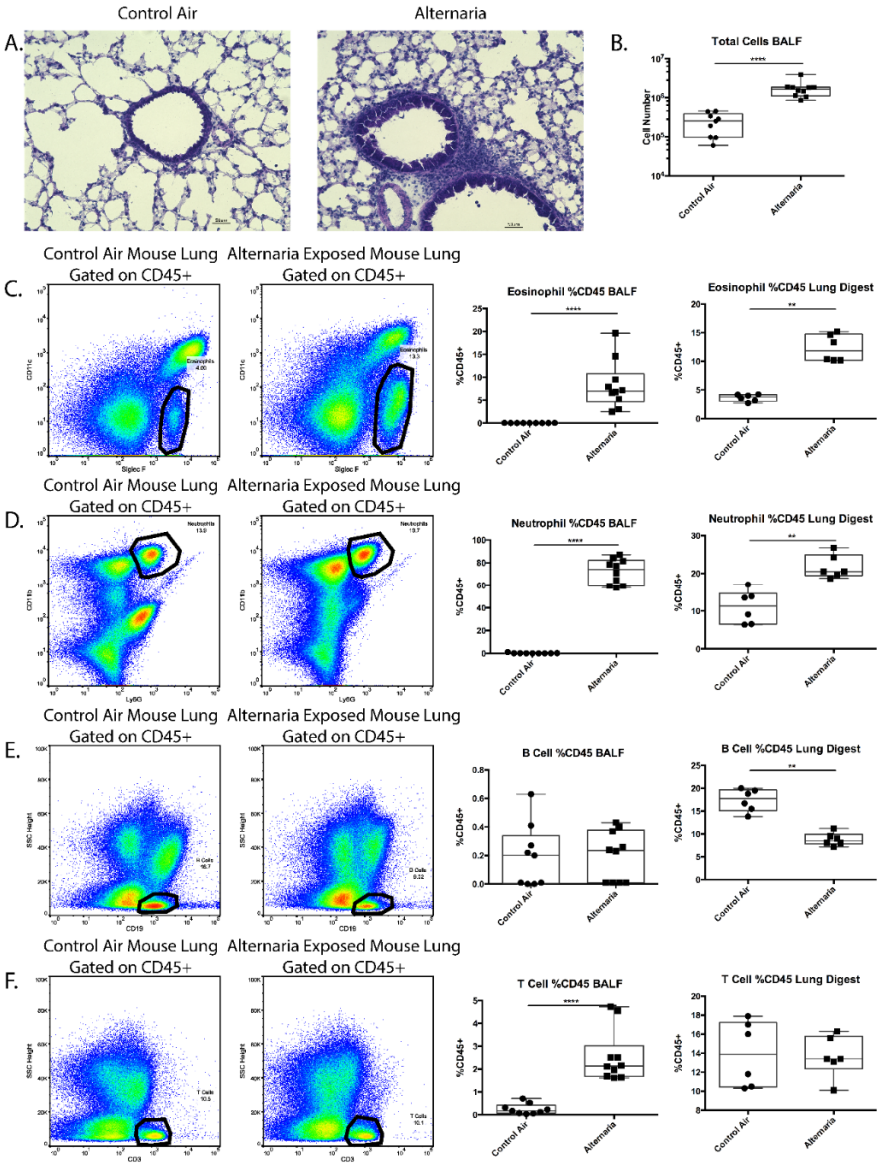

Figure 4-2 Inflammatory cell recruitment due to Alternaria aerosols. Mice were exposed to either filtered control air or aerosolized Alternaria filtrate for 7 days in dual environmental chambers. Following exposure, bronchoalveolar lavage fluid (BALF) was collected and the left lobe was digested and analyzed via flow cytometry. (A) Lungs inflated with a 1:1 OCT:PBS solution and frozen in OCT blocks were sectioned and stained with H&E. (*, Interstitial infiltrate). (B) Total cells in the BALF were counted via hemocytometer (Left, Control air, n = 9; Right, Alternaria, n = 10). (C–F) Cells were represented as a percentage of CD45+ cells in digested lungs or BALF. Representative dot plots for control air and Alternaria exposed are shown. Eosinophils are CD45+CD11c−SiglecF+ (Left diagram: Left, Control air BALF, n = 9; Right, Alternaria BALF, n = 10; Right diagram: Left, Control Air Lung, n = 6, Right, Alternaria Lung, n = 6). Neutrophils are CD45+CD11b+Ly6G+ (Left diagram: Left, Control air BALF, n = 9; Right, Alternaria BALF, n = 10; Right diagram: Left, Control air, n = 6, Right, Alternaria, n = 6). B cells are CD45+SSClowCD19+ (Left diagram: Left, Control air BALF, n = 9; Right, Alternaria BALF, n = 10; Right diagram: Left, Control air, n = 6, Right, Alternaria, n = 6). T cells are CD45+SSClowCD3+ (Left diagram: Left, Control air BALF, n = 9; Right diagram: Right, Alternaria BALF, n = 10; Left, Control air, n = 6, Right, Alternaria, n = 6). ** = p < 0.01; **** = p < 0.0001.

4.3.3 Alternaria elicited allergic immune cell recruitment to lungs

To assess whether Salton Sea exposure can trigger allergic asthma, it was important to establish reference characteristics of a canonical allergic lung inflammation. Thus, we exposed C57BL/6 J mice to Alternaria alternata and Alternaria tenuis filtrate mixture (hereafter referred to as "Alternaria") at a chamber mass concentration of approximately 1500 μg m^{-3} for 7 days. A group of mice were held in the exposure chamber, while a control group was simultaneously held in a parallel chamber that had only filtered air pumped into it. Following the exposure, BALF and lung tissues were assessed for inflammatory cell infiltration. H&E staining of the lung showed marked cellular infiltration around the airways compared to the controls (Fig. 4-2a), indicating an inflammatory response to the Alternaria. Additionally, there was a significant increase in the number of cells in the BALF (1.7 × 106 ± 2.7 × 105 vs. 2.5 × 105 ± 4.9 × 104 control, $p < 0.0001$; Fig. 4-2b) compared to the controls.

BALF cells were stained for analysis by flow cytometry to identify infiltrating inflammatory cells. The differential proportions of neutrophils (CD11b+, Ly6G+), eosinophils (CD11c−, Siglec F+), T cells (SSClow, CD3+), and B cells (SSClow, CD19+) were quantified as a proportion of CD45+ cells, with the remaining cells mainly being alveolar macrophages. Similar to our previous studies (Peng et al., 2018), the BALF of Alternaria exposed mice showed an expected increase in neutrophils (72.1 ± 11.1% vs. 0.2 ± 0.1% control, $p < 0.0001$; Fig. 4-2d) and eosinophils (8.3 ± 1.7% vs. ~0% control, $p < 0.0001$; Fig. 4-2c). T cells made up a higher, though small, percent of the BALF after

Alternaria exposure (2.5 ± 0.4% vs 0.2 ± 0.1% control, $p < 0.0001$; Fig. 4-2f). B cells were essentially undetectable in the BALF (0.2 ± 0.1% vs. 0.2 ± 0.1% control; Fig. 4-2e).

Infiltrating inflammatory cells may be limited to the interstitial compartment of the tissue, and so might not be detected among lung lavage cells. Differences in BALF versus tissue infiltrating cells may also reveal differences in the way inflammatory cells are recruited as well as differences in their impact on tissue remodeling, which has a critical impact on airway resistance. Thus, tissue infiltrating cells were also isolated by enzymatic digestion of lung tissues and stained for analysis by flow cytometry. Interestingly, we found that while there were some similarities in the types of cells detected, the proportions of different infiltrating cell types were notably different. For example, the proportion of neutrophils in Alternaria exposed lungs, while higher than in the control lungs (21.8 ± 1.3% vs. 11.1 ± 1.8% control, $p < 0.01$; Fig. 4-2d), was nonetheless smaller than the 70% + proportion of neutrophils in the BALF. In the case of eosinophils, there also were low numbers of cells detected in controls; however, Alternaria-exposed lung actually showed a higher proportion in the digested tissue (12.3 ± 1.0% vs. 3.6 ± 0.3% control $p < 0.01$; Fig. 4-2c) compared to ~8.3% in the BALF. These contrasting ratios of neutrophils and eosinophils in BALF versus digested tissue are consistent with the possibility that neutrophils may play a more important role in clearing microbes from alveolar and airway spaces, while eosinophils are more important in the interstitial spaces, where they may contribute to tissue remodeling.

Lymphocytes were also more easily detected in lung digests compared to BALF. T cells were higher in digested tissue (13.6 ± 0.9% vs. 13.9 ± 1.4% control) compared to BALF,

but the Alternaria exposed lungs showed no significant difference compared to controls (Fig. 4-2f); an expected increase in recruited CD4 T cells21 was likely diluted by the infiltrating granulocytes. The percentage of B cells was also higher in digests (8.8 ± 0.6% vs. 17.4 ± 1.0% control, $p < 0.01$) than in BALF, but the proportion of B cells detected in exposed lungs was decreased relative to controls, also possibly due to the increased proportion of granulocytes (Fig. 4-2e).

4.3.4 Response to Salton Sea and Pacific Ocean water

With the inflammatory response to Alternaria exposure as a reference, we exposed mice to filtered and aerosolized Salton Sea water. Exposures were performed using water samples collected at different times and sites at the Sea, but all exposures were performed at a similar mass concentration. Following the exposures, mice were analyzed in the same manner as the Alternaria exposure. In contrast to the picture in Alternaria exposed mice, the lungs from mice exposed to aerosolized Salton Sea water did not contain granulocyte recruitment in either the BALF or digested lung tissue. Moreover, H&E stained lung sections (Fig. 4-3a) showed no evidence for cellular recruitment after exposure to aerosolized Salton Sea water. Total BALF cell counts also showed no differences between exposure and control ($5.2 \times 10^5 \pm 1.6 \times 10^5$ vs. $3.8 \times 10^5 \pm 7.9 \times 10^4$ control; Fig. 4-3b). Flow cytometry analysis of digested lung tissue revealed minimal inflammatory cell recruitment: eosinophils (3.7 ± 0.6% vs. 2.4 ± 0.5% control; Fig. 4-3c), neutrophils (12.2 ± 1.2 vs. 15.3 ± 2.7% control; Fig. 4-3d), and T cells (10.7 ± 0.7% vs. 10.2 ± 0.8% control;

Fig. 4-3f) showed no significant differences. Interestingly, B cells in digested lung tissue were increased after exposure to the Salton Sea water (18.5 ± 1.5% vs. 12.3 ± 0.7% control, $p < 0.05$; Fig. 4-3e). All four cell types were essentially not present in the BALF (data not shown). To determine whether this response was due to unique characteristics of the Salton Sea spray particles or a general response to Sea spray, we exposed mice to aerosolized Pacific Ocean water, also collected at multiple dates. Communities living near the Pacific Ocean do not show the high asthma rates found near the Salton Sea, so any differences observed may provide clues to potential links between Salton Sea aerosols and asthma. Inflammatory cell recruitment from Salton Sea and Pacific Ocean exposures turned out to be very similar, as there was no difference in the BALF cell counts ($3.8 \times 10^5 \pm 7.6 \times 10^4$ vs $2.6 \times 10^5 + 3.3 \times 10^4$ control; Fig. 4-3b) nor increase in the percentage of tissue digest eosinophils (2.6 ± 0.3% vs. 2.8 ± 0.3% control; Fig. 4-3c), neutrophils (11.9 ± 2.7% vs. 16.8 ± 6.8% control; Fig. 4-3d), or T cells (15.5 ± 1.3% vs. 10.7 ± 1.4% control; Fig. 4-3f). Moreover, there was a similar significant increase in B cell percentage (21.1 ± 1.2% vs. 13.9 ± 1.9% control, $p < 0.05$; Fig. 4-3e). Once again, all four cell types were essentially absent in the BALF (data not shown).

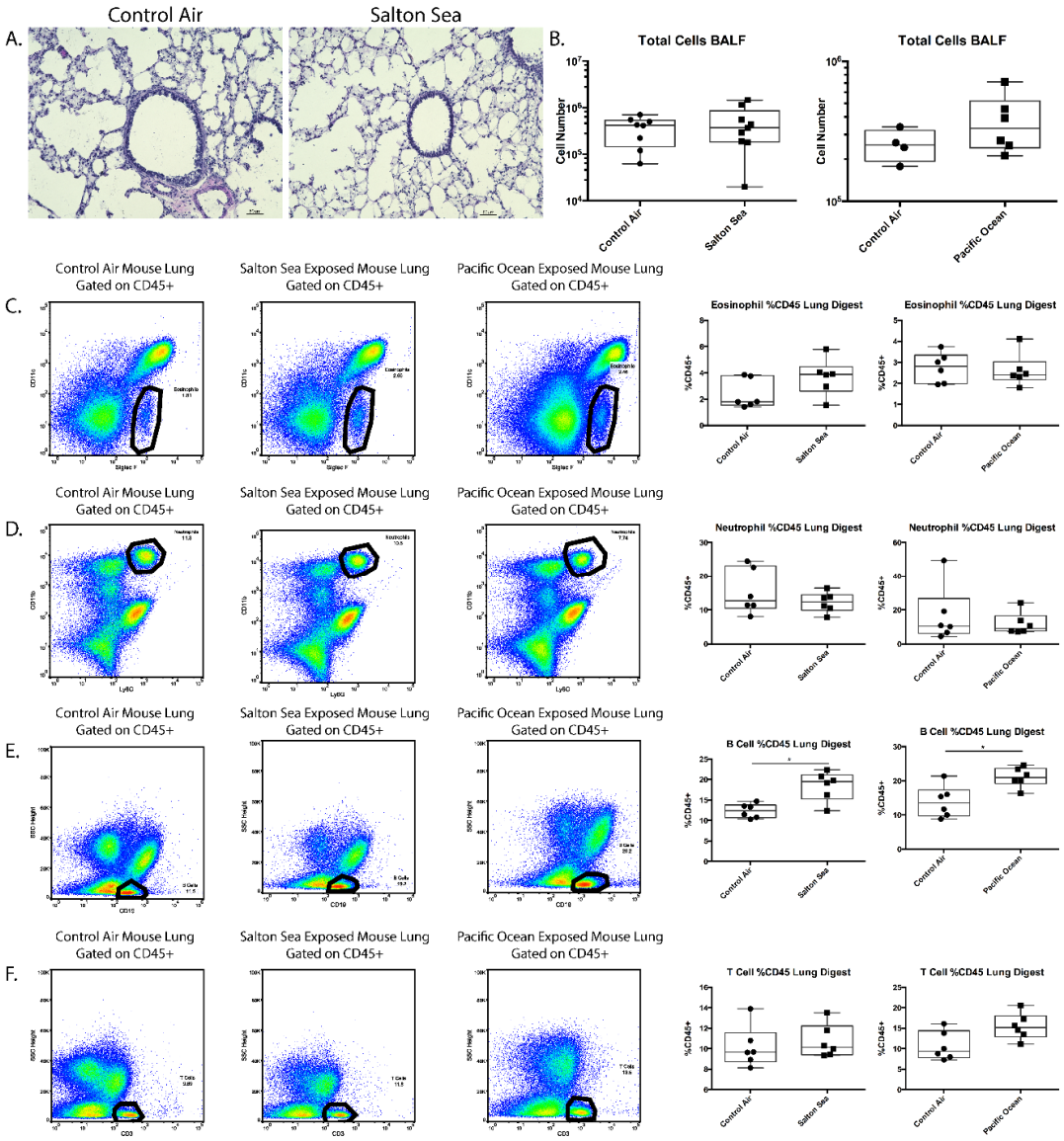

Figure 4-3 Inflammatory cell recruitment due to Salton Sea and Pacific Ocean aerosols. Mice were exposed to filtered control air, filtered and aerosolized Salton Sea water, or filtered and aerosolized Pacific Ocean water for 7 days. BALF was collected and tissue was digested for flow cytometry. (A) Lungs were inflated with a 1:1 OCT:PBS mixture and frozen, sectioned and stained with H&E. (B) Total cells in the BALF were counted via hemocytometer (Left diagram: Left, Control air, n = 8; Right, Salton Sea, n = 9; Right diagram: Left, Control Air, n = 4; Right, Pacific Ocean, n = 6). (C–F) Digested lung was stained and analyzed via flow cytometry. Cells populations are represented as the percentage of $CD45^+$ cells. Representative dot plots for the control air, Salton Sea exposed, and Pacific Ocean exposed mice are shown. Aerosolized Salton Sea and Pacific Ocean exposed mice are compared to their contemporaneous controls. Eosinophils are $CD45^+CD11c^-SiglecF^+$ (Left diagram: Left, Control air, n = 6; Right, Salton Sea, n = 6; Right Diagram: Left, Control air, n = 6; Right, Pacific Ocean, n = 6). Neutrophils are $CD45^+CD11b^+Ly6G^+$ (Left diagram: Left, Control air, n = 6; Right, Salton Sea, n = 6; Right Diagram: Left, Control air, n = 6; Right, Pacific Ocean, n = 6). B cells are $CD45^+SSC^{low}CD19^+$ (Left diagram: Left, Control air, n = 6; Right, Salton Sea, n = 6; Right Diagram: Left, Control air, n = 6; Right, Pacific Ocean, n = 6). T cells are $CD45^+SSC^{low}CD3^+$ (Left diagram: Left, Control air, n = 6; Right, Salton Sea, n = 6; Right Diagram: Left, Control air, n = 6; Right, Pacific Ocean, n = 6). * = $p < 0.05$.

4.3.5 Gene expression changes in the response to aerosols

While assays for cellular infiltrates and histological changes can reveal significant inflammatory responses to exposures, more subtle tissue responses were revealed from analyses of gene expression profiles. In these studies, we focused on a subset of immune-associated genes assayed using a panel of short sequence tag probes (NanoString). This method quantifies expressed genes by direct counting of hybridized tagged gene probes and includes a set of general "housekeeping gene" probes. As a set, this approach allowed broad internal normalization of the assayed gene expression profiles, which in turn enabled direct comparisons of different RNA profiles from different samples and studies. Principal Component Analysis (PCA) of gene expression profiles collapses the complex gene expression data sets, and helps provide overall comparisons among individual mice in different treatment groups. Our reference allergic inflammatory response to Alternaria exposure illustrates a reproducible and characteristic gene expression pattern, as seen by the distance between centroids from the control air group to the Alternaria group ($d = 19.84$) in this PCA ordination; we observed tight clustering within the control air group and Alternaria groups and clear differentiation between the groups in the PCA, despite multiple replicates (Fig. 4-4a). We identified 213 differentially regulated genes (FDR < 0.10) of which 166 were significantly upregulated vs 47 which were significantly downregulated (Fig. 4-4b). These genes are diverse in function, but the strongest change in regulation falls into immune defense responses and chemokine production, consistent with the observed recruitment of inflammatory cells into the lung. Among the top 20 regulated genes are Ig receptors (Fcgr2b, Pigr, Fcgr3), chemokines (Cxcl3, Ccl9, Ccl8, Ccl3 Ccl22), immune

regulatory genes (Tgfbi, Lilrb4, IL33, Ctss, Ptafr, Ctsc) and innate immune genes (Cfb, Muc1). By contrast, analysis of gene expression profiles from exposures to aerosolized Salton Sea water revealed a distinctively different pattern (Fig. 4-5a). The PCA shows an overall distinction between control air and Salton Sea exposed groups; however, the extent of these orthogonal axes did not explain as much of the variance, nor did they illustrate as great of a separation as was detected for the Alternaria exposures. Euclidean distance between centroids of control air and Salton Sea exposed groups (d = 3.08) within the PCA ordination was shorter than was found in the PCA for the Alternaria exposures.

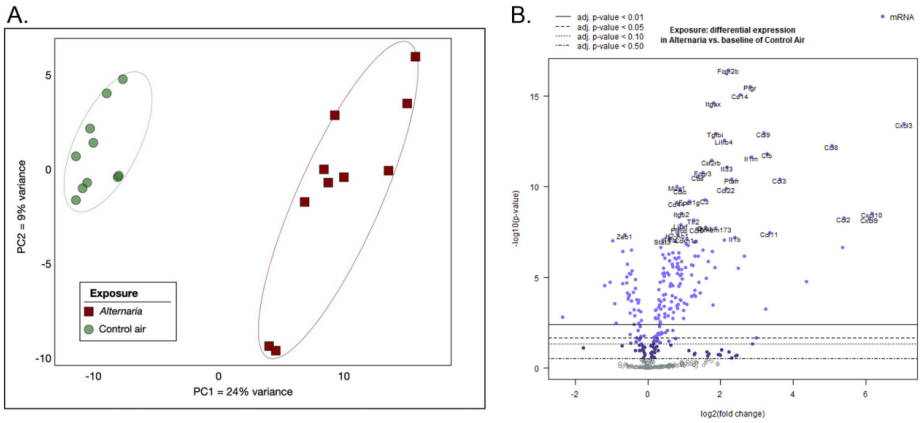

Figure 4-4 Gene expression changes due to Alternaria aerosol exposure. After a 7-day exposure to either filtered control air (n = 10) or Alternaria filtrate (n = 10), lung RNAs were analyzed for gene expression using a defined immunology gene panel (NanoString); (A) PCA of the gene expression data with red squares representing mouse lung immune gene expression profiles from individual animals exposed to aerosolized Alternaria sp., as compared to green circles, which are from mouse samples exposed to control air. (B) Volcano plot depicting the differential expression profile of the Alternaria exposed mice compared to a baseline of control air. The X-axis depicts the log2 fold change while the Y-axis depicted the -log10 (Benjamini-Hochberg adjusted p-value). The 40 most significant gene by Benjamini-Hochberg adjusted p-value are labeled.

This exposure triggered significant gene expression changes, with 151 differentially expressed genes (Fig. 4-5b). Of these, 146 genes were significantly upregulated while only 5 were significantly downregulated (FDR < 0.10). The regulated genes were primarily associated with phosphorylation pathways (Jak1, Jak2, Jak3, Stat5b, Tnfrsf14), T cell activation (Ifnar1, Ifngr1), and NF-KB signaling (Ikbkb). Additionally, a preference

toward MHC I/Th1 response predominates (Ifnar1, Ifngr1, Tap1), although there were some Th2-related receptors upregulated (Il6ra). It should be noted that the magnitude of gene expression changes, while statistically significant, were relatively small, with the vast majority (134 of the 146 upregulated genes) showing less than 0.5 Log2 fold change. Despite the lower magnitude changes, the regulated genes were consistent across replicate exposures and multiple Salton Sea samples, illustrated by the clustering of the Salton Sea data points relative to control data in the PCA.

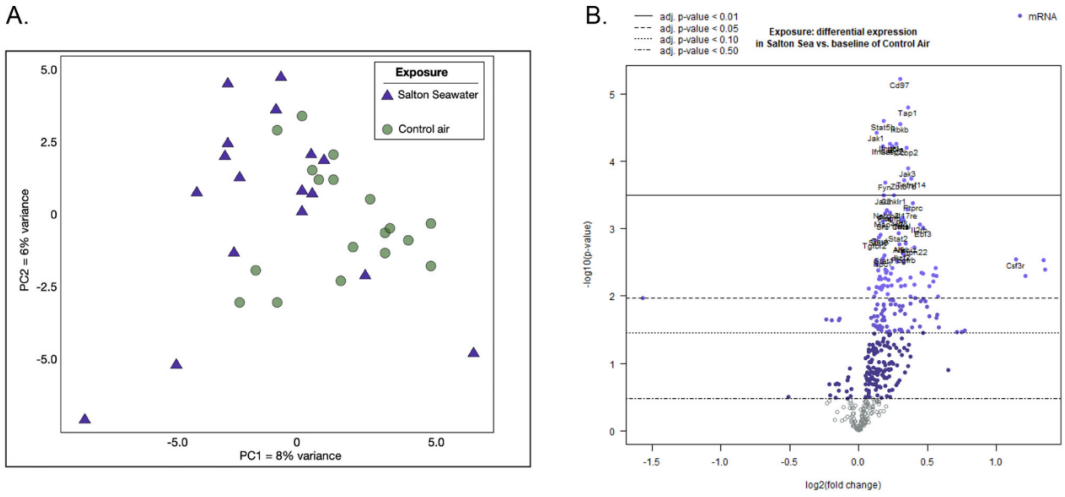

Figure 4-5 Gene expression changes due to Salton Sea aerosol exposure. After a 7-day exposure to either filtered control air (n = 18) or aerosolized Salton Sea water (n = 17), lung RNAs were analyzed for gene expression using a defined immunology gene panel (NanoString). (A) PCA of the gene expression data with purple triangles representing mouse lung immune gene expression profiles from individual animals exposed to aerosolized Salton Sea water, as compared to green circles, which are from mouse samples exposed to control air. (B) Volcano plot depicting the differential expression profile of the aerosolized Salton Sea exposed mice compared to a baseline of control air. The X-axis depicts the log2 fold change while the Yaxis depicted the -log10 (Benjamini-Hochberg adjusted p-value). The 40 most significant gene by Benjamini-Hochberg (BH) adjusted p-value are labeled.

As noted above, both Salton Sea and Pacific Ocean exposures induced some recruitment of B cells into lung tissue. Interestingly, this similarity was not seen in the gene expression profiles; in replicate studies with different Pacific Ocean samples, aerosolized Pacific Ocean exposed mice showed no significant changes in gene expression compared to

controls (Fig. 4-8). It is likely that if there were any induced genes related to B cell recruitment, they were not represented in the probe set used. More importantly however, these comparisons suggest that Salton Sea water exposures had a characteristic biological effect, unrelated to any general effect of exposure to sea water.

Our analysis of gene regulation in response to Alternaria versus Salton Sea exposures showed that each induced a reproducible and characteristic set of gene expression changes, with tight clustering within the groups and little intergroup overlap. Additionally, both Salton Sea and Alternaria produced responses distinct from the Pacific Ocean exposed mice (Fig. 4-6a). It is especially notable, however, that the Alternaria and Salton Sea exposures each induced strikingly different sets of genes (Fig. 4-6b; Pacific Ocean excluded due to a lack of differentially expressed genes). Of the 166 upregulated genes in Alternaria exposed mice and the 146 in the Salton Sea exposed mice, only 55 are upregulated in both. Even more notable is that of the 47 downregulated genes in the Alternaria exposed mice and 5 downregulated genes in the Salton Sea exposed, only 1 was downregulated in both. Additionally, 13 genes which were upregulated in Salton Sea exposed mice were downregulated in Alternaria while 2 genes which were upregulated in Alternaria exposed mice were downregulated in mice exposed to aerosolized Salton Sea. Thus, while it appeared that both types of exposures regulated genes associated with at least some aspect of innate and adaptive immunity, their overall impacts were on rather different components of the immune or inflammatory response.

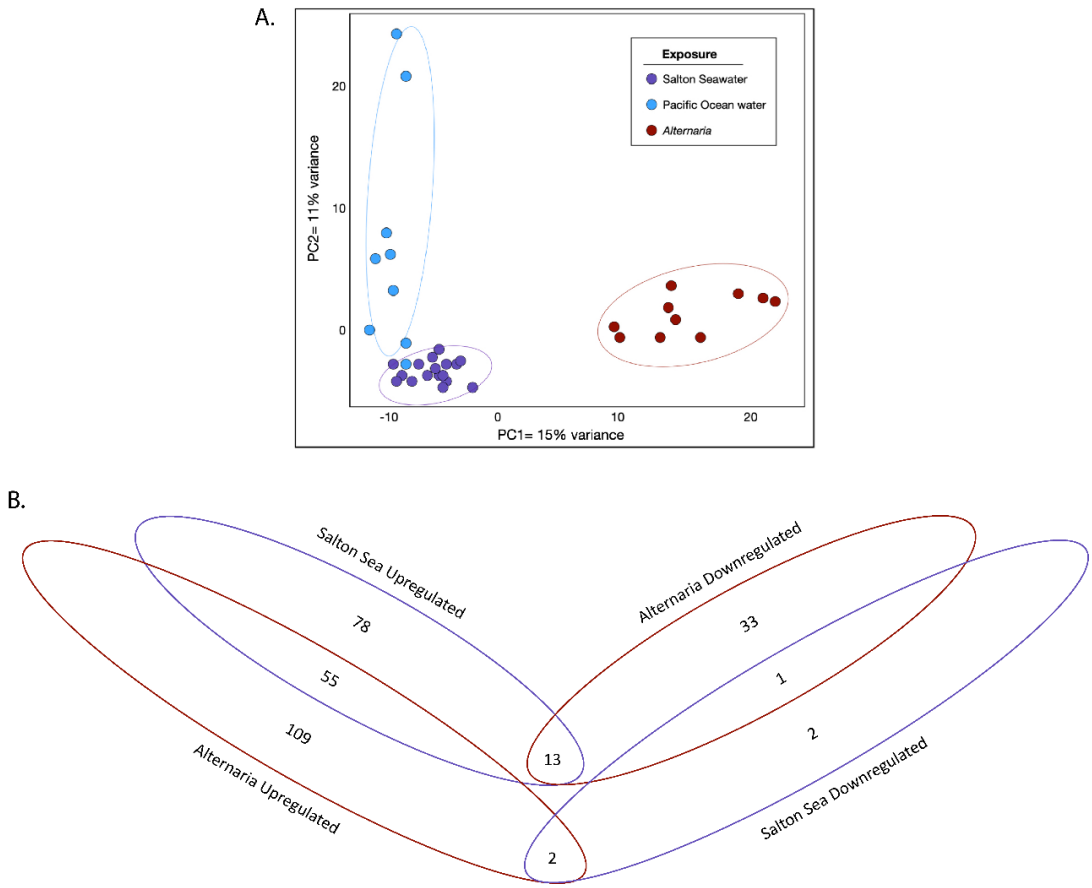

Figure 4-6 Comparisons between Alternaria, Salton Sea and Pacific Ocean exposures. Mice were exposed to either control air, Alternaria, or aerosolized Salton Sea for 7-days before lung tissue was collected. Extracted RNA was analyzed using a Mouse Immunology Panel (NanoString). (A) PCAs were generated using the "prcomp" function in R (version 4.0.3), to compare Pacific Ocean (blue stars), Salton Sea (purple triangles) and Alternaria (red squares) exposures, and visualized PCA as in Methods. Comparisons are made between Alternaria exposed mice (n = 10) and their contemporaneous controls (n = 10) or aerosolized Salton Sea exposed mice (n = 17) and their contemporaneous controls (n = 18). 213 genes were differentially regulated in the Alternaria comparison (FDR < 0.10), of which 166 were upregulated and 47 were downregulated. 151 genes were differentially regulated in the Salton Sea comparison (FDR < 0.10), of which 146 were upregulated and 5 were downregulated. 55 genes were upregulated in both comparisons, 1 gene was downregulated in both comparisons, 13 were upregulated in the Salton Sea comparison but downregulated in the Alternaria comparison while 2 were upregulated in the Alternaria comparison but downregulated in the Salton Sea comparison. 78 genes were uniquely upregulated, and 2 genes were uniquely downregulated in the Salton Sea comparison while 109 genes were uniquely upregulated and 33 were uniquely downregulated in the Alternaria comparison.

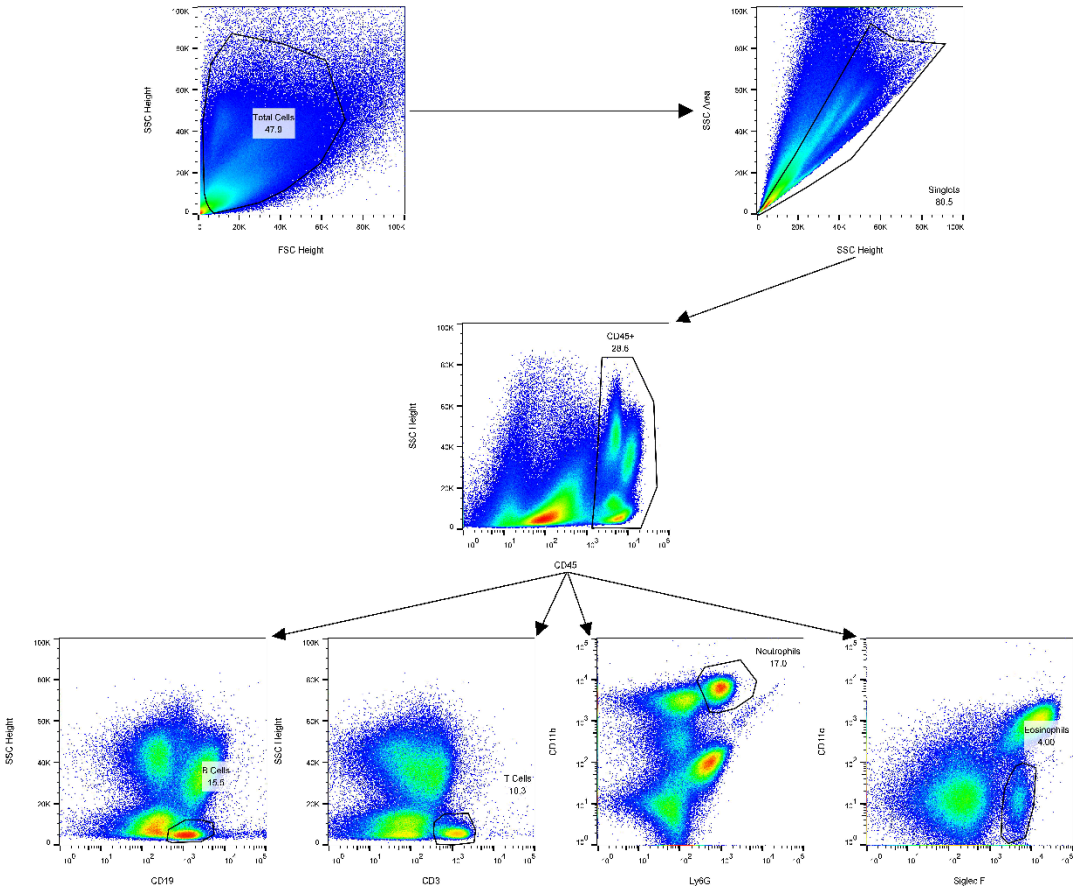

Figure 4-7 Gating strategy for flow cytometry. Lungs of mice were collected and digested after 7 days of a given exposure condition. The digested lungs were treated with BD FC Block in order to prevent nonspecific binding. Afterwards, the digested lung was stained with anti-CD45^{+} FITC, anti-CD19 PE-Cy5, anti-CD3 Alexa Fluor 700, anti-CD11b BV421, anti-Ly6G BV510 or anti-SiglecF APC. The gating strategy used to identify different immune cell subpopulations are shown above. First, debris is gated out using SSC and FSC height. Following that, doublets are gated out using SSC area and SSC height. Then CD45^{+} cells are selected. These CD45^{+} cells are then subdivided into B cells (SSC^{low}, CD19^{+}), T cells (SSC^{low}, CD3^{+}), neutrophils (CD11b^{+}, Ly6G^{+}) and eosinophils (CD11c^{-}, Siglec F^{+}).

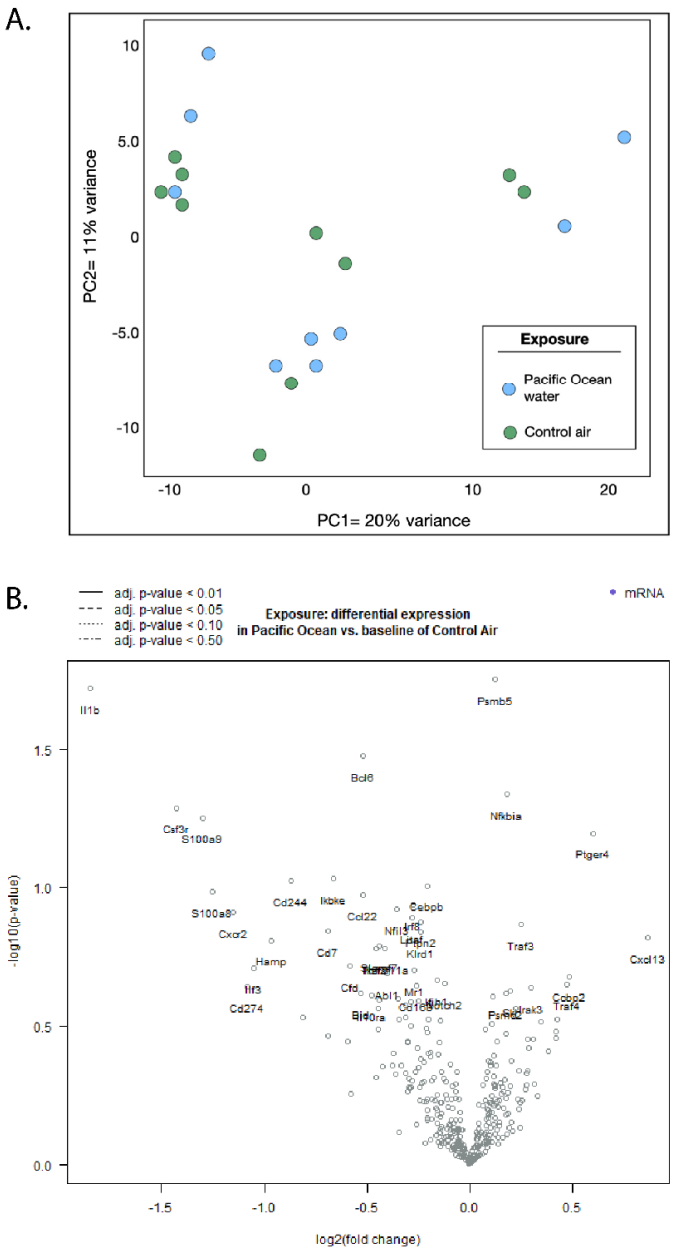

Figure 4-8 Gene expression changes due to Pacific Ocean aerosols. After a 7-day exposure to either filtered control air (n=10) or aerosolized Pacific Ocean exposed (n=10), lung RNAs were analyzed for gene expression using a defined immunology gene panel (NanoString). (A) PCA of the gene expression data with blue stars representing mouse lung immune gene expression profiles from individual animals exposed to aerosolized Pacific Ocean, as compared to green circles, which are from mouse samples exposed to control air. PCAs were generated as described in Methods. (B) Volcano plot depicting the differential expression profile of the aerosolized Pacific Ocean exposed mice compared to a baseline of control air. The X-axis depicts the log2 fold change while the Y-axis depicted the -log10 (Benjamini-Hochberg adjusted p-value). The 40 most significant gene by Benjamini-Hochberg adjusted p-value are labeled.

4.4 Discussion

The studies reported here were principally aimed at determining whether the aqueous components (which may include microbial components and toxins) in Salton Sea water might have effects on pulmonary tissues in response to chronic delivery into the lung as aerosolized particles. We found that aerosolized Salton Sea water was able to induce a distinct inflammatory gene expression profile despite a lack of cell recruitment to the BALF as well as neutrophil and eosinophil recruitment to the lung tissue. It is important to note that these studies do not test the biological effects of actual dust generated at the Salton Sea exposed playa; these effects are the subject of ongoing studies and will be reported separately. Since the impact of dust exposure among residents in the region is dependent on a variety of factors, including prevailing wind patterns, dust events, and proximity to the Salton Sea, such studies will need to take these other additional factors into account.

To investigate the effect that Salton Sea spray may have on the communities surrounding the Sea, we exposed C57BL/6 mice to approximately 1500 μg m^{-3} of aerosolized Salton Sea for 7 days. While this is meant to simulate a chronic exposure condition, there are still some limitations associated with our model. Residents surrounding the Salton Sea are exposed to variable levels of aerosols over a period of years, unlike the consistent 7-day exposure in our study. As perfectly matching both the exposure time and aerosol concentration the residents are exposed to is impractical, we focused on a reasonable timeframe and aerosol concentration that showed demonstrable results. As this timeframe and concentration was sufficient to reliably induce large changes in Alternaria exposed

mice and gene expression changes in Salton Sea exposed mice while the Pacific Ocean exposed mice showed no change, we believe our methodology is capable of providing real insights into the health effects of these aerosols. While direct measurement of airway hyperreactivity was beyond the scope of this study, our initial results call for future studies into this topic.

For this study, we used aerosols generated from filtered aqueous solutions. While this excluded the potential effects of larger inert dust particles, it allowed us to specifically focus on the effects of the dissolved components in the water. Separating the effects of the dissolved aqueous components and inert dust particles is critical as inert dust particles can have their own biological effects, including triggering of airway irritant receptors (Sellick and Widdicombe, 1971). Additionally, larger dust particles (e.g., 1 μm or larger) may affect the delivery of soluble components carried on their surface, since they would not be as capable of penetrating deep into alveolar spaces. Exclusion of these larger particles was also important for generating a consistent PM (all PM in the study had a mobility diameter well under 1 μm); thus, particle size was unlikely to be a limiting factor for distribution. Effects due directly to minor differences in particle size are most likely negligible, as exposure to Pacific Ocean water failed to induce gene expression changes, indicating that the specific composition of the aerosol is the primary driving agent for gene expression changes and cell recruitment. Our AMS breakdown was unable to pinpoint a broad category for reactive agents, as there was no consistent ratio between the composition and the effects. Thus, future studies should focus on specific components that may be present in the Salton Sea water. As we found some aspects of the NFKB pathway upregulated

(Ikbkb, RelA), care should be taken to investigate sources of reactive oxygen species (ROS). In particular, pesticides (LeBlanc and Kuivila, 2008) and heavy metal ions (Frie et al., 2019; D'Evelyn et al., 2021), both of which have been detected in the Salton Sea, should be investigated, as they are known to induce ROS (Abdollahi et al., 2004; Leikauf et al., 2020).

The studies reported here are only among the first steps in studies identifying the potential aerosols contributing to lung disease in residents near the Salton Sea. The sea spray aerosols produced at the Salton Sea surface are certainly not the only contributor to inhaled aerosols and the proportions of other components in the inhaled aerosols may vary widely depending on the aggregation of sea spray among other ambient dust particles generated at the playa or more distant sources. Indeed, these studies should not be interpreted to suggest that Salton Sea water aerosols are the only source of potential aerosol toxins in the region. Also, actual exposures well depend on an individual's geographic position relative to the Salton Sea, seasonal winds, and other factors.

The main observation reported here is that soluble components of Salton Sea water are able to induce a unique pattern of gene expression changes in chronically exposed lungs, and that this pattern is strikingly distinct from the characteristic allergic inflammation induced by the common household fungal allergens in Alternaria filtrate. In the context of the observed high incidence of asthma in the Salton Sea region, our findings suggest that the Salton Sea water soluble components by themselves appear to induce significant lung responses, but they are clearly distinct from the characteristic allergic inflammatory responses typified by Alternaria exposures. However, the distinctive effect of Salton Sea

exposures does not entirely rule out potential impacts on asthma. A number of receptors were significantly upregulated, including Il6r, CD97, Ifngr1 and Ifnar1. IL-6 is associated with IL-4 production, which is critical for Th2 differentiation (Rincon and Irvin, 2012). The soluble form of Il6r has also been associated with asthma severity (Peters et al., 2017). CD97 is a known costimulatory factor on CD4+ T cells (Capasso et al., 2006). In contrast to the previous receptors, Ifngr1 and Ifnar1 are associated with Th1 response. However, Th1-polarization has been linked to nonallergic asthma (Zoratti et al., 2014). Additionally, our previous studies showed that Th1 inflammatory responses could not only co-exist with allergic Th2 inflammatory responses, they could show additive effects (Li et al., 1998). Salton Sea exposures also induced a number of genes associated with signaling pathways, such Jak1, Jak2 and Jak3. As these signaling pathways are known to have critical roles in pulmonary eosinophilia, airway hyperreactivity and mucus hypersecretion (Hoshino et al., 2004), upregulation of these components could potentially provide additive or synergistic effects in the presence of other triggers, including environmental or household allergens.

4.5 Conclusions

Our results suggest two main points. First, Salton Sea exposure is unable to generate an inflammatory response similar to a potent allergen, as characterized in our study by Alternaria. However, aerosolized Salton Sea was able to trigger an inflammatory response distinct from a potent allergen, unlike aerosolized Pacific Ocean water, which did not trigger an inflammatory response. Thus, while Salton Sea spray may not be sufficient to generate asthma alone, it could play a key role in the progression to asthma or other

inflammatory diseases. Future studies should explore the role of this inflammatory response in the context of the full range of aerosols to which the communities surrounding the Salton Sea are exposed.

4.6 Reference

Abdollahi, M., Ranjbar, A., Shadnia, S., Nikfar, S., Rezaie, A., 2004. Pesticides and oxidative stress: a review. Med. Sci. Monit. 10 (6), 141–148.

Bernstein, J.A., Ghosh, D., Levin, L.S., Zheng, S., Carmichael, W., Lummus, Z., Bernstein, I.L., 2011. Cyanobacteria: an unrecognized ubiquitous sensitizing allergen? Allergy Asthma Proc. 32 (2), 106–110. https://doi.org/10.2500/aap.2011.32.3434.

Bousquet, J., Jeffery, P.K., Busse, W.W., Johnson, M., Vignola, A.M., 2000 May. Asthma. From bronchoconstriction to airways inflammation and remodeling. Am. J. Respir. Crit. Care Med. 161 (5), 1720–1745. https://doi.org/10.1164/ajrccm.161.5.9903102.

Bureau of Reclamation, 2020. Salton Sea. Retrieved March 02, 2021, from. https://www.usbr.gov/lc/region/programs/saltonsea.html.

Bush, R.K., Prochnau, J.J., 2004. Alternaria-induced asthma. J. Allergy Clin. Immunol. 113 (2), 227–234. https://doi.org/10.1016/j.jaci.2003.11.023.

California Environmental Protection Agency, Office of Environmental Health Hazard Assessment, 2018, June 25. CalEnviroScreen 3.0. Retrieved from. https://oehha.ca.gov/calenviroscreen/report/calenviroscreen-30.

Capasso, M., Durrant, L.G., Stacey, M., Gordon, S., Ramage, J., Spendlove, I., 2006. Costimulation via CD55 on human CD4 + T cells mediated by CD97. J. Immunol. 177 (2), 1070–1077. https://doi.org/10.4049/jimmunol.177.2.1070.

Carmichael, W.W., Li, R.H., 2006. Cyanobacteria toxins in the Salton Sea. Saline Syst. 2, 5. https://doi.org/10.1186/1746-1448-2-5.

DeCarlo, P.F., Kimmel, J.R., Trimborn, A., Northway, M.J., Jayne, J.T., Aiken, A.C., Gonin, M., Fuhrer, K., Horvath, T., Docherty, K.S.,Worsnop, D.R., Jimenez, J.L., 2006. Field-deployable, high-resolution, time-of-flight aerosol mass spectrometer. Anal. Chem. 78 (24), 8281–8289. https://doi.org/10.1021/ac061249n.

D'Evelyn, S.M., Vogel, C.F.A., Bein, K.J., Lara, B., Laing, E.A., Abarca, R.A., Zhang, Q., Li, L., Li, J., Nguyen, T.B., Pinkerton, K.E., 2021. Differential inflammatory potential of particulate matter (PM) size fractions from imperial valley, CA. Atmos. Environ. 244 (January 2020). https://doi.org/10.1016/j.atmosenv.2020.117992.

Environmental Protection Agency, 2012. Nonattainment Areas for the Criteria Pollutants. Retrieved from. https://www.arcgis.com/apps/MapSeries/index.html?appid=8fbf9bde204944eeb422eb3ae9fde765.

Evan, A.T., 2019. Downslope winds and dust storms in the salton basin. Mon. Weather Rev. 147 (7), 2387–2402. https://doi.org/10.1175/MWR-D-18-0357.1.

Farzan, S.F., Razafy,M., Eckel, S.P., Olmedo, L., Bejarano, E., Johnston, J.E., 2019. Assessment of respiratory health symptoms and asthma in children near a drying saline lake. Int. J. Environ. Res. Public Health 16 (20). https://doi.org/10.3390/ijerph16203828.

Fleming, L.E., Kirkpatrick, B., Backer, L.C., Bean, J.A., Wanner, A., Reich, A., Zaias, J., Cheng, Y.S., Pierce, R., Naar, J., Abraham,W.M., Baden, D.G., 2007. Aerosolized red-tide toxins (brevetoxins) and asthma. Chest 131 (1), 187–194. https://doi.org/10.1378/chest.06-1830.

Frie, A.L., Garrison, A.C., Schaefer, M.V., Bates, S.M., Botthoff, J., Maltz, M., Ying, S.C., Lyons, T., Allen, M.F., Aronson, E., Bahreini, R., 2019. Dust sources in the Salton Sea Basin: a clear case of an anthropogenically impacted dust budget. Environ. Sci. Technol. 53 (16), 9378–9388. https://doi.org/10.1021/acs.est.9b02137.

Guarnieri, M., Balmes, J.R., 2014. Outdoor air pollution and asthma. Lancet 383 (9928), 1581–1592. https://doi.org/10.1016/S0140-6736(14)60617-6.

Hoshino, A., Tsuji, T., Matsuzaki, J., Jinushi, T., Ashino, S., Teramura, T., Chamoto, K., Tanaka, Y., Asakura, Y., Sakurai, T., Mita, Y., Takaoka, A., Nakaike, S., Takeshima, T., Ikeda, H., Nishimura, T., 2004. STAT6-mediated signaling in Th2-dependent allergic asthma: critical role for the development of eosinophilia, airway hyper-responsiveness and mucus hypersecretion, distinct from its role in Th2 differentiation. Int. Immunol. 16 (10), 1497–1505. https://doi.org/10.1093/intimm/dxh151.

LeBlanc, L.A., Kuivila, K.M., 2008. Occurrence, distribution and transport of pesticides into the Salton Sea Basin, California, 2001-2002. Hydrobiologia 604 (1), 151–172. https:// doi.org/10.1007/s10750-008-9316 1.

Leikauf, G.D., Kim, S.H., Jang, A.S., 2020. Mechanisms of ultrafine particle-induced respiratory health effects. Exp. Mol. Med. 52 (3), 329–337. https://doi.org/10.1038/s12276-020-0394-0.

Li, L., Xia, Y., Nguyen, A., Feng, L., Lo, D., 1998. Th2-induced eotaxin expression and eosinophilia coexist with Th1 responses at the effector stage of lung inflammation.

J. Immunol. (Baltimore, Md. : 1950) 161 (6), 3128–3135. http://www.ncbi.nlm.nih.gov/pubmed/9743380.

Li, X., Xu, L., Zhou, W., Zhao, Q., Wang, Y., 2016. Chronic exposure to microcystin-LR affected mitochondrial DNA maintenance and caused pathological changes of lung

tissue in mice. Environ. Pollut. 210, 48–56. https://doi.org/10.1016/j.envpol.2015.12.001.

Löndahl, Jakob, Massling, Andreas, Pagels, Joakim, Swietlicki, Erik, Vaclavik, Elvira, Loft, Steffen, 2007. Size-resolved respiratory-tract deposition of fine and ultrafine hydrophobic and hygroscopic aerosol particles during rest and exercise. Inhal. Toxicol. 19 (2), 109–116. https://doi.org/10.1080/08958370601051677.

Oksanen, O., Blanchet, F.G., Kindt, R., et al., 2016. Vegan: Community Ecology Package. R Package Version 2.3-5. http://CRAN.R-project.org/package=vegan.

Peng, X.,Madany, A.M., Jang, J.C., Valdez, J.M., Rivas, Z., Burr, A.C., Grinberg, Y.Y., Nordgren, T.M., Nair, M.G., Cocker, D., Carson, M.J., Lo, D.D., 2018. Continuous inhalation exposure to fungal allergen particulates induces lung inflammation while reducing innate immune molecule expression in the brainstem. ASN Neuro 10, 175909141878230. https://doi.org/10.1177/1759091418782304.

Peng, X., Maltz, M.R., Botthoff, J.K., Aronson, E.L., Nordgren, T.M., Lo, D.D., Cocker, D.R., 2019. Establishment and characterization of a multi-purpose large animal exposure chamber for investigating health effects. Rev. Sci. Instrum. 90 (3), 1–7. https://doi.org/10.1063/1.5042097.

Peters, M.C., Mcgrath, K.W., Hawkins, G.A., Ph, D., Hastie, T., Ph, D., Levy, B.D., Israel, E., Phillips, B.R., Mauger, T., Ph, D., Comhair, S.A., Ph, D., Erzurum, S.C., Johansson, M.W., Wenzel, S.E., Woodruff, P.G., Bleecker, E.R., 2017. Plasma IL6 levels, metabolic dysfunction, and asthma severity: a cross-sectional analysis of two cohorts. Lancet Respir. Med. 4 (7), 574–584. https://doi.org/10.1016/S2213-2600(16)30048-0. Plasma.

Pielou, E.C., 1984. The Interpretation of Ecological Data: A Primer on Classification and Ordination. J. Wiley and Sons, New York.

R Core Team, 2017. R: A Language and Environment for Statistical Computing. R Foundation for Statistical Computing, Vienna, Austria https://www.R-project.org/.

R Core Team, 2020. R: A Language and Environment for Statistical Computing. R Foundation for Statistical Computing, Vienna, Austria https://www.R-project.org/.

Rincon, M., Irvin, C.G., 2012. Role of IL-6 in asthma and other inflammatory pulmonary diseases. Int. J. Biol. Sci. 8 (9), 1281–1290. https://doi.org/10.7150/ijbs.4874.

Salo, P.M., Arbes, S.J., Sever, M., Jaramillo, R., Cohn, R.D., London, S.J., Zeldin, D.C., 2006. Exposure to Alternaria alternata in US homes is associated with asthma symptoms. J. Allergy Clin. Immunol. 118 (4), 892–898. https://doi.org/10.1016/j.jaci.2006.07.037.

Sellick, H., Widdicombe, J.G., 1971. Stimulation of lung irritant receptors by cigarette smoke, carbon dust, and histamine aerosol. J. Appl. Physiol. 31 (1), 15–19. https://doi.org/10.1152/jappl.1971.31.1.15.

Shaffo, F.C., Grodzki, A.C., Fryer, A.D., Lein, P.J., 2018. Mechanisms of organophosphorus pesticide toxicity in the context of airway hyperreactivity and asthma. Am. J. Physiol. Lung Cell. Mol. Physiol. 315 (4), L485–L501. https://doi.org/10.1152/ajplung.00211.2018.

Sinclair, R., Russell, C., Kray, G., Vesper, S., 2018. Asthma risk associated with indoor mold contamination in hispanic communities in Eastern Coachella Valley, California. J. Environ. Public Health 2018. https://doi.org/10.1155/2018/9350370.

Wang, C., Gu, S., Yin, X., Yuan, M., Xiang, Z., Li, Z., Cao, H., Meng, X., Hu, K., Han, X., 2016. The toxic effects of microcystin-LR on mouse lungs and alveolar type II epithelial cells. Toxicon 115, 81–88. https://doi.org/10.1016/j.toxicon.2016.03.007.

Wark, P.A., Gibson, P.G., 2006 Oct. Asthma exacerbations. 3: pathogenesis. Thorax 61 (10), 909–915. https://doi.org/10.1136/thx.2005.045187.

Wickham, H., 2009. ggplot2: Elegant Graphics for Data Analysis. Springer-Verlag, New York, NY, USA.

Xu, E.G., Bui, C., Lamerdin, C., Schlenk, D., 2016. Spatial and temporal assessment of environmental contaminants in water, sediments and fish of the Salton Sea and its two primary tributaries, California, USA, from 2002 to 2012. Sci. Total Environ. 559, 130–140. https://doi.org/10.1016/j.scitotenv.2016.03.144.

Zaias, J., Fleming, L.E., Baden, D.G., Abraham, W.M., 2011. Repeated exposure to aerosolized brevetoxin-3 induces prolonged airway hyperresponsiveness and lung inflammation in sheep. Inhal. Toxicol. 23 (4), 205–211. https://doi.org/10.3109/08958378.2011.558936.

Zhou, C., Huang, J.C., Liu, F., He, S., Zhou, W., 2017. Effects of selenite on Microcystis aeruginosa: growth, microcystin production and its relationship to toxicity under hypersalinity and copper sulfate stresses. Environ. Pollut. 223, 535–544. https://doi.org/10.1016/j.envpol.2017.01.056.

Zoratti, E., Havstad, S., Wegienka, G., Nicholas, C., Bobbitt, K.R., Woodcroft, K.J., Ownby, D.R., Johnson, C.C., 2014. Differentiating asthma phenotypes in young adults through polyclonal cytokine profiles. Ann. Allergy Asthma Immunol. 113 (1), 25–30. https:// doi.org/10.1016/j.anai.2014.04.013.

Chapter 5 : Conclusion and Recommendations for Future Work

In chapter 2, we illustrated that RO_2 chemistry can explain the SOA formation trends with varying experimental conditions. The [HC]/[NO_x] ratio is a useful indicator of what major RO_2 reaction pathway can be but cannot completely represent the RO_2 chemistry. This is due to the varying ratios of RO_2+NO pathway to total RO_2 oxidation pathways in the traditional chamber study with one-time injection of NO_x before the irradiation. We were able to propose a hypothesis that at intermediate NO radical levels, the RO2+NO pathway owns fast reaction rate and can form HOMs as the end products. However, when NO radical mixing ratio is high that causes a high NO/HO_2 ratio, the end products formed with lack of HO_2 can have relatively high vapor pressure and thus lead to a low SOA mass yield. For future works, although the trends are supposed to retain since the trigger moments of SOA formation (the duration from lights on to measurable amount of SOA scanned) are similar with/without NO_x and the total number concentrations were similar and both relatively low (most maximum N <15,000 cm^{-3} with one at ~22,000cm^{-3}), the inconsideration of coagulation effects in the data processing still affected final SOA mass yield reported and asks for data reprocessing to properly evaluate the data. Future work can try investigating the reason for why oxidation products from camphene tended to form particles at significantly large size of up to 900nm in an 8-hour experiments. A series of

camphene experiments with constant branching ratio of RO_2+NO pathway is recommended to be performed in the new UCR fixed-volume chamber with continuous injection of NO under instructions from SAPRC simulations.

We discussed the findings derived from chamber comparison and their implications and reflections in the new chamber system in chapter 3. The electro-static charge on the Teflon bag was found to be the most critical factor that can significantly affect the total particle number decay rate by up to a factor of 7. A redesigned particle loss correction method was presented with two new components (in addition to the particle wall loss) being brought into consideration for the new UCR fixed-volume chamber: the exceed measurement range particle loss due to coagulation and dilution loss determined by tracer mixing ratio change from beginning to end of an experiment. The new correction method was validated to be capable of recovering 100% of the original particle level by pure seed deposition tests. With the significantly lowered particle wall loss rate and updated particle loss correction, a series of m-xylene oxidation experiments conducted at varying seed levels suggested the existing of vapor wall loss, which can cause underestimation of final SOA mass yield by >50%. However, the study of benzyl alcohol showed an opposite effect of seed on the SOA mass yield, though more experiments are required to consolidate the observation. For future studies, the study of vapor wall loss effects is recommended to be carried out with modeling of particle and gas molecule dynamics. It is also interesting to study whether soft X-ray can affect nucleation or not during oxidation experiments.

In the animal study shown in chapter 4, a preliminary chemical composition analysis was done to provide insights in investigating correlations between mice responses and PM

composition. Consistent results were observed between PM composition and mice responses. Higher fraction of organic components in the PM was found with the strongest lung inflammation being observed. However, things get complicated when study the correlation between "salty" PMs and mice responses. Working as potential reactive oxygen species (ROS), metal ions and organics both contributed high fractions of the mass in the "salty" particles. By comparing the mice responses between salty PM and Alternaria PM, the weaker immune response observed in salty PM exposures indicated that the direct effects from metal ions and other inorganics could be little under such short-term experimental conditions. On the contrary, organic fraction tended to play a more important role in determining the significance of the effects on mice. Although both Salton Sea exposure and Pacific Ocean exposures induced similar lung inflammation which was not significant, Salton Sea exposure achieved the similar results with a smaller fraction of organics. Differences in mice responses in terms of gene regulations further indicated that Salton Sea PM could be potentially more effective in applying certain effects. Long term exposures and more composition analysis are needed for further. Seasonal variation is expected in Salton Sea PM composition with a higher endotoxin concentration during summer and fall than other seasons due to algal bloom. Study in difference of water composition, especially organic species composition, is therefore necessary for the future study.